TUNING BIOMECHANICAL ENERGETICS WITH AN EXOSKELETON TO IMPROVE STABILITY DURING WALKING

A Dissertation
Presented to
The Academic Faculty

by

Pawel Robert Golyski

In Partial Fulfillment
of the Requirements for the Degree
Doctor of Philosophy in the
Bioengineering Interdisciplinary Graduate Program

Georgia Institute of Technology
July 2022

TUNING BIOMECHANICAL ENERGETICS WITH AN EXOSKELETON TO IMPROVE STABILITY DURING WALKING

Approved by:

Dr. Gregory Sawicki, Advisor
The Woodruff School of Mechanical Engineering
Georgia Institute of Technology

Dr. Young-Hui Chang
School of Biological Sciences
Georgia Institute of Technology

Dr. Lena Ting
The Wallace H. Coulter Department of Biomedical Engineering
Georgia Institute of Technology

Dr. Keith Gordon
Department of Physical Therapy and Human Movement Sciences
Northwestern University

Dr. Richard Nichols
School of Biological Sciences
Georgia Institute of Technology

Date Approved: [July 19, 2022]

ACKNOWLEDGEMENTS

TABLE OF CONTENTS

LIST OF TABLES

LIST OF FIGURES

LIST OF SYMBOLS AND ABBREVIATIONS

COM   Center of mass

XCoM   Extrapolated center of mass

TM   Treadmill

AP   Anteroposterior

ML   Mediolateral

MoS   Margin of stability

SL   Step length

SW   Step width

Ips   Ipsilateral

Con   Contralateral

GRF   Ground reaction force

RF   Rectus femoris

MTU   Muscle-tendon unit

WBAM   Whole-body angular momentum

EMG   Electromyography

SUMMARY

Exoskeletons are promising tools to improve multiple aspects of our daily lives – they can increase our strength, improve our efficiency during walking and running, and lower our risk of injury during tasks such as lifting. Further, passive exoskeletons with elastic elements can be lighter and cheaper than their motor-driven counterparts, while also being able to assist us by modulating the mechanics of muscles and biological joints. However, one critical aspect of locomotion which we do not understand the influence of passive exoskeletons on is stability. This dissertation addresses the interaction between the areas of locomotion stability, muscle mechanics, and passive exoskeleton assistance through the lens of mechanical energetics. The overarching goal was to understand whether a passive hip exoskeleton can shift the mechanical energy demands imposed by a perturbation during walking by altering underlying muscle and joint dynamics to improve stability. Chapter 2 describes and validates a novel method for delivering transient, unilateral perturbations in belt speed on an instrumented treadmill. Chapter 3 assesses the effects of different perturbation timings on the mechanical energetics of the leg and joints, with a principal finding being the ankle of the perturbed leg and the knee of the unperturbed leg reflect the energetic demand of a perturbation. Chapter 4 extends this analysis to the level of a hip flexor/knee extensor muscle, the rectus femoris. Using a custom semiautomated application for tracking rectus femoris dynamics, the mechanical energetics at the level of fascicles and the muscle-tendon unit were estimated, with the principal finding that the rectus femoris better reflected the energetic demands of the hip than the knee on the contralateral leg. Finally, Chapter 5 assesses the influence of a passive hip

exoskeleton on stability during perturbed walking both from the perspective of whole-body angular momentum and mechanical energetics. The principal findings from that chapter indicate a disconnect between definitions of stability effects, with the exoskeleton having deleterious effects on the fluctuation of momentum but limited effects on energetics. In all this dissertation contributes valuable first insights into proximal muscle mechanics during human walking and the potential impacts of passive exoskeletons on stability.

CHAPTER 1.   INTRODUCTION

Falls remain a major public health concern in the United States, particularly among adults over 65 and in the workplace. 1 in 4 older adults fell at least once in 2018, accounting for 35.6 million falls and 8.4 million fall-related injuries, with the rate of falls and fall-related injuries remaining unchanged between 2012 and 2018 (Moreland et al., 2020). In 2016, falls resulted in over 25,000 deaths among adults over 75 years old (Hartholt et al., 2019), and non-fatal fall-related injuries incurred a total direct healthcare cost of over $31 billion in 2015 (Burns et al., 2016). Experiencing a fall also results in psychosocial effects such as the development of a fear of falling, which precipitates additional declines in mental and physical health (Bjerk et al., 2018; Lavedán et al., 2018). Further, falls are not limited to older adults alone. 1 in 5 younger adults fall at least once in a 2-year period (Talbot et al., 2005), though these falls are associated with a lower risk of serious injuries such as fractures than in older adults (Sterling et al., 2001). Nevertheless, in 2009, individuals between 35 and 64 years of age accounted for 68% of workplace fall-related injuries, which accounted for $5.4 billion in compensation costs (Yeoh et al., 2013). Across all age groups, most falls occur because of environmental disturbances such as slipping or missing a step, in combination with balance impairments such as tripping or stumbling (Talbot et al., 2005). To address these balance challenges in older adults, exercise training has been shown to be effective, but such training programs are often long in duration (>12 weeks), and adherence to such programs is usually poor (63% compliance across 71 studies; (Sherrington et al., 2019)). In the workplace, indoor fall risk can be improved by raising awareness and improving flooring, but most younger adults fall outdoors (Bell et

al., 2008; Talbot et al., 2005). **Altogether, these findings indicate there is a critical need for interventions that can immediately improve stability during walking in a variety of environments.**

Wearable robots such as exoskeletons may serve as tools to address this need. However, literature investigating the effects of exoskeletons on stability, particularly during perturbed walking, is limited: one study investigated the effects of an active exoskeleton on unperturbed standing balance with added load (Schiffman et al., 2008), a second evaluated how a passive mediolateral leg brace influenced perturbed standing balance (Ringhof et al., 2019), a third investigated the effects of active ankle exoskeleton controllers on perturbed standing balance (Emmens et al., 2018), a fourth explored the effects of an active ankle exoskeleton on gait variability during unperturbed walking (Antonellis et al., 2018), a fifth tested the effects on foot placement of a pre-set hip exoskeleton torque profile during perturbed treadmill walking (Monaco et al., 2017), and two studies provided proof of concept responses of powered hip exoskeletons intended to alter foot placement following pushes during walking (Hua et al., 2021; Zhang et al., 2018). Thus, current state-of-the-art exoskeleton designs focus on treatment of the human-exoskeleton system as a bipedal robot, with limited consideration of the stabilizing properties of biological structures. Terrestrial vertebrates have the remarkable ability to rapidly adapt the mechanics of their limbs (Daley et al., 2006; Ferris and Farley, 1997; Ferris et al., 1999), joints (Daley et al., 2007; Dick et al., 2019), and muscles (Daley and Biewener, 2011; Daley et al., 2009; Dick et al., 2021) through mechanisms involving intrinsic muscle-tendon mechanics, spinal reflexes, and higher brain centers (Daley and Biewener, 2011; Daley et al., 2009; Dick et al., 2021; Dietz et al., 1989; Hof and Duysens,

2018; Shinya et al., 2009; Sloot et al., 2015; van der Linden et al., 2007). Thus, an alternative approach to developing stabilizing exoskeletons is to tap into the stabilizing properties of biological joints and muscles using simple wearable devices. To execute such an approach, **the connections between locomotion stability, muscle mechanics, and exoskeleton assistance must be understood. Exploring the connections between these three pillars is the central focus of this dissertation**. To be able to make these connections, a measure that can both quantify the destabilizing demands of a perturbation during locomotion, while also being able to relate to muscle and exoskeleton mechanics, is necessary. Mechanical energy was selected as this measure, since 1) the mechanical works at each level of musculoskeletal description lend themselves to energy accounting analysis (e.g., the summed leg joint works should equal the overall work of a leg, the summed muscle-tendon unit works of a leg should equal the summed leg joint works, etc.), and 2) because the net mechanical work on the legs and body is zero on average over a steady state, level ground stride at constant speed, any deviations from this energetic reference caused by an environmental perturbation can be classified as a destabilizing energetic demand. Thus, within this perturbation energetics paradigm, the demand of a destabilizing perturbation can be framed as eliciting either negative or positive work, which can subsequently be tracked across all levels of description at which mechanical work is measured. Within this framework, a device which can shift the energetic role of joints and muscles to oppose the energetic demand of the perturbation should be stabilizing. In the lower limbs of terrestrial vertebrates, proximal muscle-tendon units – with stiff tendons, low pennation angles, and long fascicles capable of rapid length changes – may be better morphologically suited for generating mechanical work (Biewener, 2016; Gillis and

Biewener, 2002; McGowan et al., 2007). Further, in humans the hip joint has been identified as being a principal contributor to the net mechanical work produced by the leg during tasks that require energy generation, such as accelerating and inclined locomotion (Roberts and Belliveau, 2005; Schache et al., 2019). Literature at the intersection of exoskeletons and mechanical energetics has largely focused on providing external mechanical work using active devices to reduce the metabolic cost of locomotion ((Sawicki et al., 2020) as a review). However, studies have also demonstrated that passive devices, even though they cannot contribute net mechanical work themselves, can lead to shifts towards positive net mechanical work at both the hip (Lewis and Ferris, 2011) and ankle (Collins et al., 2015), potentially by altering the dynamics of underlying musculature (Nuckols et al., 2020a) or transferring energy to other joints (van Dijk and van der Kooij, 2014). Since passive devices can be cheaper and lighter than their powered counterparts, the potential of stabilizing passive exoskeletons warrants investigation.

Considering the energetic roles of proximal joints and muscles and the potential mechanical energetic shifts induced of a passive exoskeleton, there were **two specific aims of this dissertation: 1) to determine the multi-scale response to transient mechanical energy demands of proximal joints and muscles, and 2) to evaluate the influence of an elastic hip exoskeleton on stability during perturbed walking**. These aims were addressed in 4 chapters of original research.

To impose destabilizing transient mechanical energy demands during walking, all studies in this dissertation used rapid unilateral belt accelerations targeted at specific points in the walking gait cycle. Chapter 2, an accepted publication in the Journal of Biomechanics (Golyski et al., 2021), serves as validation of the custom algorithm used to

deliver the perturbations, in addition to a preliminary assessment of the effects of different perturbation timings on spatiotemporal stability measures.

Chapter 3, an accepted publication in the Journal of the Royal Society Interface (Golyski and Sawicki, 2022), describes the effects of different treadmill perturbation timings on the mechanical energetics of the perturbed leg. This study also relates the energetic effects of the perturbation between the leg and joint levels to determine which joints best reflect leg-level demands.

Chapter 4, which I indent to submit to the Journal of Experimental Biology, extends the energy accounting analysis of the previous chapter to the level of a proximal leg muscle - specifically the rectus femoris. This muscle was initially selected since 1) it acts as a hip flexor, hence would likely be engaged as the perturbation extends the leg, 2) it is active in late stance during unperturbed walking, so would likely contribute to the mechanical energetics of the leg during any perturbation timing, and 3) as a biarticular muscle, it allows for investigation of how mechanical work is transferred between joints during perturbed walking. This chapter also describes a custom semiautomated tracking application for measurement of proximal muscle fascicle dynamics. *In-vivo* dynamics together with electromyography and Hill-type models of muscle force were used to estimate mechanical energetics at the level of rectus femoris fascicles and muscle-tendon units (Dick et al., 2017; Zajac, 1989). From these data, the energetic role of the rectus femoris during perturbed walking was related to the roles of the hip, knee, and leg.

Chapter 5, which I intend to submit to the Journal of Biomechanics, addresses the second specific aim and incorporates a passive hip exoskeleton into the perturbation

energetics paradigm. As part of that study, 1) a custom passive hip flexion assisting exoskeleton was developed which provided a bio-inspired assistive hip flexion torque (Haufe et al., 2020; Panizzolo et al., 2019; Shamaei et al., 2013) while also allowing for B-mode ultrasound imaging of the rectus femoris, and 2) the custom semiautomated fascicle tracking application was supplemented with a deep learning approach to allow for fully automated measurement of rectus femoris fascicle dynamics. The effects of the passive hip exoskeleton on stability, as quantified by changes in whole-body angular momentum (Herr and Popovic, 2008), in addition to mechanical energetics at the whole-body down to the level of the rectus femoris fascicles, were assessed. The results of that investigation serve to relate stability as defined according to whole-body angular momentum and mechanical energetics, while also assessing whether passive exoskeletons can have effects at the whole-body level by altering the mechanical energetics at the muscle level.

Altogether, these studies provide several important contributions to the literature including: 1) establishing a link between stability and energetics during human walking, 2) the first *in-vivo* measurements of hip muscle dynamics during locomotion in humans, 3) the first direct measurements of the effects of a hip exoskeleton on underlying muscle mechanics, and 4) the first assessment of the effects of a passive exoskeleton during perturbed walking. I anticipate this dissertation will spur additional multi-scale mechanical energetics-based investigations of locomotor stability and will inform the next generation of stabilizing wearable robots.

CHAPTER 2.   VALIDATION OF A GAIT-PHASE TARGETED TREADMILL PERTURBATION

The first work associated with my dissertation is an article describing and validating the method used to deliver transient unilateral perturbations in treadmill belt speed at specified times during the gait cycle. It has been published in the Journal of Biomechanics and is entitled, "Onset timing of treadmill belt perturbations influences stability during walking." (Golyski et al., 2021). That published article is reproduced in this chapter.

2.1   Abstract

Split-belt treadmills have become popular tools for investigating stability during walking by using belt accelerations to induce slip-like perturbations. While the onset timing of destabilizing perturbations is a critical determinant of an individual's stabilizing response, previous studies have predominantly delivered belt acceleration perturbations at heel strike or have not explicitly controlled onset as a percentage of the gait cycle. To address this gap, we 1) developed an algorithm to target transient increases in unilateral belt speed to begin at specific percentages of the walking gait cycle, 2) validated the algorithm's accuracy and precision, and 3) investigated the influence of different onset timings on spatial stability measures. We evaluated desired onset timings of 10, 15, 20, and 30% of the gait cycle during walking at 1.25 m/s and measured step lengths and widths, as well as anteroposterior and mediolateral margins of stability during the perturbed and four recovery steps in 10 able-bodied participants. From 800 perturbations, we found a mean (standard deviation) delay in onset timing of 5.2% (0.9%) of the gait cycle, or 56 (9)

ms. We hypothesized later onset timings would elicit more stabilizing responses due to the less stable configuration of the body during late vs. early single stance. Our data generally supported this hypothesis – in comparison to earlier onset timings, later onset timings precipitated greater stabilizing responses, including larger step lengths, step widths, and anteroposterior/mediolateral margins of stability on the perturbed step, in addition to shorter step lengths and wider step widths on the first step post-perturbation.

2.2   Introduction

Rapid belt accelerations on split-belt treadmills can emulate slip-like perturbations to study dynamic stability recovery mechanisms with precise control. Although rapid belt accelerations are not identical to slips, the destabilizing effects of both forward pitching slips and belt accelerations are similar, causing a more anterior center of mass position relative to the base of support during the perturbed step (Debelle et al., 2020). Previous work has explored the influence of the direction (i.e., acceleration vs. deceleration) and magnitude of single belt accelerations during walking on stability (Ilmane et al., 2015; Kagawa et al., 2011; Lee et al., 2019; van den Bogaart et al., 2020), but the relationship between gait phase progression at belt acceleration onset and stability measures has not been systematically explored. The majority of studies using rapid belt acceleration perturbations during walking have targeted heel strike as the perturbation onset (Figura et al., 1986; Kagawa et al., 2011; Liu et al., 2018; Roeles et al., 2018; van den Bogaart et al., 2020; Yang et al., 2013), or have not explicitly controlled the onset to begin at a certain percentage of the gait cycle (Berger et al., 1984; Gholizadeh et al., 2019; Lurie et al., 2013; Madehkhaksar et al., 2018). From experiments using other types of perturbations, such as lateral pushes, trips, and force plate translations, the onset timing of a perturbation has been

shown to influence the stabilizing response (Eng et al., 1994; Hof et al., 2010; Tang and Woollacott, 1999). Our goals in this work were: 1) to describe and validate the performance of an algorithm that controls the onset of unilateral belt accelerations to begin at specified percentages of the walking gait cycle, and 2) to preliminarily investigate the influence of different onset timings on stability measures. To guide our secondary goal, we hypothesized onset timings later in single stance would be most destabilizing, and hence would elicit more stabilizing responses, since the center of mass is most anterior to the base of support in late single stance (Debelle et al., 2020).

2.3   Methods

2.3.1   Study Design and Procedures

Ten healthy participants (Table 1) walked at 1.25 m/s on an instrumented split-belt treadmill (CAREN; Motek, Netherlands; Figure 1A). Following a 5-minute treadmill acclimation, participants continued to walk for approximately 30 minutes with unexpected belt accelerations (Zeni and Higginson, 2010). Individual belts were commanded to accelerate from 1.25 m/s to reach and hold at 2.5 m/s, then decelerate to 1.25 m/s (Figure 2A). The commanded accelerations/decelerations were 15 m/s^2 and the duration of the entire perturbation was ~30% (~340 ms) of the gait cycle. A 10-camera motion capture system (Vicon, Oxford, UK) collected positions of reflective markers placed on bilateral heels, PSIS, and second metatarsals (MT2) at 100 Hz (Figure 1A). Onsets of belt accelerations were targeted at 10, 15, 20, and 30% of the gait cycle (Figure 1B). Each participant was perturbed 10 times on each leg at each onset timing (*i.e.*, 80 perturbations per participant). 40 and 50% onset timings were investigated but not analyzed since the

perturbed feet did not reach maximum velocity (2.5 m/s) before toe-off. The timing and leg of each perturbation were randomized, and participants took an average of 15 steps (standard deviation: 4 steps) between perturbations. All participants provided informed consent to the protocol approved by the local Institutional Review Board.

Table 1 - Participant demographics. SD = standard deviation

Participant	Gender	Age (years)	Stature (cm)	Weight (kg)	Right Leg Length (cm)
1	M	29	189.0	73.2	100.0
2	M	18	176.5	73.5	89.4
3	M	23	173.7	89.0	88.9
4	M	27	183.5	87.5	95.2
5	M	23	188.0	73.0	100.3
6	F	22	156.5	47.8	83.6
7	M	21	181.5	76.6	93.3
8	M	22	170.0	74.5	92.0
9	M	25	183.8	82.4	96.5
10	F	28	161.0	63.1	86.3
Mean (SD)		24 (3)	176.4 (11.1)	74.1 (12.0)	92.6 (5.6)

2.3.2 Timing Algorithm

Perturbation timing was implemented using D-Flow (Motek, Netherlands). Heel strikes and corresponding gait cycles were identified in real-time based on pelvis and heel marker positions (Zeni et al., 2008). After a perturbed leg and onset timing were selected, the algorithm would wait until the next heel strike on the selected leg. The algorithm then calculated the delay to deliver the perturbation at the specified gait cycle percentage. This delay was the product of the desired onset timing (*e.g.*, 10% of the gait cycle) and the duration of the previous gait cycle of the selected leg.

To validate the algorithm, perturbation onset time ($t_{Pert\ Onset}$) was measured as the elapsed time from heel strike to when velocity of the MT2 marker of the perturbed foot crossed above 110% of the unperturbed walking speed (*i.e.*, above 1.375 m/s). This threshold was similar to the minimal detectable change in self-selected walking speed for young adults (0.18 m/s; (Washabaugh et al., 2017), so the measured onset timing could be interpreted as when the perturbation first became statistically meaningful. Absolute onset delays were calculated using Eq 1:

$$Onset\ Delay_{Absolute} = t_{Pert\ Onset} - \frac{Desired\ Onset\ Timing}{100} \cdot t_{Prev\ Ips\ GC} \qquad \text{Eq 1}$$

Where $t_{Prev\ Ips\ GC}$ is duration of the ipsilateral gait cycle preceding the perturbation, and *Desired Onset Timing* is a percentage of the gait cycle. Absolute delays were converted to percentages of the gait cycle using Eq 2:

$$Onset\ Delay_{Percent\ Gait\ Cycle} = \frac{Onset\ Delay_{Absolute}}{t_{Prev\ Ips\ GC}} * 100 \qquad \text{Eq 2}$$

Accuracy of the algorithm was validated using mean onset delays, while precision was validated using standard deviation of onset delays.

2.3.3 Data Processing

Data were analyzed in MATLAB (Mathworks, Natick, MA). Marker trajectories were low pass filtered at 6 Hz. Stability metrics are graphically presented in Figure 1C. All metrics were calculated at heel strike. The perturbed step (S0 in Figure 2) was defined by the first heel strike following, and on the side contralateral to, that of the perturbation. The differences in anteroposterior and mediolateral positions of the heel markers were used to

calculate step length and step width, respectively. Margins of stability (Hof et al., 2005) were approximated using marker positions similar to McAndrew Young et al., 2012. Anteroposterior margin of stability (AP MoS) was approximated as the difference between the leading leg's anteroposterior MT2 position and the extrapolated center of mass (XCoM), corrected by the velocity of the leading MT2 marker scaled by leg length and gravity (Beltran et al., 2014; Süptitz et al., 2012; Figure 1C Eq 3). Mediolateral margin of stability (ML MoS) was approximated as the mediolateral distance between the heel marker of the leading leg and XCoM (Figure 1C Eq 4). Use of heel vs. lateral foot markers introduces an offset that underestimates ML MoS relative to literature, but should not affect relative differences in ML MoS across onset timings (Roden-Reynolds et al., 2015). XCoM was approximated using the mean PSIS position as the center of mass and the equations of Hof et al., 2005 (Figure 1C Eq 5). A larger AP/ML MoS indicates increased stability in the anterior/lateral directions, respectively.

2.3.4   Statistics

Step length was the only outcome significantly affected by leg side following perturbations ($p = 0.046$, $p > 0.205$ for all other outcomes), but this difference was less than the minimal detectable change of this variable (0.47 cm vs. 1.88 cm; Rabago et al., 2015). Thus, left and right perturbations were combined. Shapiro-Wilks tests for normality were not significant for outcome measures ($p > 0.065$) except for step length ($p < 0.041$). Thus, Friedman's test with Dunn-Bonferroni post-hoc tests were used to assess the influence of perturbation timing on step length. For AP MoS, ML MoS, and step width, two-factor linear mixed models with a random effect of participant and a fixed effect of perturbation timing were run with Bonferroni-corrected pairwise post-hoc tests. Statistical tests were

run separately for each step relative to the perturbation since models including both step number and onset timing showed significant interactions between step number and onset timing (p < 0.001). All statistical analyses were performed in SPSS (IBM, Chicago, IL), with significance concluded when p < 0.050.

$$AP\ MoS = AP\ P_{MT2,Leading} - AP\ XCoM - \frac{|AP\ V_{MT2,Leading}|}{\sqrt{\frac{g}{L}}} \quad \text{(Eq 3)}$$

$$ML\ MoS = ML\ P_{HEEL,Leading} - ML\ XCoM \quad \text{(Eq 4)}$$

$$XCoM = Mean\ P_{PSIS} + \frac{Mean\ V_{PSIS}}{\sqrt{\frac{g}{L}}} \quad \text{(Eq 5)}$$
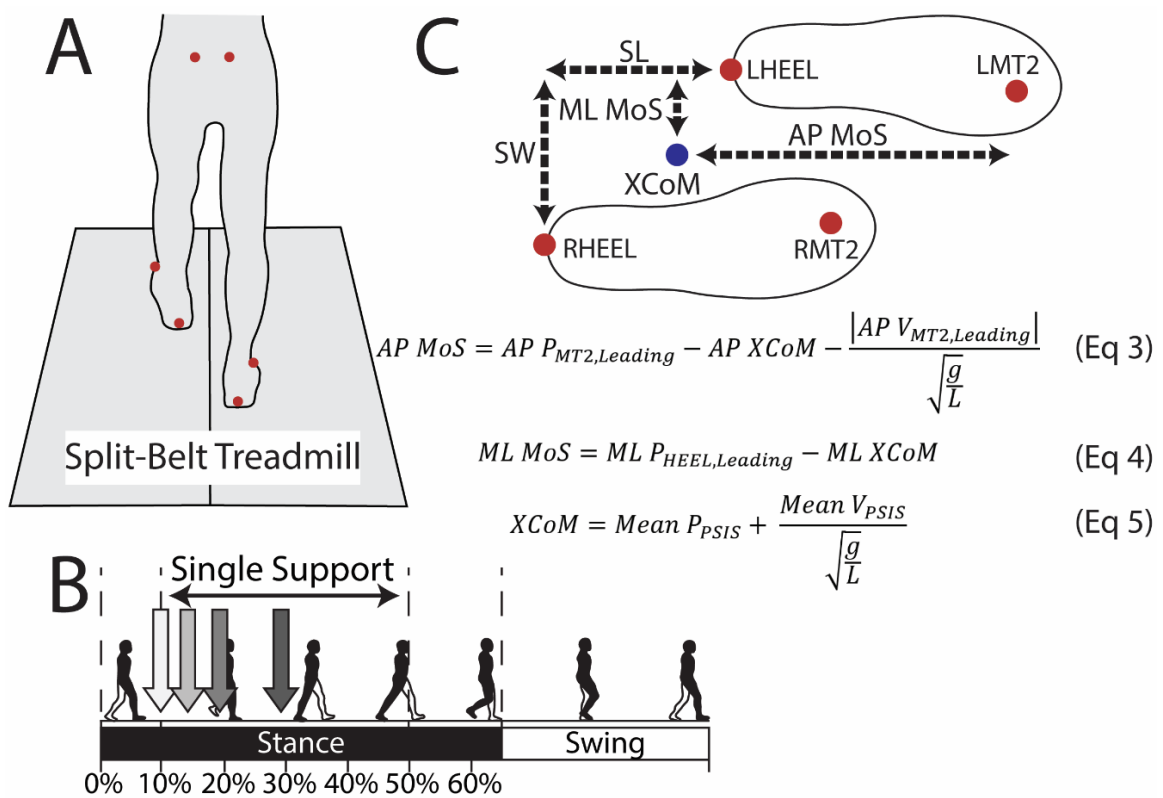
Figure 1 – (A) Collection setup with reflective marker placements. (B) Targeted onset timings of belt acceleration perturbations as a percentage of the gait cycle. Onset timings were targeted to single support, with 30% of the gait cycle hypothesized to be most destabilizing since the center of mass is most anterior to the base of support in late single stance. (C) Spatial outcome measures measured at a hypothetical left heel strike with equations used to calculate AP and ML MoS. SL = Step Length, SW = Step Width, L/RMT2 = L/R second metatarsal heads, XCoM = extrapolated center of mass, AP/ML MoS = Anteroposterior/Mediolateral margin of stability, g = gravitational constant, L = leg length, P = positions, V = velocities.

2.4 Results

2.4.1 Perturbation Timing Validation

The average accuracy across onset timings, as quantified by mean onset delay, was 5.2% of the gait cycle (56 ms), while the average precision, as quantified by the standard deviation of onset delay, was 0.9% of the gait cycle (9 ms; Table 2). The commanded and measured velocities are shown in Figure 2A and Figure 2B, respectively.

Table 2 – Accuracy and precision validation measures in percentage of gait cycle and milliseconds. Perturbation onset time was measured as the elapsed time from heel strike to when velocity of the MT2 marker of the perturbed foot crossed above 110% of 1.25 m/s (*i.e.*, above 1.375 m/s). Absolute onset delays in milliseconds were calculated by subtracting the desired onset percentage multiplied by the duration of the ipsilateral gait cycle preceding the perturbation from the measured onset time (Eq 1). Absolute onset delays were converted to percentages of the gait cycle by dividing by the duration of the ipsilateral gait cycle preceding the perturbation (Eq 2).

	Desired Onset Timing (% Gait Cycle)	10%	15%	20%	30%
Accuracy Metrics	Mean Onset Delay (% Gait Cycle)	5.1	5.1	5.2	5.4
	Mean Onset Delay (ms)	54	55	56	58
Precision Metrics	Standard Deviation of Onset Delay (% Gait Cycle)	0.9	0.9	0.9	1.0
	Standard Deviation of Onset Delay (ms)	9	9	9	10

2.4.2 Stability Outcome Measures

On the perturbed step ($p < 0.001$) and the first step post-perturbation ($p = 0.016$), there was an effect of onset timing on AP MoS (Figure 2C). On the perturbed step, later onset timings resulted in larger AP MoS – pairwise comparisons showed 30% onset timings

had larger AP MoS than all other timings (p < 0.001), while 20% onset timings had larger AP MoS than 10% onset timings (p = 0.018). Conversely, for the first step post-perturbation, earlier onset timings resulted in larger AP MoS – 10% onset timings resulted in larger AP MoS than 30% onset timings (p = 0.017).

On all steps following the perturbation, there was an effect of onset timing on step length (p=0.002 for perturbed step, p < 0.001 for all steps post-perturbation; Figure 2D). On the perturbed step, later onset timings resulted in larger step lengths – 20 and 30% onset timings had larger step lengths than 10% onset timings (p < 0.019). For the first step post-perturbation, later onset timings resulted in smaller step lengths –20 and 30% onset timings had smaller step lengths than 10% onset timings (p < 0.019) and 30% onset timings had smaller step lengths than 15% onset timings (p = 0.003). For the second through fourth steps post-perturbation, earlier onset timings resulted in smaller step lengths – 10% onset timings had smaller step lengths than 20 and 30% timings (p < 0.034), and for the second and third steps post-perturbation 15% timings had larger step lengths than 30% timings (p=0.034).

On the perturbed step alone, there was a significant effect of onset timing on ML MoS (p=0.003; Figure 2E), with later onset timings tending to have larger ML MoS than earlier timings. 20% onset timings had significantly larger ML MoS than the 10 and 15% onset timings (p < 0.017).

On the perturbed step and first step post-perturbation, there was an effect of onset timing on step width (p < 0.047; Figure 2F). For the perturbed step, 20% onset timings resulted in the largest step widths – 20% onset timings had significantly larger step widths

15

than 10% onset timings (p=0.047). For the first step post-perturbation, despite a significant

effect of onset timing and a trend of 20% onset timings resulting in the largest step widths,

no pairwise comparisons were significant (p > 0.061).
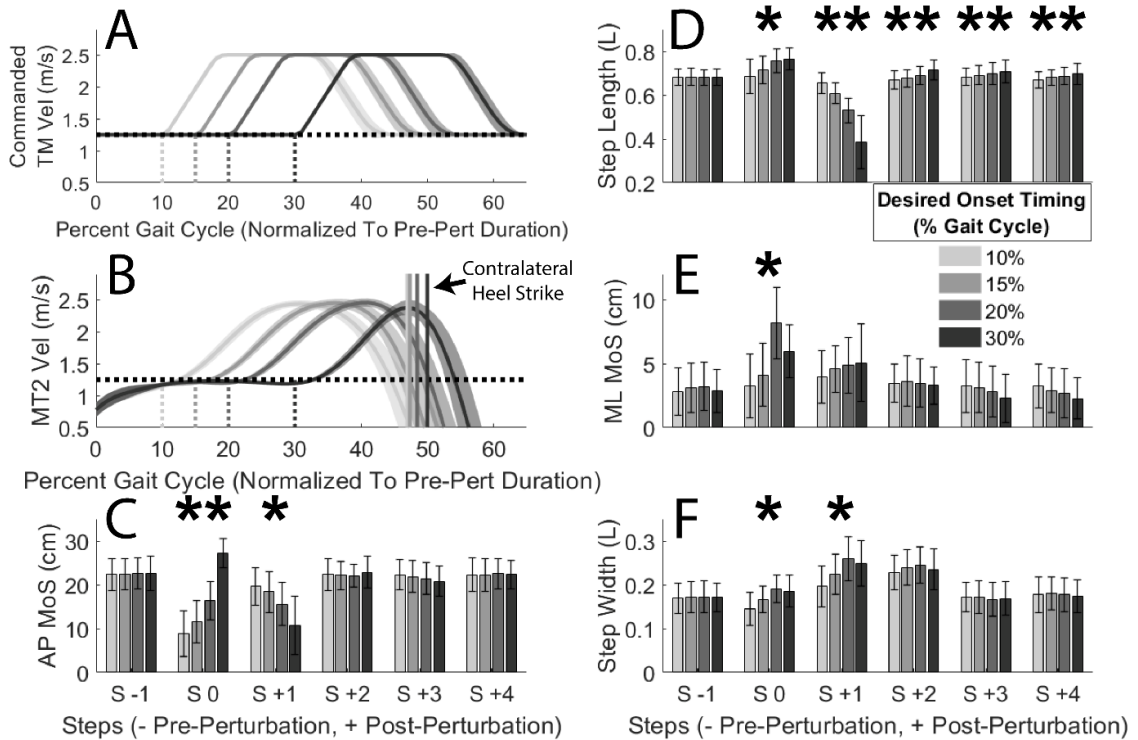
Figure 2 – (A) Commanded treadmill velocity profiles and (B) measured MT2 marker velocities of the perturbed foot for all analyzed perturbations. Gait cycles were normalized to the duration of the ipsilateral gait cycle preceding the perturbation. Solid vertical lines indicate the end of single support. Shaded areas represent ±1 standard deviation. Dotted vertical lines represent desired start times. Horizontal dotted lines represent the unperturbed velocity (1.25 m/s). (C-F) Across-subject mean spatial stability measures. Error bars represent ±1 standard deviation. L = metric normalized to participant leg length. AP MoS = anteroposterior margin of stability. ML MoS = mediolateral margin of stability. * = p < 0.050 and ** = p < 0.001 for effect of timing for that step. Pairwise comparisons are described in text.

16

2.5   Discussion

2.5.1   Algorithm Evaluation

To evaluate the algorithm's accuracy, we defined a successful single stance perturbation as a one that induced maximum belt speed of the stance foot before double support. Thus, based on our commanded belt acceleration, an unperturbed gait cycle duration, and the latest onset timing, the *a priori* maximum acceptable onset delay was 13% of the gait cycle. The measured accuracy fulfilled this requirement, with perturbations being delivered 5.2% of the gait cycle after the desired onset time. Perturbations also had to be delivered such that they did not "spill over" into other onset timings. Thus, our *a priori* threshold for acceptable precision was half the minimum difference in targeted onset timings (*i.e.*, 2.5% of the gait cycle), which would ensure ~95% of the perturbations were delivered within ±5% of the gait cycle centered at each desired onset timing. Our measured accuracy (0.9% of the gait cycle) also fulfilled this criterion.

2.5.2   Effect of Onset Timing on Stability

As the walking gait cycle progresses, the extrapolated center of mass first crosses in front of the anterior boundary of the base of support as early as 6% of the gait cycle and continues to move anteriorly until contralateral heel strike (Debelle et al., 2020). Thus, from the onset of single support to the beginning of double support, the negative AP MoS, and hence the risk of a forward fall, increases, while the time to make a corrective foot placement decreases (Hof et al., 2010; Vlutters et al., 2018). This spurred our hypothesis that belt accelerations with onset timings later in single stance would elicit more stabilizing responses, which was generally supported by our data.

Following a posterior perturbation of the base of support (mechanically analogous to an anterior center of mass push), *larger* step lengths on the perturbed step are stabilizing since the leading limb can apply a larger posterior braking force (Joshi and Srinivasan, 2019; Wang and Srinivasan, 2014), and more mechanical work is dissipated by collision (Donelan et al., 2002a; Kuo, 2002). By decreasing center of mass velocity, this increased braking/dissipation precipitates a *smaller* post-perturbation step length (Kuo and Donelan, 2010), which is more stabilizing during recovery (Espy et al., 2010). Such stabilizing step length changes have been observed following both belt accelerations (Afschrift et al., 2019; Debelle et al., 2020; Roeles et al., 2018; Sloot et al., 2015) and anterior pelvic pulls (Vlutters et al., 2018). Consistent with these mechanisms and literature, we found later onset timings elicited more stabilizing step lengths on both the perturbed step and first step post-perturbation in comparison to earlier onset timings, with trends in AP MoS following these changes in step length.

In the frontal plane, later onset timings generally resulted in more stabilizing (Donelan et al., 2004), larger step widths and ML MoS for the perturbed and post-perturbation steps, except for onset timings of 30%. Coupling between AP and ML foot placement may explain larger step widths on the perturbed step (Bauby and Kuo, 2000; Kim and Collins, 2017), which together with a larger ML MoS elicits more lateral subsequent foot placement and larger step widths on the first step post-perturbation (Rankin et al., 2014). Less stabilizing step widths and ML MoS for 30 vs. 20% onset timings may stem from 1) perturbations with 30% onset timings being less destabilizing since double support begins midway through the perturbation (Figure 2B) or 2) insufficient

time for foot positioning exacerbated by the anterior perturbation shortening single-stance duration (Roeles et al., 2018; Sloot et al., 2015; Vlutters et al., 2018).

2.5.3 Limitations

Our participants were young able-bodied individuals, so it is unknown how these results would generalize to participants with balance impairments. Further, the belt accelerations we applied in early stance do not represent usual balance challenges faced in daily life – early slips are associated with backwards pitching and would be better represented by a belt deceleration beginning at heel strike (Heiden et al., 2006; Nagano et al., 2013). Despite these limitations, belt accelerations provide an accessible tool to investigate the stabilizing responses individuals use while walking.

2.6 Acknowledgements

CHAPTER 3.   RELATING JOINT AND LEG LEVEL MECHANICAL ENERGETICS DURING PERTURBED WALKING

The second work associated with my dissertation evaluates whether transient unilateral treadmill perturbations can elicit energetic demands and investigating which joints reflect overall leg level demands. This work is currently in press at the Journal of the Royal Society Interface (Golyski and Sawicki, 2022). That published article is reproduced in this chapter.

3.1   Abstract

Current approaches to investigating stabilizing responses during locomotion lack measures that both directly relate to perturbation demands and are shared across different levels of description (*i.e.*, joints, legs). Here we investigated whether mechanical energy could serve as a "common currency" during treadmill walking with transient unilateral belt accelerations. We hypothesized that by delivering perturbations in either early or late stance, we could elicit net negative or positive work, respectively, from the perturbed leg at the leg/treadmill interface, which would dictate the net demand at the overall leg level. We further hypothesized that of the lower-limb joints, the ankle would best reflect changes in overall leg work. On average across all 7 participants and 222 perturbations, we found early stance perturbations elicited no change in net work performed by the perturbed leg on the treadmill, but net positive work by the overall leg, which did not support our hypotheses. Conversely, late stance perturbations partially supported our hypotheses by

eliciting positive work at the leg/treadmill interface, but no change in net work by the overall leg. In support of our final hypothesis, changes in perturbed ankle work, in addition to contralateral knee work, best reflected changes in overall leg work.

3.2   Introduction

Falls remain a major public health problem. In the United States alone, 1 in 4 adults over 65 years old fall at least once a year, which results in over 25,000 deaths annually and $31 billion in annual direct healthcare costs (Burns et al., 2016; Hartholt et al., 2019; Moreland et al., 2020). In the workplace, falls caused 16% of fatal work-related injuries in 2019, with 68% of fall-related injuries occurring in individuals between 35 and 64 years old (US Bureau of Labor Statistics, 2021; Yeoh et al., 2013). In both younger and older adults, falls occur more often during walking than any other locomotor task, with external disturbances such as slips and trips being the predominant perceived cause of falls (Berg et al., 1997; Talbot et al., 2005). Although responses to external perturbations have been extensively studied at the overall leg (*e.g.*, foot placement), joints, and muscles (*e.g.*, Debelle et al., 2020; Eng et al., 1994; Grabiner et al., 1993; King et al., 2019; Li and Huang, 2021; Pijnappels et al., 2004; Roeles et al., 2018; Schillings et al., 2000; Sloot et al., 2015; Tang et al., 1998), relating these different levels of description remains difficult. Two obstacles to such analyses are: 1) variables used to characterise responses are generally not measured using a "common currency" that can be easily related across different levels, and 2) the explicit, quantifiable demand imposed by the perturbation is unknown. In this work we aimed to overcome these obstacles by using a split-belt treadmill to deliver destabilizing perturbations using transient changes in belt speed that imposed quantifiable energetic demands on the legs that could be related to changes in work at the joints. We anticipate

this analysis will serve as an initial step in describing stabilizing responses at multiple levels using mechanical energetics.

The mechanical power of each leg during walking, with respect to a fixed global reference frame and assuming massless legs, can be estimated using the individual limbs method (Donelan et al., 2002b), which quantifies the mechanical energy flowing between the ground and the centre of mass (COM). During overground walking, the mechanical power of each leg is the dot product of its corresponding ground reaction force (GRF) and COM velocity. No power flows between each leg and the ground because the velocity of the ground is 0, thus $\boldsymbol{F}_{Leg} \cdot \boldsymbol{v}_{ground} = 0$, where $\boldsymbol{F}_{Leg}$ is equal and opposite to the ground reaction force. However, for treadmill walking, this is no longer the case; with respect to a fixed global reference frame, each belt is moving, so the power flowing from each leg to its corresponding belt is $\boldsymbol{F}_{Leg} \cdot \boldsymbol{v}_{belt}$. Thus, in the case of treadmill walking, the mechanical power of each leg is the sum of the power flowing from the leg to the treadmill belt and the leg to the COM (Selgrade et al., 2017).

During level ground treadmill walking with both belts of a split-belt treadmill moving at the same constant speed, the net work of each leg on the COM is zero on average over a stride. Further, with both belts moving at the same speed, since the average anteroposterior force must be zero over a stride (otherwise the COM would accelerate relative to the treadmill), each leg performs zero net mechanical work on its corresponding belt. Therefore, in this condition the net work performed by each leg must be zero on average (Sánchez et al., 2019). However, in either non-steady conditions or when belts of a split-belt treadmill are moving at different speeds, the previous assumptions no longer

hold, and a treadmill can elicit an energetic demand on the leg over a stride. In this study, we leveraged this concept and designed perturbations intended to elicit a change in net work over a stride by a leg (*i.e.,* generation or dissipation). Specifically, since leg force is directed anteriorly in early stance and posteriorly in late stance, by increasing the posterior velocity of a belt, our first hypothesis (H1) was net negative work would be performed by the perturbed leg on the treadmill over a stride with an early stance perturbation, while net positive work would be performed with a late stance perturbation (Figure 3). Our second hypothesis (H2) was that such changes in net work at the leg/treadmill interface relative to an unperturbed stride would be reflected at the level of overall leg work, since the treadmill environment limits large fluctuations in COM velocity and thus also the mechanical power exchanged between each leg and the COM ($\boldsymbol{F}_{GRF} \cdot \boldsymbol{v}_{COM}$).

While no previous work has investigated the mechanical energetics of transient unilateral treadmill speed perturbations during walking, there are numerous experimental contexts that elicit an energetic demand on the legs during locomotion by changing the required amount of work the legs perform on the COM. Examples include increasing or decreasing the slope of the ground relative to level (Alexander et al., 2017; Lay et al., 2007; Montgomery and Grabowski, 2018; Nuckols et al., 2020b; Roberts and Belliveau, 2005), accelerating or decelerating (Qiao and Jindrich, 2016; Schache et al., 2019), and falling into a hole (Daley et al., 2007; Dick et al., 2019). In general, relative to level ground, walking on an incline results in a shift to more positive work and power at the hip joint (Alexander et al., 2017; Lay et al., 2007; Montgomery and Grabowski, 2018; Nuckols et al., 2020b), while walking on a decline results in more negative work and power at the knee joint (Alexander et al., 2017; Lay et al., 2007; Nuckols et al., 2020b). However, in the case

of speed changes and ground height perturbations, changes in ankle work and power best reflect the overall demand on the leg (Daley et al., 2007; Dick et al., 2019; Farris and Raiteri, 2017; Qiao and Jindrich, 2016; Schache et al., 2019). Since our perturbations were more similar to speed changes than slope changes, our third hypothesis (H3) was that changes in net leg work over a stride resulting from the perturbation would primarily be reflected by changes in net work at the ankle joint.

3.3 Methods

3.3.1 Experimental Protocol

Seven young, healthy individuals (5 males, 2 females, mean [SD]: 25 [2] years, 178.5 [12.1] cm stature, 72.7 [13.3] kg) walked on an instrumented split-belt treadmill (CAREN; Motek, Netherlands). Following an unperturbed 5-minute acclimation period at 1.25 m/s (Zeni and Higginson, 2010), transient unilateral belt accelerations were delivered during walking. Each perturbation was targeted to either early or late stance and either the left or right leg. Each timing/leg pairing was repeated 10 times (*i.e.*, 2 legs x 2 timings x 10 repetitions = 40 perturbations per participant). The order of perturbations was randomized, with 30-40 steps between perturbations to ensure the perturbation was unexpected and the participant had returned to steady state walking (Liu et al., 2018). The perturbation algorithm is fully described elsewhere (Golyski et al., 2021), and used real-time kinematic data to estimate gait phase during walking. Perturbations consisted of a brief (mean duration: 340 ms, 32.9% perturbed gait cycle) increase in belt speed from 1.25 m/s to 2.5 m/s (Figure 3B). All participants provided informed consent as approved by the local Institutional Review Board.
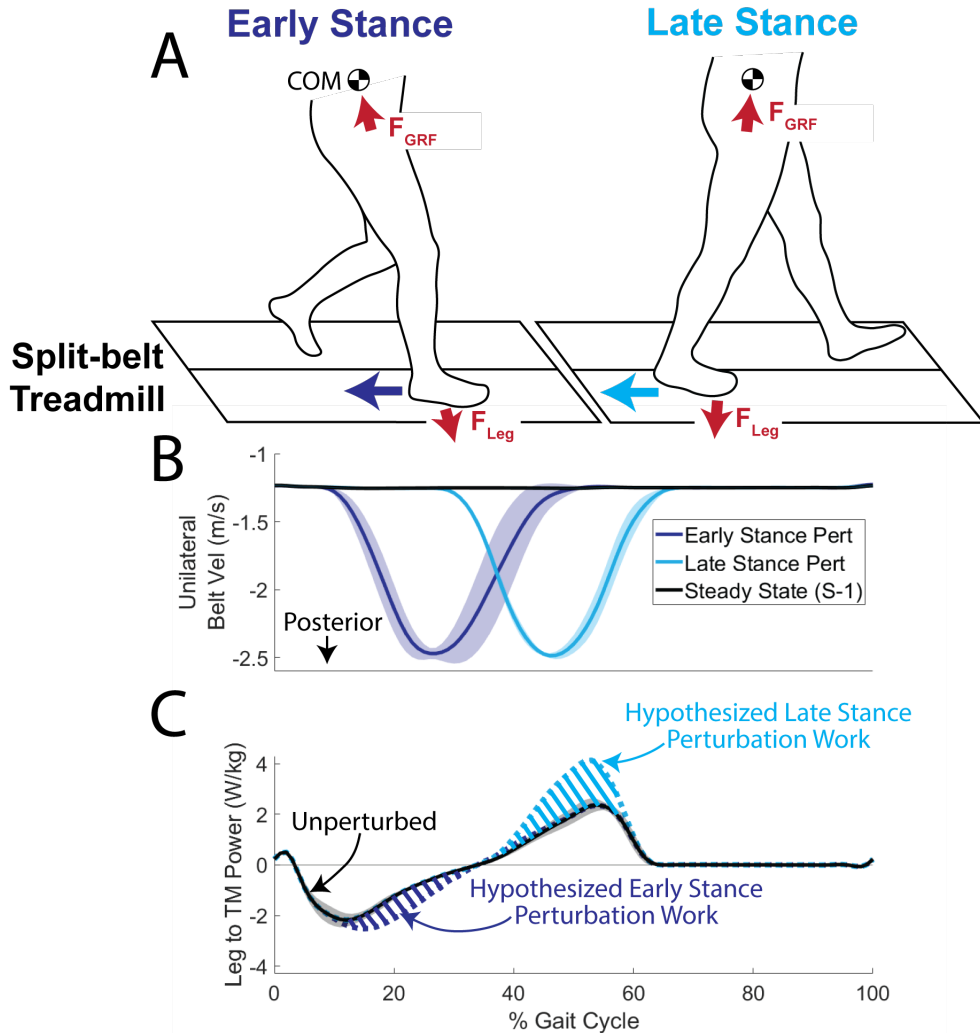
Figure 3 – Perturbation overview. A) Perturbation design. In early stance perturbations, since the leg force is anterior and treadmill velocity is posterior, this results in the leg performing negative work on the belt. In late stance, when leg force is posterior and treadmill velocity is posterior, the leg performs positive work on the belt. B) Unilateral belt velocity traces show across-subject ensemble averages. Shaded regions represent ±1 standard deviation. C) Hypothesized changes in power flowing from the leg to the treadmill relative to steady state, with early stance perturbations eliciting negative power (*e.g.*, dissipation) and late stance perturbations eliciting positive power (*e.g.*, generation).

3.3.2   Data Acquisition

3D forces from the instrumented treadmill were sampled at 2000 Hz and treadmill belt velocities were logged at approximately 70 Hz. 67 reflective markers (modified Human Body Model 2; (van den Bogert et al., 2013)) were placed on the bony landmarks

and major body segments (head, hands, forearms, upper arms, torso, pelvis, thighs, shanks, and feet) of each participant. A 10-camera motion capture system (Vicon; Oxford, UK) collected 3D marker trajectories at 200 Hz. For each participant, a static trial was used to scale an individualized version of the generic full body musculoskeletal model developed by Rajagopal and colleagues (37 degrees of freedom, 22 rigid bodies;(Rajagopal et al., 2016)) in OpenSim v. 4.0 (Delp et al., 2007). Trials where participants crossed over the belts, as determined by manual inspection, were removed from analysis, leaving 222 successful trials.

3.3.3   Leg Mechanical Energetics

To calculate a "ground truth" estimate of the overall mechanical powers of each leg, we used a modified version of the individual limbs method (Donelan et al., 2002b; Selgrade et al., 2017; Zelik et al., 2015). This "corrected" overall leg power (as opposed to summing lower limb joint powers) was the sum of 1) the power flowing from each leg to the treadmill, 2) the power flowing from each leg to the COM, and 3) the peripheral powers of the leg segments (thigh, shank, and foot) relative to the COM. The power from the leg to the treadmill was calculated as the dot product of the force from each leg on the ground (equal and opposite to ground reaction force) with the velocity of the respective treadmill belt. The power from each leg to the COM was calculated as the dot product of each ground reaction force and the velocity of the whole-body COM. Whole-body COM kinematics were calculated using the scaled musculoskeletal models and the OpenSim Body Kinematics tool. This kinematic COM estimate was selected instead of estimates based on GRF (Donelan et al., 2002b; Sánchez et al., 2019; Selgrade et al., 2017) because GRF-based estimates of COM velocity solve for integration constants assuming steady-state

behaviour over multiple strides, but such integration constants may not be valid during perturbed strides. Peripheral power of the leg segments was calculated by summing the time derivative of the rotational and translational components of kinetic energy (Cavagna and Kaneko, 1977; Willems et al., 1995; Zelik et al., 2015).

3.3.4   Joint Mechanical Engergetics

Joint level powers were calculated as the product of joint angular velocities and joint moments. Joint angular velocities were calculated as the time derivative of joint angles produced using the OpenSim inverse kinematics tool. Joint moments were calculated with the OpenSim inverse dynamics tool using both the joint angles and bilateral ground reaction forces applied to the calcanei of the scaled models. Joint kinematics and kinetics were lowpass filtered using 4th order zero-phase Butterworth filters at 6 and 15 Hz, respectively. Strides were segmented using a 30 N threshold applied to vertical ground reaction forces. To calculate summed joint power, joint powers about each available degree of freedom were summed (ankle plantar/dorsiflexion, knee flexion/extension, hip flexion/extension, hip ab/adduction, and hip external/internal rotation). The metatarsophalangeal and subtalar joints of the models were locked in all analyses, thereby assuming the foot was a rigid body. To estimate leg power most accurately from joint power, 6 degree of freedom joint powers and a deformable segment model for the foot are preferred (Buczek et al., 1994; Duncan et al., 1997; Takahashi et al., 2012; Zelik et al., 2015), but such calculations are not compatible with model-based OpenSim analysis that constrains joints to behave within physiological bounds. Sagittal plane joint angles and moments are not explicitly discussed in this work but are included in electronic supplementary material (Figure 8 and Figure 9, respectively). Mechanical work at the

levels of the joints and legs was calculated using trapezoidal integration of powers with respect to time.

3.3.5 Statistical Analysis

All statistical analyses were performed in Matlab R2019b (Mathworks, Natick, MA, USA). Continuous outcome measures (*i.e.*, gait-cycle normalized profiles of power, force, velocity, etc.) of the early and late stance perturbation conditions were compared to steady state profiles using statistical parametric mapping (SPM) to perform paired t-tests (Pataky et al., 2015). This method evaluates the probability that smooth random curves would produce differences as large as those observed in the data and avoids the need to correct for multiple comparisons based on the number of data points in the traces. While we reported all statistical differences, readers should note that since the perturbations altered stride times and all profiles were normalized to the gait cycle, this produced some small phase shifts between perturbed and steady state traces. As a result, some statistical differences were found between curves during periods of low variance and/or high slope which we did not interpret as being meaningful. For discrete outcome measures (*i.e.*, mechanical work), a conventional paired t-test was used to compare the two perturbation conditions to steady state levels. For H3, linear regressions were used to relate changes in corrected leg work with changes in ankle, knee, and hip work. For these regressions, changes in leg and joint work were calculated relative to steady state strides (*i.e.*, the work of stride S+N – work of stride S-1). Significance was concluded for p-values ≤ 0.05.

3.4 Results

3.4.1 H1 – Effect of Perturbation Timing on Work Performed by the Perturbed Leg on the Treadmill

Both early and late stance perturbations elicited significant deviations in velocity, anteroposterior leg force, and power flowing from the leg to the treadmill on the perturbed side, relative to steady state (Figure 4).

For early stance perturbations, the increased posterior velocity ($p<0.001$; Figure 4A) resulted in a larger anterior leg force before midstance ($p<0.001$; Figure 4B), and a larger posterior leg force in late stance ($p<0.001$). The increased anterior leg force in early stance coupled with increased posterior velocity resulted in increased negative power flowing from the perturbed leg to the treadmill belt in early stance ($p<0.001$; Figure 4C), as we hypothesized. However, the increased posterior force in late stance also resulted in increased positive power flowing from the leg to the treadmill ($p<0.001$). There was no significant difference in the net work performed by the perturbed leg on the treadmill over the stride relative to steady state ($p=0.912$; Figure 4G).

Late stance perturbations increased posterior velocity ($p<0.001$; Figure 4D), but had a limited effect on anteroposterior leg force, aside from a shift to more anteriorly directed force at approximately 40% of the gait cycle ($p<0.001$; Figure 4E). As hypothesized, there was significantly increased positive power flowing from the leg to the treadmill in late stance ($p<0.001$; Figure 4F), which resulted in a significant increase in net work performed by the perturbed leg on the treadmill over the stride relative to steady state ($p=0.033$; Figure 4G).
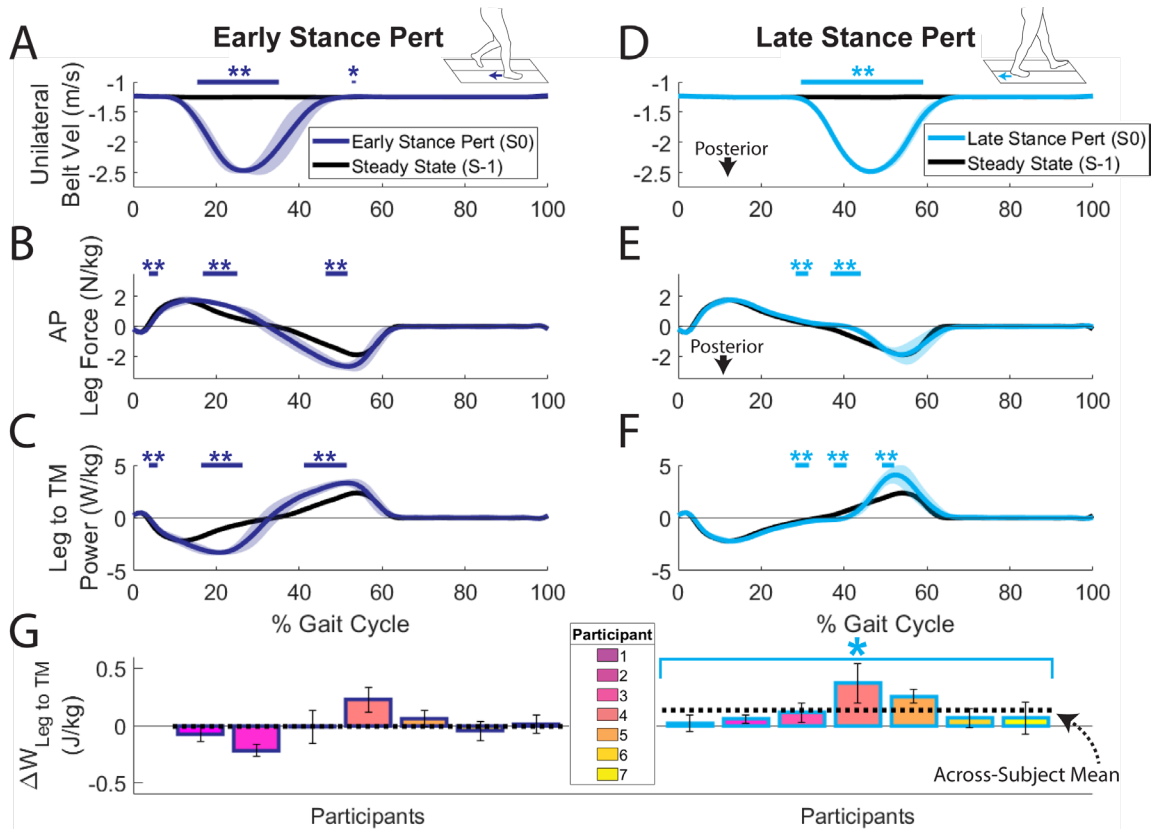
Figure 4 – Results addressing H1: that early/late stance perturbations would elicit net negative/positive work, respectively, performed by the perturbed leg on the treadmill. Across-subject ensemble average A,D) unilateral belt velocity traces, B,E) anteroposterior forces exerted by the perturbed leg on the treadmill belt, and C,F) power flowing from the leg to the treadmill belt. Instances when curves significantly deviated from steady state (S-1) are identified with thick horizontal lines and ** for p < 0.001, and thin horizontal lines and * for p < 0.05. G) Power flowing from the perturbed leg to the treadmill was integrated in time to calculate the work contribution over the perturbed stride (S0). These values were subtracted from their respective measurements during steady state strides (S-1) to quantify the changes in mechanical work at the leg/treadmill interface because of the perturbation. Statistical outcomes represent results of paired t-tests comparing work between the S0 vs. S-1 strides. * = p < 0.05. Shaded regions (A-F) and error bars (G) represent ±1 standard deviation. See supplementary Figure 10 for 3D leg and ground reaction forces.

3.4.2 H2 – Effect of Perturbation Timing on Overall Corrected Leg Work

All three components of overall corrected leg power were influenced by each of the perturbation timings (Figure 5). For early stance perturbations, significantly less negative power flowed from the perturbed leg to the COM in late stance (p<0.001; Figure 5Ai),

which resulted in net positive work being performed by the leg on the COM over the perturbed stride relative to steady state ($p<0.001$, Figure 5C, top row). Significantly more positive peripheral COM power was found in early stance ($p<0.001$), and more negative peripheral COM power was found at the end of swing ($p=0.005$). These peripheral COM power changes, in addition to changes that did not reach significance in late stance, resulted in no net change in peripheral COM work relative to steady state ($p=0.170$). Since there was no change in work performed by the perturbed leg on the treadmill (see section 1.10.1), combining all components of corrected leg work we found there was net positive work performed by the overall leg relative to steady state ($p=0.037$), in contrast to our hypothesis that there would be net negative work.

For late stance perturbations, significantly more negative power flowed from the perturbed leg to the COM in late stance ($p<0.001$; Figure 5Aii), which resulted in net negative work being performed by the leg on the COM over the perturbed stride relative to steady state ($p<0.001$, Figure 5C, top row). Though there were significant deviations in peripheral COM power in late stance ($p<0.001$), as was the case for early stance perturbations, these changes cancelled to result in no change in net peripheral COM work relative to steady state ($p=0.291$). Altogether, the net positive work performed by the leg on the treadmill (see section 1.10.1) cancelled with the net negative work performed by the leg on the COM to result in no net change in overall leg work relative to steady state for the late stance perturbations ($p=0.848$). This was in contrast to our hypothesis that late stance perturbations would result in net positive work.
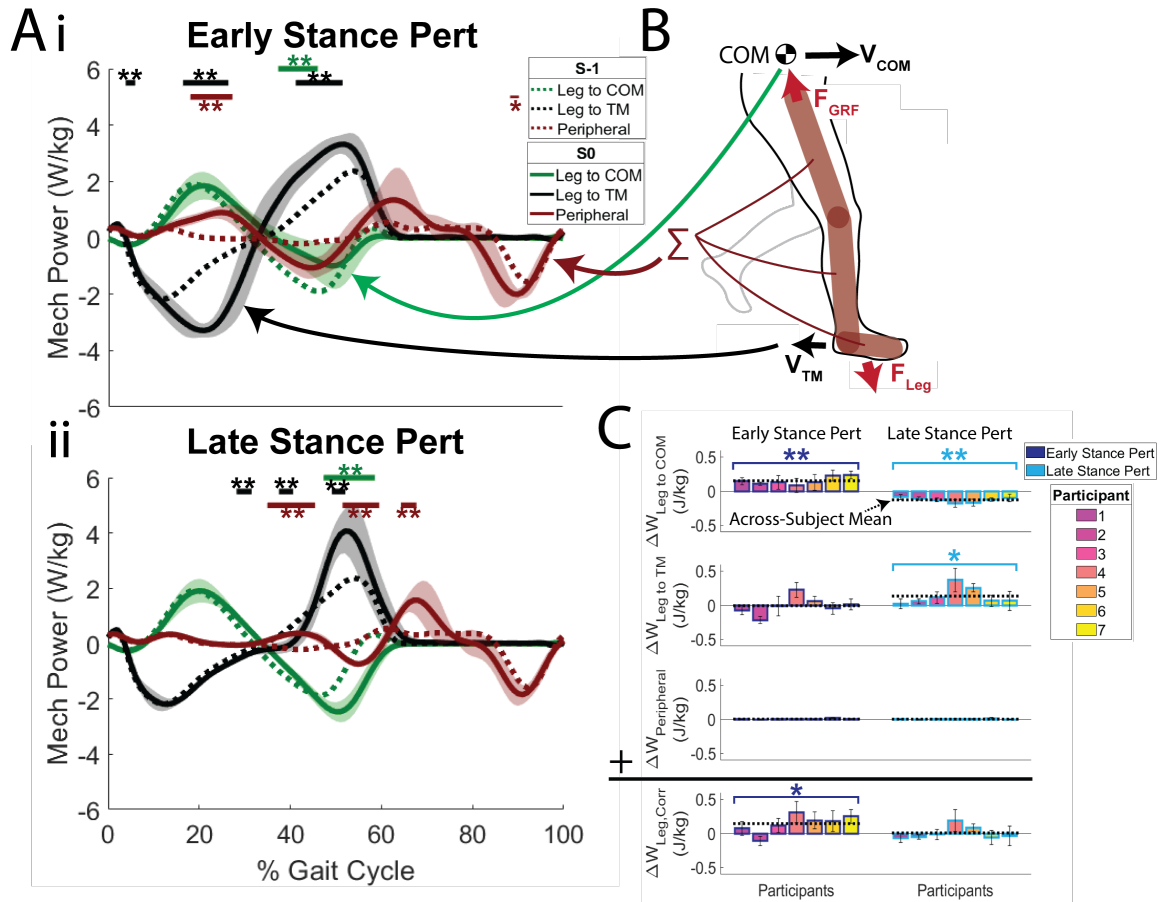
Figure 5 – Results addressing H2: that early/late stance perturbations would elicit net negative/positive work, respectively, performed by the *overall leg* stemming from demands at the leg/treadmill interface. A) Leg mechanical power breakdown for early stance (i) and late stance (ii) perturbations on the ipsilateral leg during the perturbed stride (S0, solid lines), and the unperturbed stride (S-1, dotted lines). For each perturbation timing, across-subject ensemble averages of the contributions to corrected individual leg power are shown (*i.e.*, mechanical power flowing from the leg to the centre of mass, power flowing from the leg to the treadmill, and peripheral power of leg segments moving relative to the centre of mass, all relative to a fixed lab frame). Shaded regions represent ±1 standard deviation. Instances when curves significantly deviated from steady state (S-1) are identified with thick horizontal lines and ** for p < 0.001, and thin horizontal lines and * for p < 0.05. B) Graphical representation of contributions to corrected leg power. See sections 2.3 and 2.4 for a description of power calculations. C) Contributions to corrected leg power were integrated in time to calculate the work contributions over the perturbed stride (S0). These values were subtracted from their respective measurements during steady state strides (S-1) to quantify the changes in mechanical work of these contributions because of the perturbation. Error bars represent ±1 standard deviation. Statistical outcomes represent results of paired t-tests comparing work between the S0 vs. S-1 strides. * = p < 0.05, ** = p < 0.001

3.4.3   H3 – Relating overall leg to joint level energetics

While across-subject analyses did not support H2, we found there was appreciable variability both within and among participants in the corrected leg work for both early and late stance perturbations (Figure 5C, bottom row). To investigate joint-level contributions to overall leg responses, we first assessed the agreement between corrected leg power and summed joint powers for the perturbed leg and stride (Figure 6), then compared corrected leg work with individual joint work over the perturbed stride and first two recovery strides on both the perturbed (ipsilateral) and unperturbed (contralateral) legs (Figure 7).

On the perturbed leg and stride, agreement between corrected leg power and summed joint leg power was stronger for early stance perturbations than late stance perturbations ($R^2 = 0.82$ for early, $R^2 = 0.54$ for late). For both timings (thus likely not a result of the specific perturbations themselves), deviations in power curves were apparent just after initial heelstrike and in mid-swing. For early stance perturbations specifically, agreement significantly deviated at perturbation onset, with more negative corrected leg power than summed joint power ($p<0.001$; Figure 6Ai). For late stance perturbations specifically, there was significantly more negative power during push-off for the summed joint power than the corrected leg power ($p=0.006$; Figure 6Aii).

The largest changes in joint powers from steady state generally occurred during the perturbed stride (Figure 6B). Early stance perturbations elicited more negative power followed by a greater duration of positive power at the ipsilateral ankle ($p<0.001$), in addition to more positive power during midstance at the ipsilateral hip ($p< 0.001$). On the contralateral side, early stance perturbations elicited more negative power at the knee at

the end of contralateral swing (p<0.001). Late stance perturbations elicited more negative power at the ipsilateral knee and positive power at the ipsilateral hip in late stance, though these deviations did not reach significance. On the contralateral side, late stance perturbations elicited increased positive power at the knee (p<0.001) and negative power at the hip (p<0.001) during contralateral loading response. For both early and late stance perturbations, there was less positive push-off power at the ankle on the first recovery stride (p<0.001).
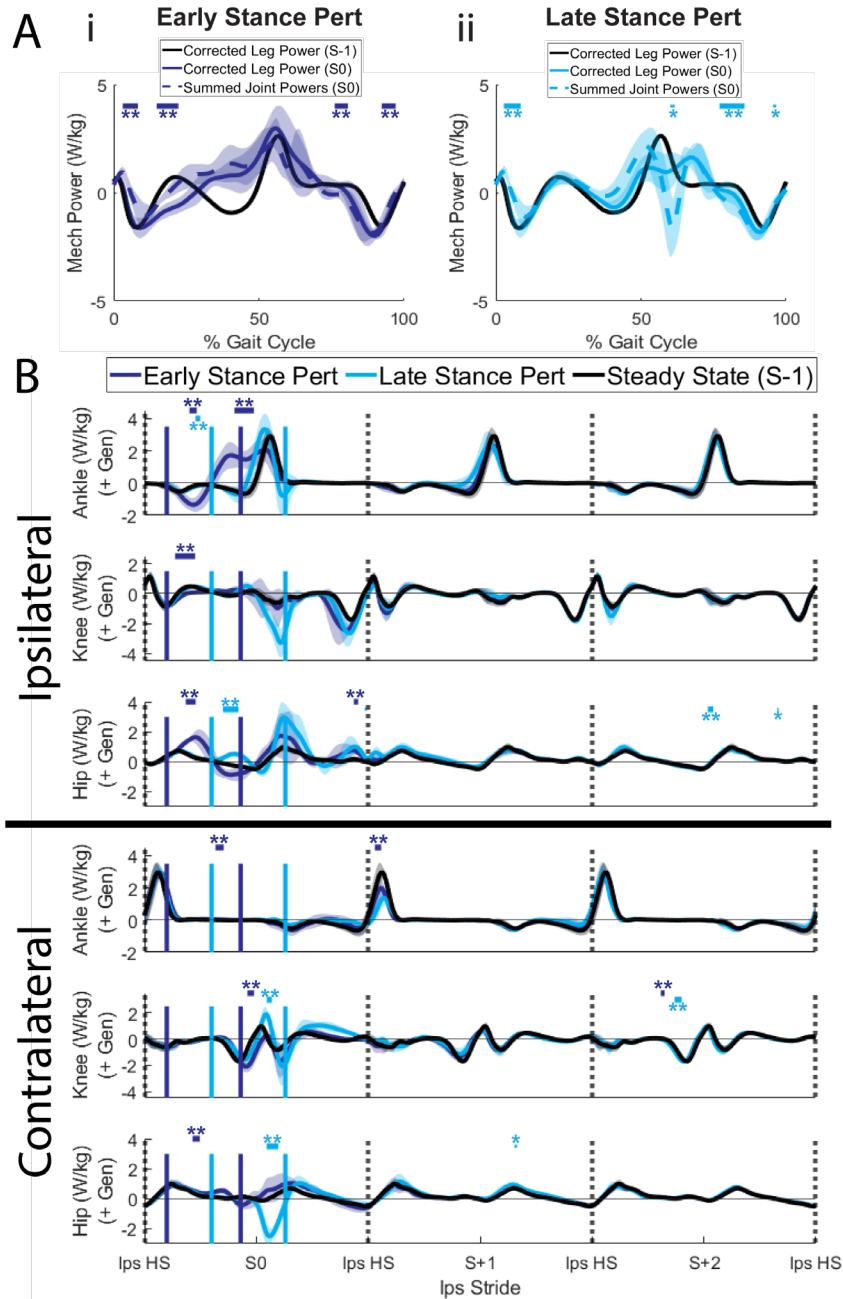
Figure 6 - Results relating joint and leg powers for H3. A) Comparison of corrected leg power and summed joint powers for early (i, $R^2 = 0.82$) and late stance (ii, $R^2 = 0.54$) perturbations. Instances when summed joint and corrected leg power curves significantly deviated are identified with thick horizontal lines and ** for $p < 0.001$, and thin horizontal lines and * for $p < 0.05$. B) Sagittal plane lower limb joint mechanical powers averaged across subjects and normalized to percentage of the gait cycle. Instances when curves significantly deviated from steady state (S-1) are identified with thick horizontal lines and ** for $p < 0.001$, and thin horizontal lines and * for $p < 0.05$. Shaded areas represent ±1 standard deviation. Solid vertical lines indicate the average start and end times of the perturbations. "Steady State" strides were the strides preceding the perturbed stride (S-1).

Relating individual joint work with corrected leg work indicated that on the perturbed stride, changes in ipsilateral ankle ($R^2 = 0.56$, Figure 7i) and contralateral knee work ($R^2 = 0.67$, Figure 7ii) best reflect changes in overall leg work as a result of the perturbation. On the first recovery stride, changes in ipsilateral ankle ($R^2 = 0.60$, Figure 7iii) and hip work ($R^2 = 0.39$, Figure 7iv) best reflected changes in corrected leg work.
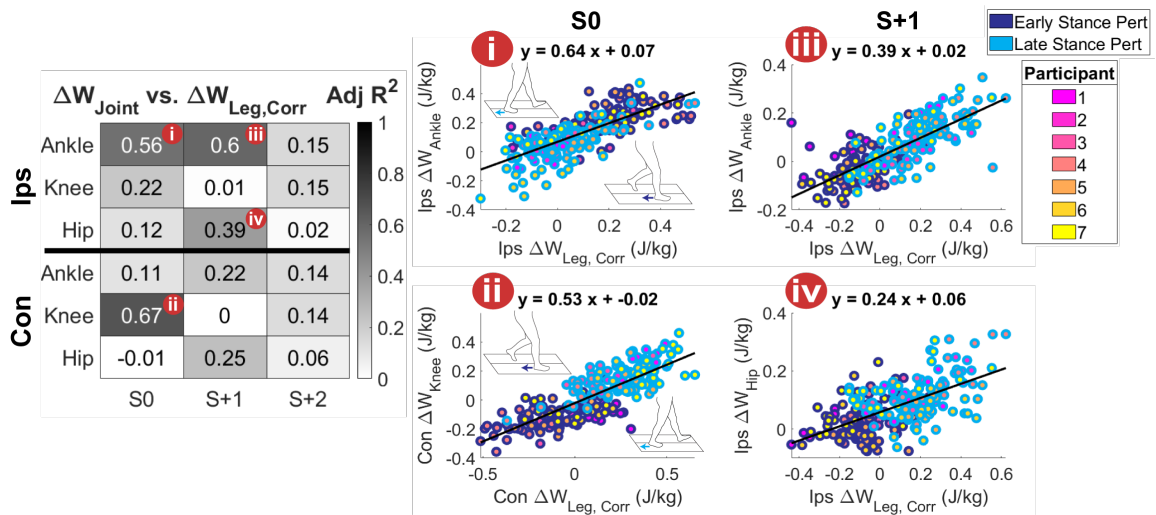
Figure 7 – Results relating joint and corrected leg work for H3. Adjusted R squared values for linear regressions between differences in joint work over a stride from steady state, and differences in corrected leg work over a stride from steady state (S-1) across all 222 perturbations. (i-iv) Scatter plots for joint/stride with the highest adjusted R squared values.

3.5 Discussion

The main objective of this work was to relate overall leg and joint level responses to destabilizing perturbations during walking using mechanical energetics. We used a split-belt treadmill to elicit transient mechanical energetic demands on the legs during walking and investigated which joints best reflected those demands. Our first hypothesis (H1) was that unilateral belt accelerations delivered in early or late stance would elicit net negative or positive work, respectively, from the perturbed leg at the leg/treadmill interface over a

stride. Our data supported this hypothesis for late stance perturbations, but not for early stance perturbations. In the case of early stance perturbations, while more negative power was elicited from the leg at the leg/treadmill interface in early stance, the posterior movement of the leg caused by the perturbation led to a more posteriorly directed leg force ((Debelle et al., 2020) , Figure 4B). This posterior leg force resulted in more positive power flowing from the leg to the treadmill in late stance, and no change in net work over a stride by the perturbed leg on the treadmill belt. Thus, future work seeking to specifically elicit net negative work at the leg/treadmill interface over a stride should consider decelerating the targeted treadmill belt during late stance, thereby avoiding unexpected compensations to the perturbation.

Our second hypothesis (H2) was that changes in net work at the leg/treadmill interface over the perturbed stride would be reflected by changes in overall leg work. Our data did not support this hypothesis for either early or late stance perturbations. For early stance perturbations, which we initially hypothesized would elicit net negative work from the perturbed leg, we found net *positive* work was generated by the leg. This occurred due to the combined effect of the net zero work performed by the leg on the treadmill coupled with less negative COM work in late stance. We attribute this decrease in negative COM work to a combination of 1) offloading of the perturbed leg around toe-off resulting in decreased negative COM power (electronic supplementary material, Figure 10), and 2) the perturbed leg accelerating the COM forward, as evidenced by an increased anteroposterior component of leg power (electronic supplementary material, Figure 11). For late stance perturbations, which we initially hypothesized would elicit net positive work from the perturbed leg, we found no net change in work performed by the leg. In this case, the

37

increased positive work performed by the leg on the treadmill was offset by the increased

negative work of the leg on the COM in late stance. Increased negative COM power

occurred despite the perturbed leg being offloaded, indicating the COM experienced a

larger downward velocity around toe-off during late stance perturbations (electronic

supplementary material, Figure 10 and Figure 11). Since the COM during double support

is closer to the ground with faster walking speeds (Orendurff et al., 2004), this downward

velocity may stem from the increased COM velocity caused by the perturbation coinciding

with late stance. An additional observation from the responses in overall leg work was the

diversity of responses particularly *among* participants, which was driven primarily by

differences in work at the leg/treadmill interface (Figure 5C). This emphasizes the need for

subject specificity in devices or interventions designed to improve perturbation response.

Our third hypothesis (H3) was that changes in net ankle work elicited by

perturbations would best reflect changes in net overall leg work. Although the energetic

demands imposed on the perturbed leg were not as hypothesized, our perturbations

nevertheless elicited both generation and dissipation, providing a rich dataset to relate leg

and joint level mechanical energetics. Our hypothesized contribution by the ankle was

supported on the perturbed stride and first recovery stride on the perturbed leg, with a large

percentage of the change in work of the perturbed leg being accounted for by the ankle

alone (64 and 39% for the perturbed and first recovery stride, respectively). While the

importance of the ankle joint in generating mechanical power during steady state walking

(Farris and Sawicki, 2012; Montgomery and Grabowski, 2018; Nuckols et al., 2020b) and

acceleration (Farris and Raiteri, 2017; Qiao and Jindrich, 2016; Schache et al., 2019) has

been established, our findings demonstrate that the ankle also plays an important role in

mediating transient demands, in agreement with previous studies of human hopping (Dick et al., 2019). However, in contrast to the perturbed leg, for the contralateral leg, the knee joint best reflected changes in leg work during the perturbed stride. While previous studies have identified the knee joint as a major contributor during tasks requiring dissipation, such as deceleration and drop landings (Qiao and Jindrich, 2016; Yeow et al., 2010), we found that the knee additionally reflected the mechanical work of the leg when generation was required. This could be explained by the knee being a major source of collisional and rebound work in early/midstance, as opposed to the ankle, which primarily contributes later in stance through push-off (Zelik et al., 2015). Further, previous work that disrupted ankle push-off found that both positive and negative knee energetics were significantly altered (Huang et al., 2015).

One technical limitation of this work was that joint power contributions did not fully account for corrected overall leg power, particularly during late stance perturbations. Since both the corrected leg power and summed joint power were calculated using the same ground reaction forces, and the respective curves for the contralateral leg on the perturbed stride were in better agreement ($R^2 = 0.90$ for early stance perturbations, 0.98 for late stance perturbations), the discrepancy between them is likely related to centre of pressure deviations altering moments during the perturbation. These deviations could be caused by acceleration or deceleration of the treadmill rollers inducing a moment and altering the centre of pressure (Hnat and van den Bogert, 2014; Moore et al., 2015). Additionally, modelling assumptions could propagate moment and power discrepancies from the foot to other joints. Future work seeking to overcome modelling discrepancies could consider using 6 degree of freedom-based inverse dynamics (Buczek et al., 1994; Duncan et al.,

39

1997; Zelik et al., 2015) vs. musculoskeletal model-based inverse dynamics, or a musculoskeletal model with free MTP and subtalar joints. Another important limitation of this work was the use of correlations to relate the joint and limb levels. While this approach suggests which joints reflect demands at the leg level, it does not establish whether those joint level responses *cause* changes at the leg level. Future work may further investigate the energetic link between joint and leg level responses by perturbing joint energetics and observing leg level responses, perhaps using wearable robots that inject/extract mechanical energy (Donelan et al., 2008; Shepertycky et al.; Witte et al., 2020). Further, future studies may also use other flavours of perturbations, such as belt decelerations (Afschrift et al., 2019; Roeles et al., 2018; Sloot et al., 2015), external pushes (Tant et al., 2020), or obstacles (King et al., 2019), to determine whether these findings generalize to other unstable contexts. Lastly, inverse dynamics can only quantify net joint powers and does not capture the contributions of muscle-tendon units to energy exchanges across either side of a joint (*e.g.,* coactivation (Abbott et al., 2019)), and between joints (*e.g.,* biarticular muscle tendon units (Iida et al., 2008)) which could be explored using musculoskeletal simulations, electromyography coupled with in-vivo imaging approaches, and animal models (Daley and Biewener, 2011; Dick et al., 2021; Lai et al., 2019).

In conclusion, we have demonstrated that a framework using mechanical energetics can be used to investigate joint level contributions to the energetic demand imposed by a transient treadmill-based perturbation during human walking. We found that the net energetic demand on the perturbed leg during the perturbed stride varied depending on the timing of the perturbation, with changes in net leg work stemming from both changes in power flowing from the leg to the COM and from the leg to the treadmill. The varied

energetic demands imposed across timings revealed that the ankle best reflected changes in energetics of the perturbed leg on the perturbed and first recovery strides, while the contralateral knee best reflected changes in energetics of the contralateral leg during the perturbed stride. We anticipate this work will serve as an initial step in using mechanical energetics to relate different levels of musculoskeletal description in unstable contexts.

3.6 Ethics

All participants provided written informed consent and all protocols were approved by the Institutional Review Board at the Georgia Institute of Technology (Protocol H20163).

3.7 Data Accessibility

Biomechanical data for all participants (N=7) is available at https://doi.org/10.5281/zenodo.6338829

3.8 Authors' Contributions

Pawel R. Golyski and Gregory S. Sawicki conceived of the study and designed the experimental protocol; Pawel R. Golyski carried out the experiments, analysed the data, and drafted the manuscript; Pawel R. Golyski and Gregory S. Sawicki edited the manuscript. Both authors gave final approval for publication.

3.9 Competing Interests

We declare no competing interests.

3.10 Funding

3.11 Acknowledgements
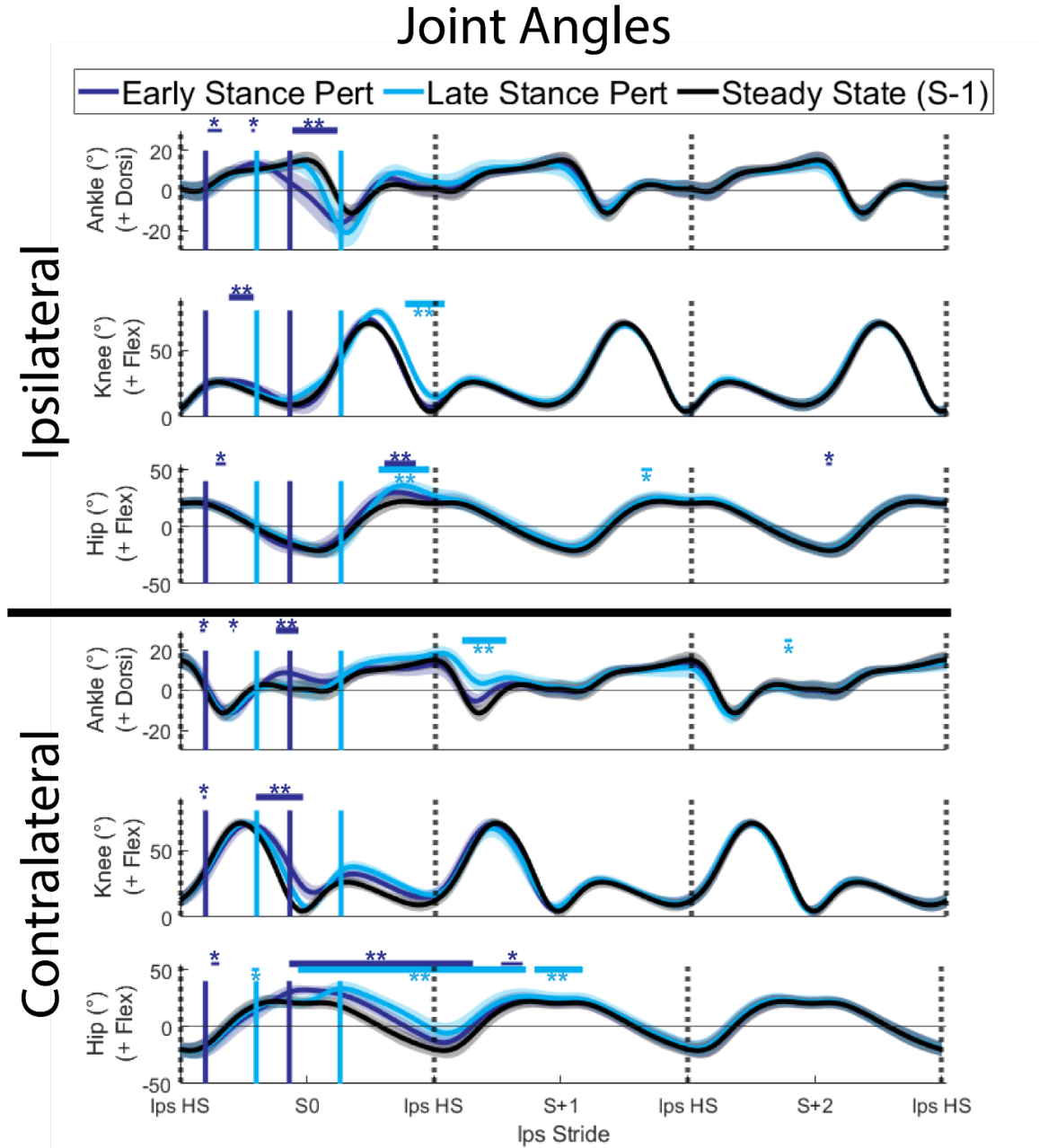
Joint Angles

Figure 8 – Sagittal plane lower limb joint angles averaged across subjects and normalized to percentage of the gait cycle. Instances when curves significantly deviated from steady state (S-1) are identified with thick horizontal lines and ** for p < 0.001, and thin horizontal lines and * for p < 0.05 Shaded areas represent ±1 standard deviation. Solid vertical lines indicate the average start and end times of the perturbations. "Steady State" strides are the stride preceding the perturbed stride (S-1).

Joint Moments
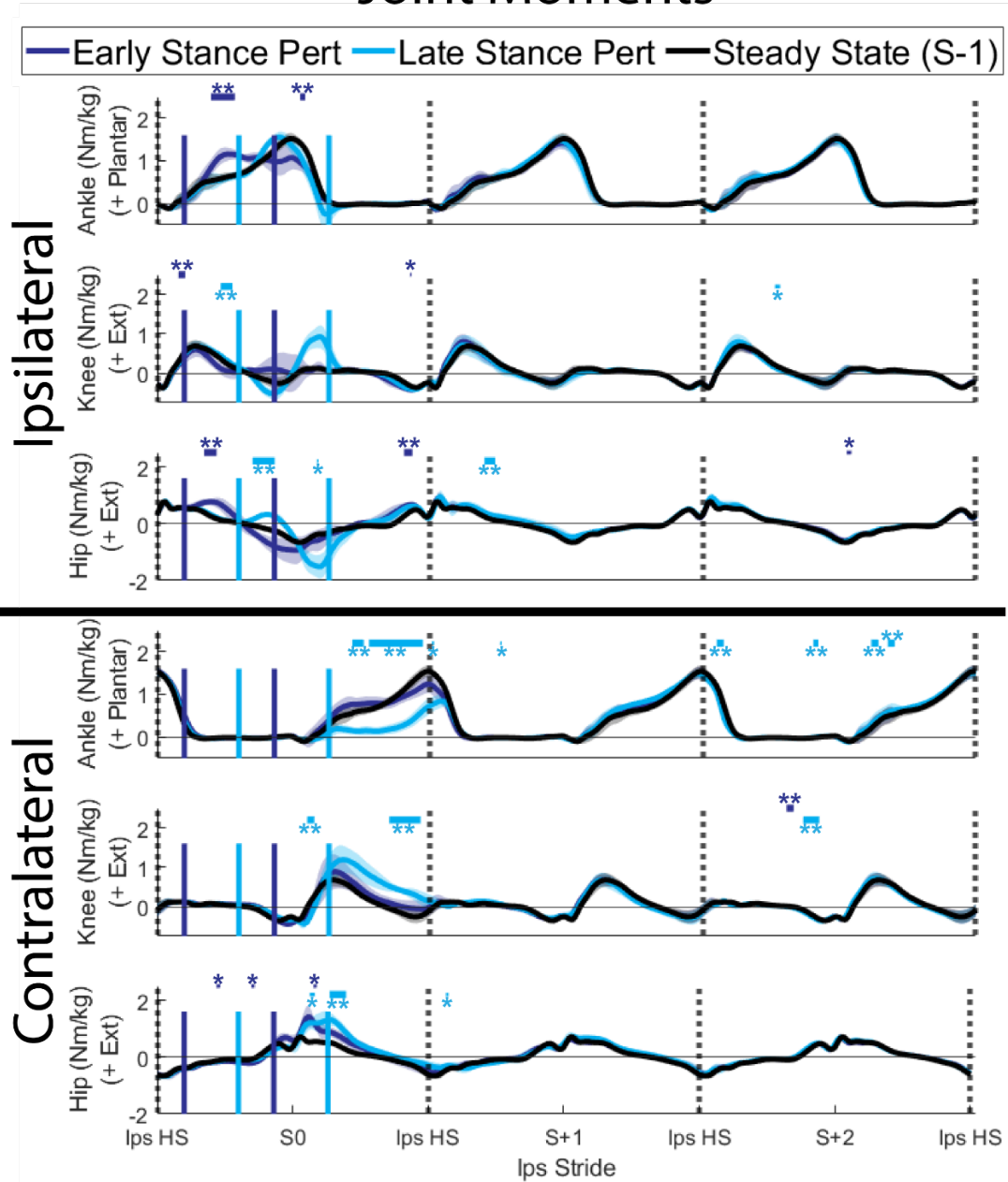
Figure 9 – Sagittal plane lower limb joint moments averaged across subjects and normalized to percentage of the gait cycle. Instances when curves significantly deviated from steady state (S-1) are identified with thick horizontal lines and ** for p < 0.001, and thin horizontal lines and * for p < 0.05. Shaded areas represent ±1 standard deviation. Solid vertical lines indicate the average start and end times of the perturbations. "Steady State" strides are the stride preceding the perturbed stride (S-1).
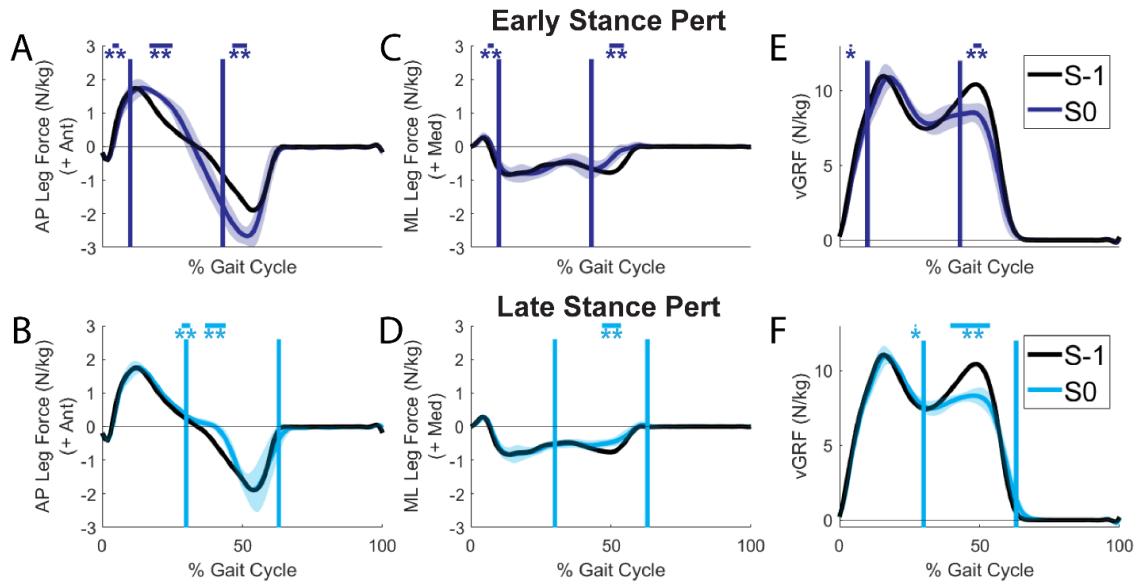
Figure 10 – Perturbed leg forces and vertical ground reaction forces separated into (A-B) anteroposterior, (C-D) mediolateral, and (E-F) vertical contributions during the perturbed stride (S0) and preceding unperturbed stride (S-1). Solid vertical lines indicate the average start and end times of the perturbations. Instances when curves significantly deviated from steady state (S-1) are identified with thick horizontal lines and ** for p < 0.001, and thin horizontal lines and * for p < 0.05.
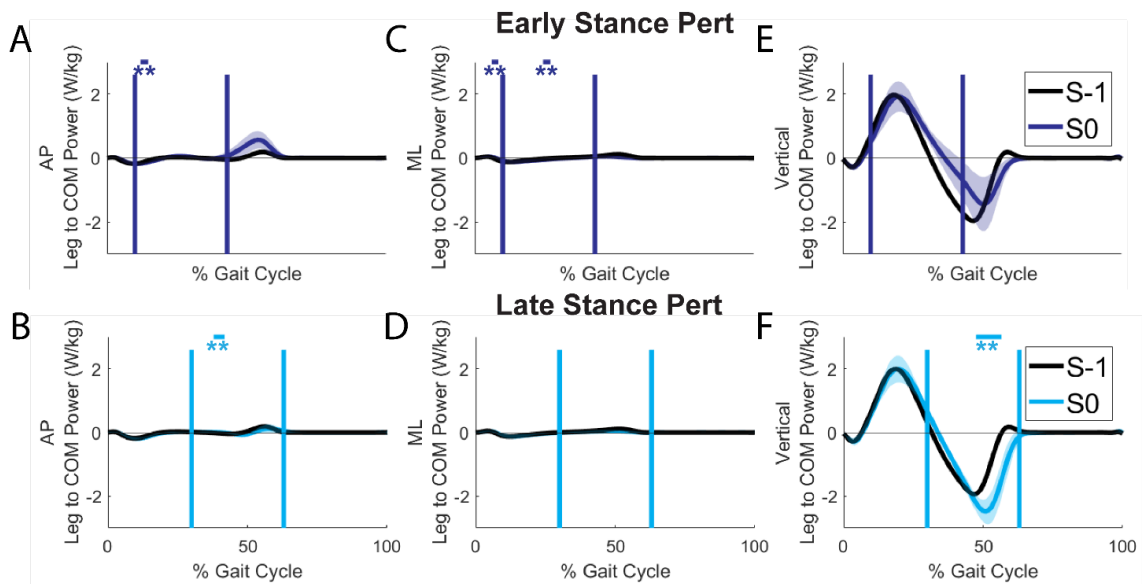
Figure 11 – Mechanical power flowing from the perturbed leg to the COM separated into (A-B) anteroposterior, (C-D) mediolateral, and (E-F) vertical contributions during the perturbed stride (S0) and preceding unperturbed stride (S-1). Solid vertical lines indicate the average start and end times of the perturbations. Instances when curves significantly deviated from steady state (S-1) are identified with thick horizontal lines and ** for p < 0.001, and thin horizontal lines and * for p < 0.05.

CHAPTER 4. MECHANICAL ENERGETIC CONTRIBUTIONS OF THE RECTUS FEMORIS DURING PERTURBED WALKING

The third work associated with my dissertation investigates the contributions of the rectus femoris to the energetics at the joint and overall leg levels. This chapter constitutes a manuscript draft that I intend to submit to the Journal of Experimental Biology.

4.1 Abstract

Animals can maintain locomotor stability following external perturbations through coordination of muscular responses that manifest at multiple levels of muscular description (*e.g.*, muscle-tendon units, joints, legs). To begin to understand the role of proximal musculature in responding to perturbations during human walking, here we extend a previous analysis relating joint and leg levels down to the level of the rectus femoris. Using *in-vivo* B-mode ultrasound processed with a custom fascicle tracking application and EMG measurements to drive Hill-type models of muscle force, we investigated mechanical energetics of the rectus femoris in 7 individuals who experienced rapid, transient unilateral belt accelerations during walking. We hypothesized that: H1) the rectus femoris fascicles and MTU on the perturbed leg would demonstrate negative power and work, H2) that on the contralateral leg the rectus femoris would reflect the energetic demand at the knee and leg levels, and H3) that the rectus femoris would transfer energy from the hip to knee joint. H1 was supported, with rectus femoris fascicles and the MTU being actively lengthened during the perturbation. H2 was not supported, with the rectus femoris best reflecting the energetic role of the hip, as opposed to the knee or leg. Support for H3 was mixed, with

the rectus femoris potentially acting in concert with the gastrocnemius to fulfill leg-level energetic demands. Overall, these findings provide a first estimate of the variety of roles of proximal muscles play in maintaining stability and lays the groundwork for additional *in-vivo* measurement informed multi-scale analyses of perturbed locomotion.

4.2 Introduction

As animals move through their environments, they exhibit an impressive ability to maintain stability despite external mechanical disturbances (*e.g.*, rocks, sidewalks, ice). The high-level goal of maintaining a locomotor trajectory without falling over is accomplished through stabilizing responses mediated by 1) feedforward strategies (*e.g.*, foot placement (Joshi and Srinivasan, 2019; Vlutters et al., 2016)), 2) feedback mechanisms (*e.g.*, reflexes (Nakazawa et al., 2004; Schillings et al., 2000)), and 3) intrinsic mechanical properties of biological structures (*e.g.*, muscle-tendon interactions (Daley and Biewener, 2011; Daley et al., 2009; Dick et al., 2021)). While stabilizing mechanical responses have been studied at different levels of musculoskeletal description (*e.g.*, center of mass [COM], legs, joints, muscles), relating responses *across* different levels remains a challenge. To address this challenge, a paradigm was recently developed which used mechanical energy to both quantify the explicit energetic demand of a perturbation and to serve as a "common currency" with which to relate responses across different levels of musculoskeletal description in humans (Golyski and Sawicki, 2022).

This approach leveraged the idea that during level split-belt treadmill walking, if both belts are moving at the same constant speed, both the net work performed by each leg on the COM and the corresponding treadmill belt must be zero over a stride on average, so

the net work performed by the overall leg (*i.e.*, the sum of both COM and treadmill contributions), must be zero as well (Sánchez et al., 2019; Selgrade et al., 2017). Barring modeling inaccuracies, this overall leg work should be equal to the sum of the work of all lower limb joints (Zelik et al., 2015). In (Golyski and Sawicki, 2022), transient increases in unilateral belt speed were targeted to either early or late stance. In this non-steady state condition, net mechanical work was performed by each leg on the COM and the corresponding treadmill belt. The difference between these non-steady state overall leg and joint level mechanical work contributions and their corresponding steady-state values constituted the mechanical energetic demand of the perturbation. By relating changes in joint and overall leg work, this approach allowed for investigation of which joints best reflected leg level demands. For the perturbed leg, on both the perturbed and first recovery stride, changes in ankle (vs. knee or hip) work best reflected changes in overall leg work, in agreement with literature from speed and ground height changes (Daley et al., 2007; Dick et al., 2019; Farris and Raiteri, 2017; Qiao and Jindrich, 2016; Schache et al., 2019). However, on the contralateral side, the knee strongly reflected overall leg level demands which spanned both net positive and negative work during the perturbed stride. This finding suggested proximal joints and muscles of the leg may play an important role in mediating transient energetic demands.

The goal of this work is to extend the perturbation energetics paradigm and investigate the role of proximal leg musculature in responding to rapid unilateral belt accelerations. As there is currently no gold-standard approach to measuring fascicle lengths of proximal muscles during dynamic tasks, to accomplish our overarching goal we developed a custom semiautomated application which uses aspects of other recent

algorithms (Marzilger et al., 2018; van der Zee and Kuo, 2020; van der Zee and Kuo, 2022) to estimate fascicle lengths from B-mode ultrasound images. These fascicle lengths were coupled with *in vivo* muscle activations to estimate fascicle and MTU forces (Dick et al., 2017), in addition to the respective mechanical powers. Of the quadriceps and hamstring muscles, we focused our analysis on the rectus femoris because 1) we sought to determine whether the extension of the perturbed limb by the perturbation would be apparent at the level of proximal muscle fascicles, as opposed to being buffered by series elasticity (Dick et al., 2021; Konow and Roberts, 2015), 2) an increased knee extensor moment is a major feature of the recovery strategy on the contralateral side following a belt acceleration during walking (Debelle et al., 2020), and 3) as a biarticular muscle it allows for interrogation of the shuttling of mechanical energy between joints (Bobbert et al., 1986; Jacobs et al., 1996; Prilutsky and Zatsiorsky, 1994). Since proximal muscles are considered to have less compliant tendons relative to distal muscles (Arampatzis et al., 2006; Biewener and Roberts, 2000), our first hypothesis (H1) was during the perturbed stride and on the perturbed leg, for perturbations in both early and late stance, rectus femoris fascicles would lengthen relative to steady state, which when coupled with increased muscle activation to flex the hip and extend the knee (Debelle et al., 2020), would result in negative fascicle and MTU power and work. On the contralateral leg, because the knee reflected overall leg level energetic demands (Golyski and Sawicki, 2022), and the functional behavior of the rectus femoris fibers and MTU (predominantly damper-like; [Lai et al., 2019]) is more similar to the knee than the hip (predominantly motor-like; [Qiao and Jindrich, 2016]), our second hypothesis was that the rectus femoris would reflect contralateral knee energetic demands and therefore also overall leg energetic demands. Lastly, informed by previous

simulations investigating biarticular energy transfers during leg extension tasks (Jacobs et al., 1996), our third hypothesis (H3) was that the rectus femoris would facilitate the transfer of energy from the hip to the knee joint.

4.3 Methods

4.3.1 Experimental Protocol

Data were collected from 7 healthy able-bodied individuals (5 males, 2 females, mean [SD]: 25 [2] years, 178.5 [12.1] cm stature, 72.7 [13.3] kg) as part of a study investigating leg and joint level energetics (Golyski and Sawicki, 2022). Participants walked on an instrumented split-belt treadmill (CAREN, Motek, Netherlands), and after 5 minutes of acclimation at 1.25 m/s (Zeni and Higginson, 2010), experienced rapid (15 m/s^2 acceleration), transient (~340 ms duration, ~33% of the perturbed gait cycle) increases in unilateral belt speed (1.25 m/s to 2.5 m/s) targeted to either early or late stance (Figure 12A). The algorithm by which these perturbations were delivered is described elsewhere (Golyski et al., 2021). Each participant experienced 40 total perturbations in a randomized order (both legs, early and late stance onset timings, and 10 repetitions of each leg/timing combination), with 30-40 steps between perturbations to allow for return to steady state walking (Liu et al., 2018). All participants provided informed consent as approved by the local Institutional Review Board.

4.3.2 External Kinematics and Kinetics

As also specified in (Golyski and Sawicki, 2022), ground reaction forces were collected at 2000 Hz from an instrumented split-belt treadmill (CAREN, Motek,

Netherlands). A full-body marker set consisting of 67 retroreflective markers (modified Human Body Model 2; (van den Bogert et al., 2013)) was used to track bony landmarks and body segments (head, hands, forearms, upper arms, torso, pelvis, thighs, shanks, and feet). Marker trajectories were collected at 200 Hz using a 10-camera motion capture system (Vicon; Oxford, UK). For each participant, a generic full-body musculoskeletal model (22 segments, 37 degrees of freedom; (Rajagopal et al., 2016)) was scaled in OpenSim 4.0 (Delp et al., 2007) using a static standing trial to generate a participant-specific model. The metatarsophalangeal and subtalar joints were locked to treat the foot as a rigid body. All trials were manually inspected to ensure crossover steps were removed from analysis, leaving 222 successful trials. Joint angles were calculated from marker trajectories using the OpenSim Inverse Kinematics tool. Joint moments were calculated with the OpenSim Inverse Dynamics tool using both joint angles and ground reaction forces applied to the calcanei of the scaled models. Time-varying moment arms of the rectus femoris to the hip and knee joints in addition to MTU lengths and velocities were calculated using the OpenSim Muscle Analysis tool using joint angles and the scaled models. Kinematic and kinetics were low-pass filtered using 4th order zero-phase Butterworth filters with cutoff frequencies of 6 and 15 Hz, respectively. Strides were segmented using a 30 N threshold applied to vertical ground reaction force.

4.3.3   Leg and Joint Energetics

Joint mechanical powers were calculated as the product of joint angular velocities (obtained by differentiating joint angles with respect to time) and joint moments. Mechanical powers of each leg were calculated using a modified individual limbs method (Donelan et al., 2002b; Zelik et al., 2015) as the sum of 1) power flowing from each leg to

51

the center of mass (COM), 2) power flowing from each leg to the treadmill, and 3) peripheral power of the leg segments moving relative to the COM of the whole body. Leg to COM power was calculated as the dot product of the corresponding ground reaction force and COM velocity. COM velocity was calculated as the time derivative of COM position from the Body Kinematics tool in OpenSim using both joint angles and scaled models. Leg to treadmill power was calculated as the product of anteroposterior leg force (equal and opposite to ground reaction force) and treadmill velocity (collected at approximately 70 Hz). Peripheral leg power was quantified by adding together the time derivatives of the rotational and translational components of kinetic energy of the leg segments (Cavagna and Kaneko, 1977; Willems et al., 1995; Zelik et al., 2015) as calculated from inertial estimates from the scaled models and segment velocities from the OpenSim Body Kinematics tool.

4.3.4   Electromyography

Surface electromyography (EMG) was collected at 2000 Hz (Avanti, Delsys, Natick, MA) from 7 lower limb muscles of the left leg: the rectus femoris (RF), tibialis anterior (TA), soleus (SOL), medial gastrocnemius (MG), vastus medialis (VM), biceps femoris (BF), and gluteus maximus (GM). EMG sensors were placed on the bellies of each muscle following light abrasion of the skin surface. All EMG envelopes were calculated by first high-pass filtering EMG signals using a 10 Hz zero-phase Butterworth filter, then full-wave rectifying the signal, then low-pass filtering the signal with a 30 Hz zero-phase Butterworth filter (Arnold et al., 2013; Buchanan et al., 2004). Signal offsets were first removed by subtracting the minimum envelope value during a relaxed static trial. These demeaned envelopes were then normalized by the difference between the maximum

within-participant envelope value across all perturbations and the minimum resting value, similar to previous work (Arnold et al., 2013; Nuckols et al., 2020a). To estimate muscle activations, this normalized signal was then passed through first-order dynamics (Zajac, 1989) with an activation time constant of 35 ms, and a deactivation time constant of 58 ms, corresponding to a mixed fiber type muscle (Dick et al., 2017), which is applicable to the RF (Johnson et al., 1973). Since the RF is the primary muscle of interest in this work, activations of other muscles are included as a supplementary figure (Figure 17).

4.3.5   Ultrasonography

B-mode cine ultrasound images were collected at approximately 115 Hz from the right RF using an ArtUS EXT-1H acquisition unit and a 60 mm long LV8-5N60-A2 probe (Telemed, Vilnius, LT). The probe was placed over the muscle belly at a consistent longitudinal location to the RF EMG sensor on the left leg. The probe was aligned such that fascicles and both superficial and deep aponeuroses could be clearly visualized. The imaging angle of the probe was also varied in EchoWave software (Telemed, Vilnius, LT) to provide the best contrast of the fascicles and aponeuroses – between 0 and -10 degrees based on the participant. An external trigger was used to synchronize motion capture and ultrasound image timestamps.

4.3.5.1   Custom Ultrasound Tracking Application

A custom semiautomated application was developed in Matlab R2019b (Mathworks, Natick, MA, USA) which was used for tracking proximal muscle fascicle lengths from B-mode ultrasound images during dynamic tasks leveraging a combination of techniques from literature. Use of the application can be separated into 5 steps (Figure

12B). <u>First</u>, the raw image, with fascicles running from top left to bottom right, is filtered using adaptive histogram equalization (adapthisteq, Matlab) to improve contrast of hyperechoic structures. To account for angled images, the user is prompted to enter the image angle, which is used to first shear the image to have vertical edges, then applies adaptive histogram equalization, then de-shears the image to return it to the original angle. This step is necessary as the border outside an angled image introduces artifacts during filtering. <u>The second step</u> is manual selection of the aponeuroses. This constitutes the only step requiring user input on every frame, with steps 3-5 occurring automatically in approximately 0.2 seconds. The user must select the vertices marking the border of the muscle of interest (roipoly, Matlab) from top left going counterclockwise (*i.e.,* leftmost vertex of superficial aponeurosis, then leftmost vertex of deep aponeurosis, then rightmost vertex of deep aponeurosis, then rightmost vertex of superficial aponeurosis). The aponeuroses are identified as first order polynomials based on these vertices. <u>The third step</u> is automatic detection of "snippets" of fascicles from hyperechoic streaks in the image. From the filtered image, the area between the aponeuroses is identified as the region of interest, with all structures outside of that area being removed. The region of interest is binarized (imbinarize, Matlab) using a Frangi-type vessel enhancement filter (fibermetric, MATLAB) as has been used in previous tracking algorithms (Frangi et al., 1998; Ryan et al., 2019; van der Zee and Kuo, 2022). From this binarized image, the area, centroid, orientation, and major axis length of each separate structure are computed (regionprops, Matlab). Only structures fulfilling specified criteria are used to calculate representative fascicle measurements. Specifically, each acceptable snippet must have more than 8 pixels, a minimum major axis length of 35 pixels (4 mm), an area to major axis length ratio of less

than 12, and a pennation angle relative to the deep aponeurosis of between 6.7 and 18.3 degrees. Aside from pennation angle, criteria were selected to be similar to that of a previous semiautomated algorithm validated on the vastus lateralis (Bohm et al., 2018; Marzilger et al., 2018). The acceptable range of pennation angles was selected to be between 1 standard deviation less than the minimum average pennation angle and 1 standard deviation more than the maximum average pennation angle from a previous study of RF architecture (Blazevich et al., 2006). To improve computational tractability, a maximum of 30 snippets are used for each frame. If more than 30 snippets are identified on a frame, the list of snippets is first sorted so snippets with centroids less than 5 pixels from the centroid of a snippet on the previous frame (*i.e.,* likely the same snippet; nearestNeighbor, Matlab). That list is then sorted by major axis length, with the longest 30 snippets being accepted for representative fascicle calculations (Marzilger et al., 2018). The fourth step is assessment of a mean thickness of the muscle. This is calculated by taking the average of the lengths of 17 equally longitudinally spaced lines that run perpendicular to the bottom aponeurosis and intersect the top aponeurosis (van der Zee and Kuo, 2020). The fifth step is calculating representative fascicle parameters. First, a representative pennation angle is calculated using a weighted average (by length) of all accepted snippets, similar to (Marzilger et al., 2018). The representative fascicle length is then calculated as the mean thickness divided by the sine of this representative pennation angle (Blazevich et al., 2006; Ryan et al., 2019; van der Zee and Kuo, 2020; van der Zee and Kuo, 2022). Functionality added to facilitate ease of use of the application includes: 1) the ability to adjust either superficial or deep aponeuroses separately, 2) estimation of aponeurosis locations (and therefore fascicle parameters) for cyclic tasks based on the first

cycle using keyframes in conjunction with linear interpolation (interp1, Matlab), 3) visualization of the ensemble averaged and time normalized fascicle lengths and pennation angles after completing processing of a trial, 4) when a file containing aponeurosis locations corresponding to the current trial is identified, the application will automatically recalculate all frames based on those data, and 5) a graphical output of representative fascicle length that updates with every frame with associated aponeurosis positions. An image of the application interface during use is included as a supplementary figure (Figure 18). For all subsequent analyses, fascicle lengths and pennation angles were low-pass filtered at 6 Hz with a zero-phase 4th order Butterworth filter. Fascicle velocities were calculated as the time derivative of filtered fascicle lengths.

4.3.6 Estimation of Fascicle and Muscle-Tendon Unit Energetics

Fascicle force was estimated from a Hill-type model of muscle force generation driven by a combination of experimentally measured fascicle lengths and muscle activations similar to (Dick et al., 2017):

$$F_{fas} = F_{max}[\hat{a}(t)\hat{F}_a(\hat{l}_{fas})\hat{F}_a(\hat{v}_{fas}) + \hat{F}_p(\hat{l}_{fas})] \qquad \text{Eq 6}$$

Where F_{max} was maximum fascicle force, $\hat{a}(t)$ was estimated muscle activation from EMG, $\hat{F}_a(\hat{l}_{fas})$ was the normalized relationship between active force and fascicle length, $\hat{F}_a(\hat{v}_{fas})$ was the normalized relationship between active force and fascicle velocity, and $\hat{F}_p(\hat{l}_{fas})$ was the relationship between passive force and normalized fascicle length. $\hat{l}_{fas}$ and $\hat{v}_{fas}$ were fascicle length and velocity, respectively, normalized to fascicle slack length, $l_{0,fas}$ (mean [stdev]: 122.6 [21.4] mm across all participants). $l_{0,fas}$ was

56

determined as the length when force began to appear in the tendon, which based on previous measurements of patellar tendon force in humans (Martin et al., 2018) was approximated for each participant to be the average fascicle length at 50% of the walking gait cycle at 1.25 m/s. MTU force was calculated as:

$$F_{MTU} = F_{fas} \cdot \cos(\alpha(t)) \qquad \text{Eq 7}$$

Where $\alpha(t)$ is pennation angle. Maximum fascicle force was calculated as:

$$F_{max} = \left(\frac{V_m}{l_{fas,opt}}\right)\sigma_0 \qquad \text{Eq 8}$$

Where V_m is muscle volume estimated from each participants height and mass (Handsfield et al., 2014), σ_0 is specific muscle stress (Roy et al., 1982; Spector et al., 1980), and $l_{fas,opt}$ is optimal RF fiber length estimated from scaled OpenSim models of each participant (Arnold et al., 2010). From (Azizi and Roberts, 2010; Otten, 1987), the normalized active force-length relationship was calculated as:

$$\hat{F}_a(\hat{l}_{fas}) = e^{-\left(\frac{\hat{l}_{fas}^{0.6}-1}{0.3}\right)^{2.3}} \qquad \text{Eq 9}$$

For normalized fascicle lengths greater than unity, the normalized passive force-length relationship (Millard et al., 2013) was calculated as:

$$\hat{F}_p(\hat{l}_{fas}) = 2.64\hat{l}_{fas}^2 - 5.30\hat{l}_{fas} + 2.66 \qquad \text{Eq 10}$$

For normalized fascicle lengths less than or equal to unity, the normalized passive force

was set to 0. For shortening fascicles ($\hat{v}_{fas} \leq 0$), the normalized force-velocity

relationship was given by (Otten, 1987):

$$\hat{F}_a(\hat{v}_{fas}) = \frac{1 + \left(\frac{\hat{v}_{fas}}{\hat{v}_0}\right)}{1 - \left(\frac{\hat{v}_{fas}}{\hat{v}_0 \beta}\right)} \qquad \text{Eq 11}$$

For lengthening fascicles ($\hat{v}_{fas} > 0$), the normalized force-velocity relationship was given

by:

$$\hat{F}_a(\hat{v}_{fas}) = 1.5 - 0.5 \frac{1 - \left(\frac{\hat{v}_{fas}}{\hat{v}_0}\right)}{1 + \left(\frac{7.56 \cdot \hat{v}_{fas}}{\hat{v}_0 \beta}\right)} \qquad \text{Eq 12}$$

Where β was the fiber type dependent curvature of the force-velocity relationship (Otten,

1987). Since the human RF is of a mixed fiber type (Johnson et al., 1973), β was

determined to be the average of the constants determined from literature of both slow and

fast fiber types (0.18 and 0.29, respectively; (Dick et al., 2017)). Similarly, $\hat{v}_0$, the

maximum intrinsic speed of the fascicles, was estimated as the average (7.5 s^{-1}) of values

from slow and fast fibers (5 and 10 s^{-1}, respectively (Lee et al., 2013; Wakeling et al.,

2012)).

Since EMG and ultrasound images were collected from different legs, for all

fascicle or MTU force, power, and work calculations information from both legs was

combined. This was achieved by ensemble averaging activations, fascicle

length/velocities, and MTU lengths/velocities, and fascicle pennation angles across all

iterations of a given perturbation timing and side within each participant. Thus, within-

participant and within-condition ensemble averaged timeseries were calculated for each

stride (*e.g.*, one trace for all RF activations ipsilateral to the perturbed leg for participant

1 during early stance perturbations). Using these combined traces, fascicle power was

calculated as the product of fascicle force and fascicle velocity, and MTU power was

calculated as the product of MTU force and MTU velocity, where fascicle or MTU

lengthening resulted in negative power, respectively. See Figure 12C for an overview of

fascicle and MTU force and power calculations. Based on previous work (Bobbert et al.,

1986; Jacobs et al., 1996), to calculate the mechanical power transferred by the RF MTU

from the hip to the knee joint, MTU force was multiplied by the hip flexion moment arm

between the hip joint center and the MTU, then by the hip angular velocity (with positive

defined as hip extension). Fascicle and MTU work values were calculated by integrating

the ensemble averaged curves (trapz, Matlab) and then multiplying by the average stride

duration of the traces divided by the number of normalized time points of each stride

(101). To compare leg or joint level mechanical work values with fascicle and MTU

mechanical work, mechanical works at the leg or joint levels were also averaged across

all perturbation iterations within each participant.
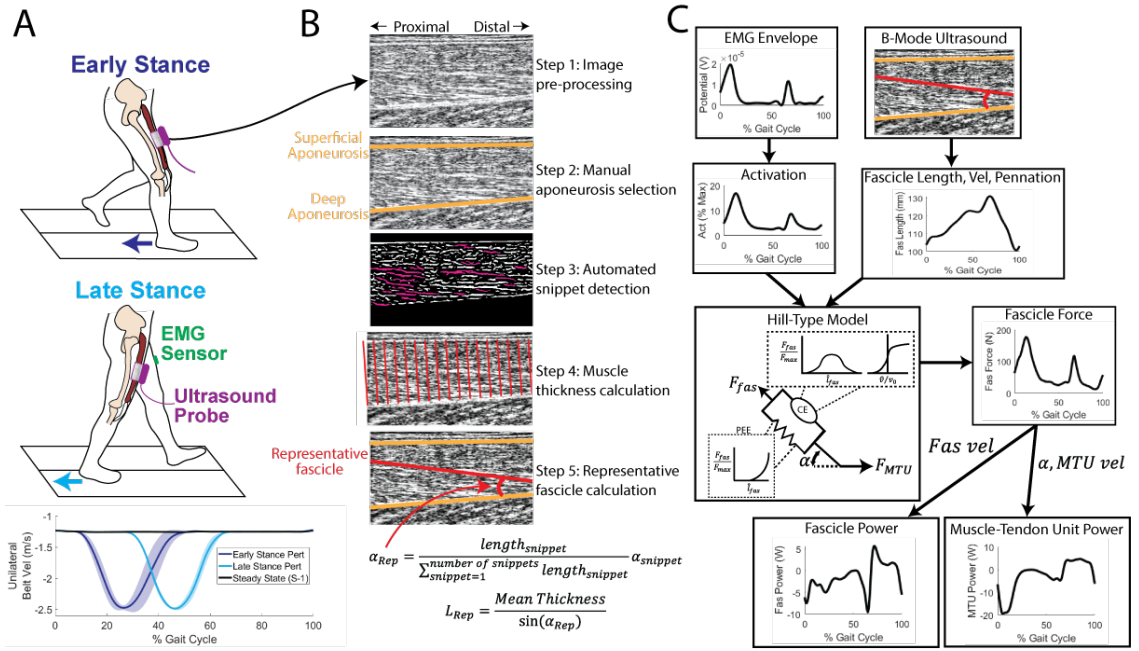
Figure 12 – A) Conceptual overview of the treadmill perturbation. B) Overview of custom fascicle tracker application. α = fascicle pennation angle, L_Rep = representative fascicle length. C) Overview of fascicle and muscle-tendon unit energetics computation. CE = contractile element, PEE = passive elastic element.

4.3.7   Statistical Analysis

Statistical analyses were performed in Matlab R2019b (Mathworks, Natick, MA, USA). To investigate differences in timeseries outcomes (e.g., fascicle lengths, activations, mechanical powers for H1), statistical parametric mapping (SPM; (Pataky et al., 2015)) was used to run paired t-tests to compare early or late stance traces to steady state traces (*i.e.*, the pre-perturbation stride) without needing to correct for multiple comparisons. While all statistical differences were reported, altering stride times from the perturbations led to phase shifts in the gait-cycle normalized data that resulted in some periods of statistical significance which were not determined to be meaningful. Further, p-values greater than the significance threshold (*i.e.*, 0.05) were approximated as the p-value associated with the maximum t-statistic during the entire timeseries. This approach has not

yet been validated (Statistical Parametric Mapping, 2007) and in some cases resulted in values less than the significance threshold. Such cases are denoted with *ns*. All timeseries data were represented in relation to the gait cycle of the perturbed (i.e., ipsilateral) leg. For discrete outcome measures such as mechanical work, paired t-tests were used to compare early or late stance perturbation conditions to steady state levels (H2 and H3). To evaluate the functional role of the RF in relation to the hip, knee, and overall leg (H2), linear regressions were used to relate changes in fascicle or MTU work to changes in hip, knee, and overall leg work relative to steady state levels (i.e., the work of the perturbed stride – work of the previous unperturbed stride, S-1). Since the hip had 3 degrees of freedom in these analyses, hip work was calculated as the integrated sum of all 3 components to better account for overall leg work. Analyses were limited to the unperturbed (S-1), perturbed (S0), and first recovery strides (S+1) as a return to steady state in external kinetics and kinematics was largely achieved after the first recovery stride (Golyski and Sawicki, 2022). Because data were collapsed across perturbation iteration, for each leg these regressions contained 14 points (7 participants x 2 timings) instead of 222 from all perturbations. Significance was concluded for p-values ≤ 0.05.

4.4   Results

4.4.1   H1 – The rectus femoris of the perturbed leg actively lengthens as a result of the perturbation

For both early and late stance perturbations, during the perturbed stride (S0) on the ipsilateral leg there was a lengthening of both the RF fascicles (early: p=0.001; late: p=0.059) and the MTU (early: p<0.001; late: p=0.039), though the lengthening of fascicles

for late stance perturbations did not achieve statistical significance. Further, though not statistically significant, an increase in RF activation from steady state levels was also observed (early: p=0.080; late: p=0.035, *ns*). Together, these longer fascicle lengths and increased activations resulted in increased fascicle forces during mid to late stance for early stance perturbations and around toe-off for late stance perturbations (p<0.001 for both; Figure 13). As hypothesized, this increased force coupled with lengthening resulted in larger negative powers at both the level of RF fascicles and the MTU (Figure 14). At the level of fascicles, these changes in power were statistically significant for early, but not late stance timings (early: p<0.001, late: p=0.050, *ns*). At the level of the MTU, changes in power were significant for both timings (p<0.001). These larger negative fascicle and MTU powers resulted in more negative work being performed by the fascicles (early: p<0.001; late: p=0.006) and MTU (early: p<0.001; late: p=0.002) on the perturbed stride relative to steady state.

4.4.2 Rectus femoris mechanical energetics on the contralateral leg and first recovery stride

On the contralateral leg to the perturbation, during the perturbed stride (S0), early stance perturbations were associated with first lengthening of both the fascicles and MTU, followed by shortening (p<0.001) to allow lengths to return to steady state levels around contralateral heelstrike. This shortening coincided with increased RF activation (p=0.025, *ns*) to result in increased forces (p<0.001) and larger positive fascicle and MTU powers (p<0.001; Figure 13). However, for fascicles, these larger positive powers were offset by larger negative powers later in the gait cycle, which resulted in the fascicles performing a larger amount of negative work over the perturbed stride relative to steady state (p=0.008;

Figure 14). Conversely, for the MTU, the larger negative power during the perturbation was not fully offset and the net work performed by the MTU was greater than steady state levels (p=0.047; Figure 14). For late stance perturbations, changes from steady state were predominantly limited to increased activations (p<0.001) and forces (p<0.001) coinciding with steady-state levels of fascicle and MTU lengthening to result in larger negative powers that manifested as negative fascicle (p=0.050) and MTU works (p=0.001) relative to steady state.

Across both legs, the largest deviations from steady state on the first recovery stride (S+1) occurred following late stance perturbations on the contralateral side. The contralateral RF fascicles lengthened then shortened during swing (p<0.001), despite shorter contralateral MTU lengths (p<0.001). With increased activations and higher forces (p<0.001), this resulted in a period of negative followed by positive fascicle power, which on net over the first recovery stride led to slightly more negative work being performed by the fascicles relative to steady state (p=0.050; Figure 13). In general, changes in both ipsilateral and contralateral fascicle and MTU work from steady state levels were minimal during the first recovery stride, despite achieving significance for the ipsilateral MTU (p=0.012), and the contralateral fascicles (p=0.009) and MTU (p=0.002) for early stance perturbations (Figure 14).
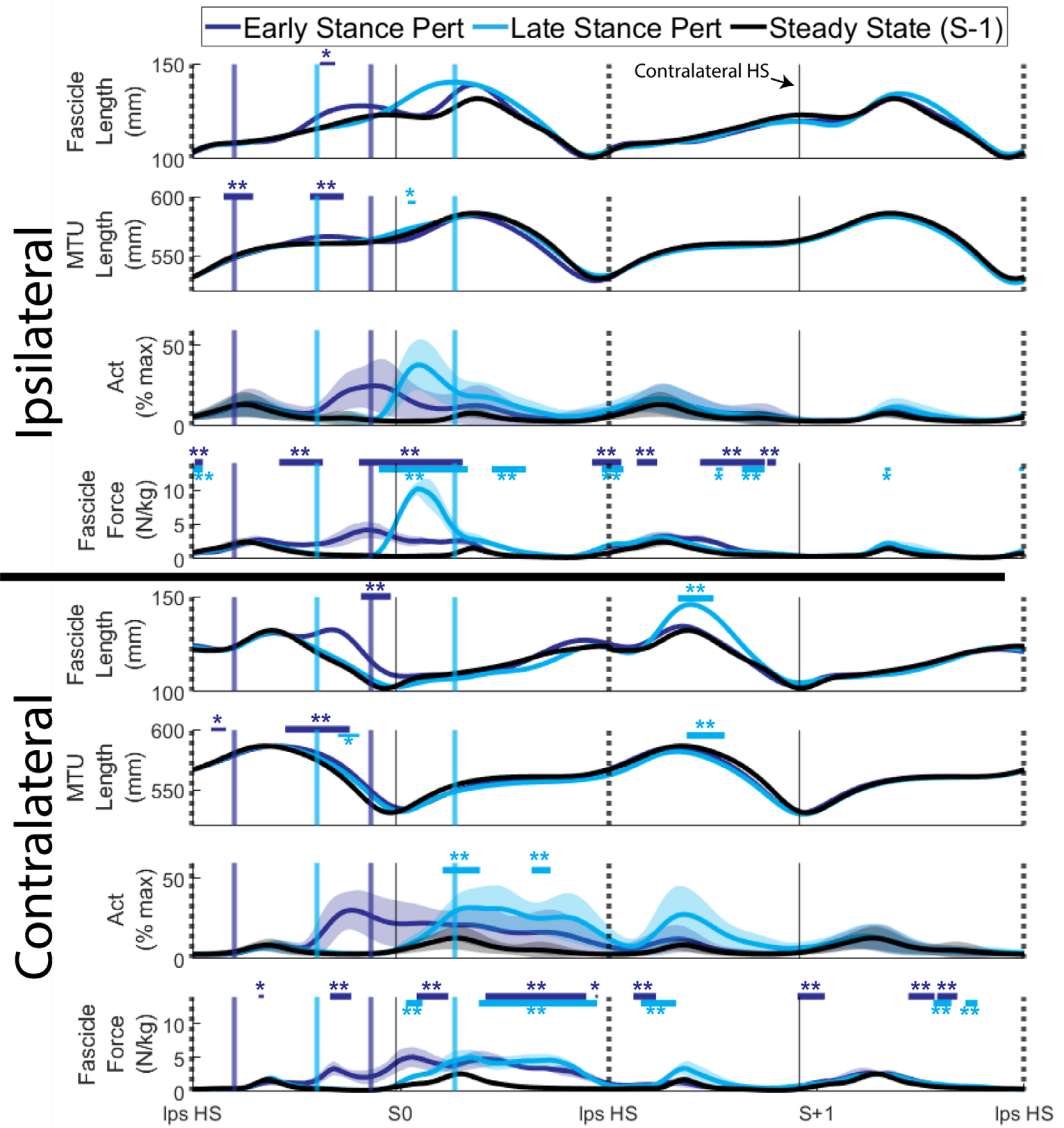
Figure 13 – Fascicle and MTU lengths, activations (% max across all trials), and forces for the rectus femoris on both sides relative to the perturbation, time-normalized to gait cycles. Shaded regions represent ±1 standard deviation. Standard deviations were omitted for length variables for clarity. Instances when curves significantly deviated from steady state (S-1) are identified with thick horizontal lines and ** for p < 0.001, and thin horizontal lines and * for p < 0.05. Solid colored vertical lines indicate average start and end times of the perturbations. Dotted/solid black vertical lines indicate instances of ipsilateral/contralateral heelstrike, respectively. "Steady State" strides were the strides preceding the perturbed stride (S-1).
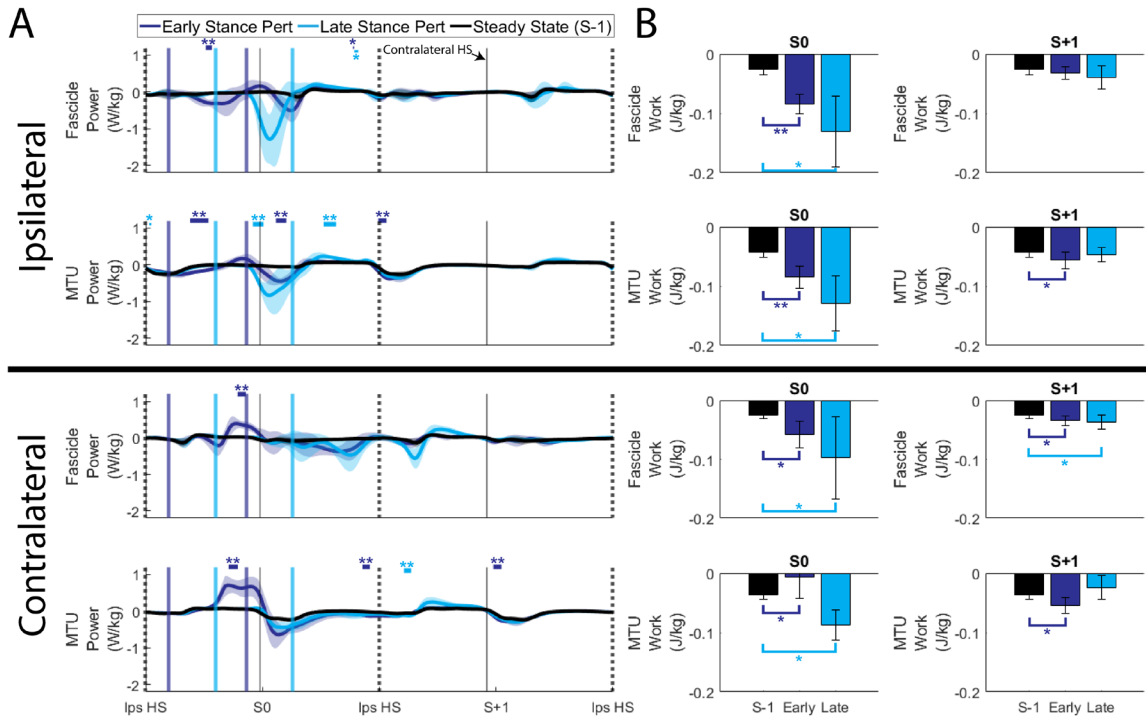
Figure 14 - A) Rectus femoris fascicle and MTU mechanical powers on both sides relative to the perturbation, time-normalized to gait cycles. Shaded regions represent ±1 standard deviation. Instances when curves significantly deviated from steady state (S-1) are identified with thick horizontal lines and ** for p < 0.001, and thin horizontal lines and * for p < 0.05. Solid colored vertical lines indicate average start and end times of the perturbations. Dotted/solid black vertical lines indicate instances of ipsilateral/contralateral heelstrike, respectively. "Steady State" strides were the strides preceding the perturbed stride (S-1). B) Rectus femoris fascicle and MTU work over the perturbed (S0) and first recovery stride (S+1) on both sides relative to the perturbation. Within-participant paired t-test results comparing perturbed to steady-state (S-1) values are represented as ** for p<0.001 and * for p<0.05.

4.4.3   H2 – The rectus femoris fascicles and MTU reflect the role of the knee and overall leg on the contralateral leg

Changes in RF fascicle and MTU work were more strongly related to changes in knee, hip, and overall leg work on the contralateral than the ipsilateral leg to the perturbation. Further, the MTU more strongly reflected demands at knee, hip, and leg levels than fascicles, though the direction of the relationships were generally consistent across fascicle and MTU levels for a given leg and stride (Figure 15).

On the perturbed stride (S0), contrary to our hypothesis, the RF fascicles/MTU had the strongest positive relationship with the hip (fascicle R^2=0.23, p=0.047; MTU R^2=0.64, p<0.001), and weaker negative relationships with the knee (fascicle R^2=0.11, p=0.1334; MTU R^2=0.47, p=0.004). Relationships between the RF fascicle/MTU levels were also weak and negative relative to the overall leg (fascicle R^2=0.10, p=0.145; MTU R^2=0.18, p=0.076).

On the first recovery stride (S+1), there was also a strong positive relationship between RF MTU and the hip (R^2=0.67, p<0.001), but not the fascicles (R^2=-0.02, p=0.399), which drove a similar relationship between the MTU and the overall leg (R^2=0.38, p=0.012).
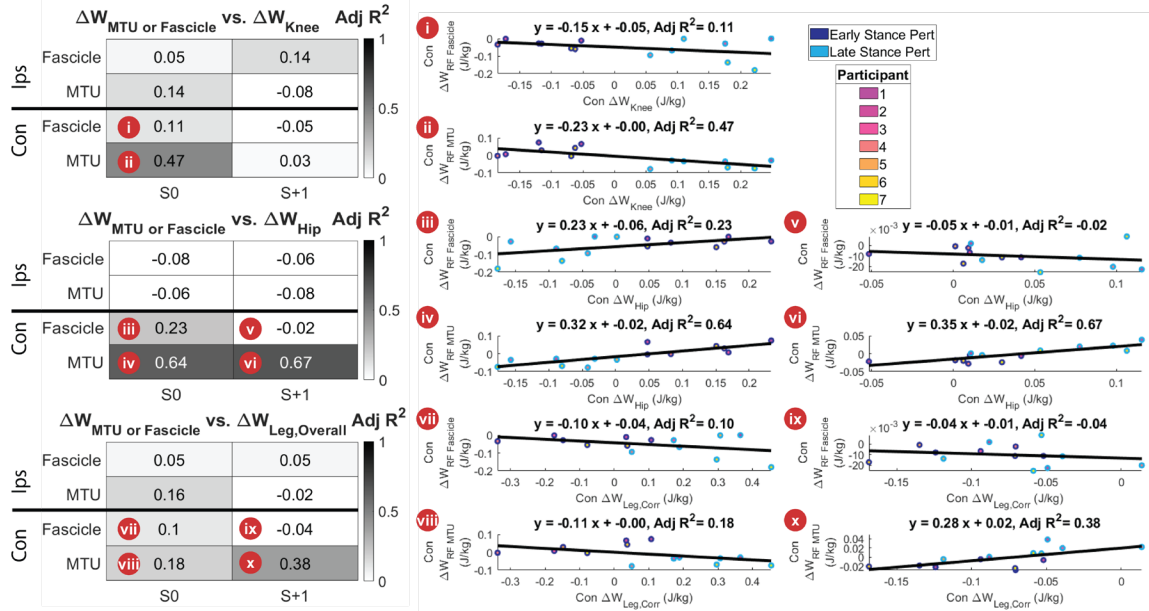
Figure 15 – Relationships between rectus femoris fascicle or MTU work and the knee, hip, and overall leg. Heatmaps show adjusted R^2 values for linear regressions between differences in fascicle or MTU work over a stride from steady state, and differences in knee, hip, or corrected leg work over a stride from steady state (S-1). Note that fascicle and MTU data were collapsed across iterations and sides, resulting in 14 data points per scatter from the original 222 perturbations. (i-x) Scatter plots for selected fascicle and MTU relationships of interest.

4.4.4 H3 – The rectus femoris MTU transfers net energy from the hip to the knee

On the perturbed leg, the RF exhibited differences in behavior between early and late stance perturbations (Figure 16). For early stance perturbations, on the perturbed stride (S0) the RF first transferred work from the hip to the knee during the perturbation ($p<0.001$), then from the knee to the hip around toe-off ($p<0.001$). Overall, this resulted in an increased net transfer of mechanical work from the hip to the knee during the perturbed stride relative to steady state, supporting our hypothesis ($p=0.015$). On the first recovery stride (S+1), increased RF transfer power from the hip to the knee during midstance ($p<0.001$) also resulted in increased net hip to knee work ($p<0.001$). For late stance perturbations, on the perturbed stride (S0) the RF predominantly transferred energy from

the knee to the hip into early swing (p<0.001). This resulted in net transfer work from the knee to the hip on the perturbed stride, contrary to our hypothesis (p<0.001).

On the contralateral leg, the RF generally behaved similarly between both perturbation timings and supported our hypothesis of a net hip to knee transfer of work. For both timings, there was increased RF transfer power from the knee to the hip during the perturbation (p<0.001), followed by a hip to knee transfer during swing (p<0.001). On net, this resulted in increased net transfers of energy from the hip to the knee for both timings relative to steady state levels (p<0.001). On the first recovery stride, for early stance perturbations, there was less energy transferred from the knee to the hip at toe-off (p<0.001), which was responsible for a slight increase in net hip to knee transfer work on the first recovery stride (p=0.001). Conversely, for late stance perturbations, there was increased knee to hip transfer power during toe-off (although not significant, p=0.056), which resulted in net knee to hip transfer work on the first recovery stride (p=0.035).
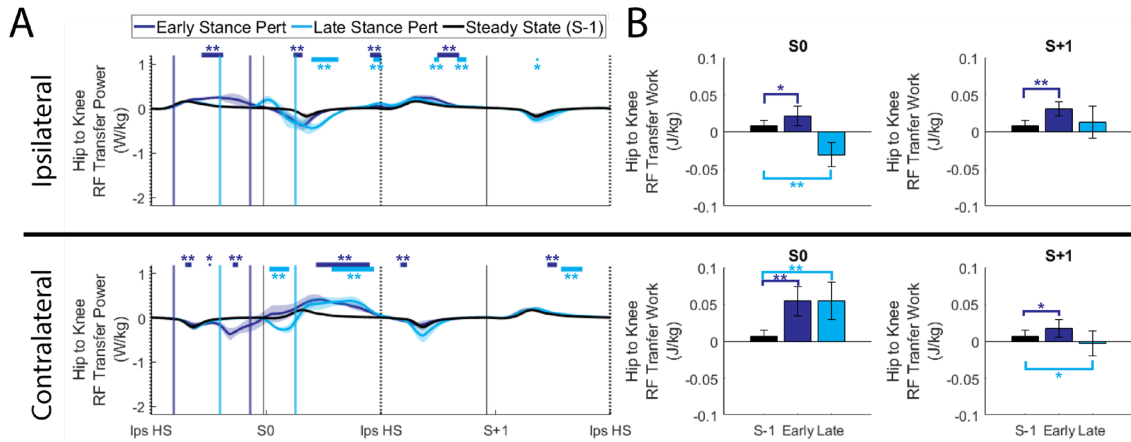
Figure 16 - A) Mechanical power transferred from the hip to the knee by the rectus femoris MTU on both sides relative to the perturbation, time-normalized to gait cycles. Shaded regions represent ±1 standard deviation. Instances when curves significantly deviated from steady state (S-1) are identified with thick horizontal lines and ** for p < 0.001, and thin horizontal lines and * for p < 0.05. Solid colored vertical lines indicate average start and end times of the perturbations. Dotted/solid black vertical lines indicate instances of ipsilateral/contralateral heelstrike, respectively. "Steady State" strides were the strides preceding the perturbed stride (S-1). B) Mechanical work transferred by the rectus femoris MTU from the hip to the knee over the perturbed (S0) and first recovery stride (S+1) on both sides relative to the perturbation. Within-participant paired t-test results comparing perturbed to steady-state (S-1) values are represented as ** for p<0.001 and * for p<0.05.

4.5   Discussion

The main objective of this work was to evaluate the role of the RF in mediating transient mechanical energy demands during perturbed walking in humans. Using unilateral belt accelerations on a split-belt treadmill, we imposed quantifiable mechanical energy demands on both legs during walking and extended our previous analysis relating joint and leg level demands down to the level of the RF MTU and fascicles (see (Golyski and Sawicki, 2022)). To estimate mechanical power and work of the RF for this approach, we used *in-vivo* RF fascicle lengths measured using B-mode ultrasound and a custom fascicle tracking application in conjunction with EMG to drive a Hill-type model of force

generation. Our first hypothesis (H1) sought to address the energetic implications of the perturbation itself – specifically, we hypothesized that on the perturbed leg, the perturbation would result in negative RF power and work because of active muscle lengthening. Our data supported this hypothesis, with lengthening occurring at both the levels of the fascicle and MTU coinciding with increased RF activation to precipitate negative power and work. While this represents the first *in-vivo* estimate of rectus femoris mechanical energetics during perturbed walking, the dissipation induced by the perturbation at proximal MTU and fascicle levels is mechanically analogous to other transient, dissipation-inducing perturbations delivered at distal sites. Specifically, unexpected changes in substrate height have been extensively investigated in both hopping humans and running guinea fowl (Daley and Biewener, 2011; Daley et al., 2009; Dick et al., 2021), with drops in ground height resulting in active lengthening of the plantarflexors. In perturbed human hopping, a drop in terrain height has been shown to extend the aerial phase and thus shift the onset timing of plantarflexor activation to be earlier relative to ground contact. This earlier activation in concert with coactivation of the tibialis anterior has been demonstrated to: 1) allow plantarflexor muscles to pre-emptively shorten before ground contact, allowing for lower, potentially less damaging muscle strains, 2) stiffen and stabilize the ankle, and 3) bias the muscle towards achieving the task demand (*i.e.*, dissipation of injected energy) due to alignment of activation and fascicle lengthening (Dick et al., 2021; Sawicki et al., 2015). We now address the consistency of those previous findings with our results. In our perturbation context, instead of delaying the onset of ground contact, we applied both perturbation timings within stance phase, which did not allow for a pre-emptive shortening during an unloaded period. Instead, we only observed

fascicle lengthening as a result of the perturbation. However, we did not observe fascicle strains that were damaging – normalized to fascicle slack length, the peak strain on the perturbed stride observed was 15%, below potentially injurious strains of 25% (Lieber and Friden, 1993). This may be attributable to series elasticity buffering changes in length between the MTU and fascicle levels, as has been observed in other knee extensors (Bohm et al., 2018), but not to the extent fascicle-level changes do not reflect joint-level dynamics, potentially due to higher stiffness of proximal vs. distal tendons (Arampatzis et al., 2006). Consistent with previous work investigating changes in activation of leg musculature during walking on uneven terrain (Voloshina et al., 2013), we observed coactivation of muscles across the lower limb on the perturbed leg (Figure 17), with increases in plantarflexor activation occurring first and being the most prominent. However, a previous study specifically investigating unilateral treadmill belt accelerations did not see increases in tibialis anterior activity following plantarflexor activation, which could be attributed to the less intense perturbations not eliciting a whole leg coactivation strategy (Sloot et al., 2015). Lastly, on the perturbed leg, we previously found the overall leg level demand of early stance perturbations was generation of net work over a stride, and the demand of late stance perturbations was net zero work over a stride, since net positive work performed by the leg on the treadmill is offset by net negative work performed by the leg on the COM (Golyski and Sawicki, 2022). Therefore, in contrast to tasks where plantarflexors have been shown to modulate their mechanical role to match that of the limb (Daley and Biewener, 2011; Daley et al., 2009; Dick et al., 2021), during a treadmill acceleration task the RF on the perturbed leg predominantly serves to dissipate energy and thus does not directly represent the energetic role of the leg, knee, or hip (Figure 15).

Despite the RF not reflecting the role of joints or the leg on the perturbed side, since we previously identified the contralateral knee as reflecting the energetic demand on the contralateral leg, we hypothesized due to the similar "damping" functions of the knee and RF (H2) that the contralateral RF may reflect knee, and therefore leg level demands on the perturbed stride. In contrast to our hypothesis, the RF, particularly at the MTU vs. fascicle level, best reflected the role of the contralateral hip, while the relationship between the RF and the knee and leg were weaker and negative (Figure 15). This relationship was due to 1) early stance perturbations eliciting positive net work at the hip joint and the MTU and fascicles actively shortening during swing to produce net positive power and 2) late stance perturbations eliciting negative work at the hip joint and the MTU and fascicles actively lengthening during stance to produce net negative power. In contrast, the work demands on the knee are opposite to that of the hip during these perturbation timings (*i.e.*, net negative knee work during early stance perturbations, net positive knee work during late stance perturbations). These findings indicate that while the role of the RF during unperturbed walking is generally dissipation of mechanical energy (Lai et al., 2019), and during perturbed walking this role can be amplified during stance phase, the RF can also contribute to energy generation through active shortening prior to ground contact.

Our third hypothesis (H3) was that the RF would facilitate the transfer of work from the hip to the knee joint. We found that on the perturbed leg and stride, the direction of net hip to knee transfer reversed for early vs. late stance perturbations. This was due to early stance perturbations eliciting increased hip to knee transfer power around midstance, in support of our hypothesis, while both timings elicited increased knee to hip transfer power driven by hip flexion at toe-off, contrary to our hypothesis. These energy transfers are

evidence of coordinated responses across biarticular muscles of the lower leg to accomplish whole-leg demands (Bobbert et al., 1986; Jacobs et al., 1996; Prilutsky and Zatsiorsky, 1994): for early stance perturbations, RF activation coupled with hip extension transfers energy from the hip to the knee, while gastrocnemius activation (Figure 17) coupled with knee extension at midstance transfers energy from the knee to the ankle, with the increased ankle power reflecting the overall leg-level demand of generation. For late stance perturbations, at toe-off, increased gastrocnemius activation coupled with knee flexion transfers energy from the ankle to the knee, which coupled with increased RF activation and hip flexion transfers energy from the knee to the hip. This proximal transfer of energy, coupled with the negative work of the RF MTU and fascicles, may partially explain how the net positive work performed between the leg on the treadmill belt is converted to the net negative work performed by the leg on the COM.

When interpreting our findings, two important technical limitations should be considered. The first limitation is that RF fascicle lengths measured using the custom tracking application were not validated against gold-standard measurement tools such as diffusion tensor imaging or extended field of view techniques (Bolsterlee et al., 2015; Noorkoiv et al., 2010). Further, comparison against hand-tracked ultrasound images may not serve as a high-fidelity standard because 2D ultrasound images cannot capture the complex 3D shape changes of the muscle (Blemker and Delp, 2006), high frame rate ultrasound imaging still necessitates the extrapolation of fascicle lengths from the imaged section of the muscle, and manual tracking of a single fascicle would likely have more variability than tracking all fascicles within the imaged section of the RF. We are confident in our tracking application because 1) the selection of snippets used to calculate a

representative fascicle was similar to that of a previously validated application (Marzilger et al., 2018), 2) only snippets within a physiological range of pennation angles were used to estimate a representative fascicle, 3) the thickness of the muscle was calculated from hand-tracked aponeuroses for each frame, 4) for within-subject designs, our extrapolation method has been shown to be acceptable for estimating normalized fascicle lengths of other quadriceps muscles (Brennan et al., 2017). Further, the range of RF fascicle strains we observed during unperturbed walking (0.85 to 1.08 of fascicle slack length) is more physiologically plausible than the range reported from simulated RF fiber length during walking at 1.25 m/s (0.7 to 1.4 of optimal fiber length; (Arnold et al., 2013)), particularly when considering active strains above 25% being potentially damaging (Lieber and Friden, 1993). The second important limitation is that we estimated fascicle and MTU forces using a Hill-type model, which is known to have shortcomings when predicting *in-vivo* forces and energetics (Dick et al., 2017; Lee et al., 2013; Perreault et al., 2003; Sandercock and Heckman, 1997; Umberger et al., 2003; Wakeling et al., 2012). Multiple aspects of Hill-type models have been suggested to contribute to these discrepancies, a subset of which are: 1) that Hill-type models are based on phenomenological relationships characterized at maximal activations, which may explain inaccuracies when estimating forces at physiological, submaximal levels (Dick et al., 2017; Lee et al., 2013; Perreault et al., 2003), 2) classical Hill-type models have independent length, velocity, and activation components and thus do not capture physiological relationships between length and activation (Close, 1972; Holt and Azizi, 2014; Huijing, 1998) or velocity and activation (Brown et al., 1999), and 3) Hill-type models do not capture the history dependence of muscle force, which may play an important role in responses to perturbations (de Groote et al., 2017; Lee and

Herzog, 2003; Libby et al., 2020). Despite these shortcomings, the computational tractability of Hill-type models has resulted in them becoming the state of the art for use in simulations of human movement (Arnold and Delp, 2011; Arnold et al., 2013; Hamner et al., 2010). By using *in-vivo* estimates of fascicle length and activation to drive a Hill-type model, our approach represents a potential improvement over other fully computational approaches by avoiding assumptions about force sharing among quadriceps muscles and the influence of series elasticity from aponeuroses and the external tendon, both of which are particularly relevant for the RF (Ackland et al., 2012; Pizzolato et al., 2015).

To conclude, this study extended a previous investigation of the relationship between joint and leg level mechanical energetics during perturbed walking down to the level of the RF MTU and fascicles. This was accomplished by coupling in-vivo EMG and B-mode ultrasound imaging in conjunction with a Hill-type model of muscle force. We found that 1) on the perturbed leg the RF MTU and fascicles actively lengthened during the perturbation, indicating a muscle-level representation of the perturbed external kinematics, 2) on the contralateral side the RF, particularly at the MTU level, better reflected energetic demands on the hip as opposed to the knee and leg levels, and 3) on the perturbed leg the RF acted to shuttle energy across the leg to fulfill the overall leg-level demand. We anticipate future work will use such multi-scale approaches to better understand how changes in muscle-level dynamics explain altered joint and leg level demands during use of assistive devices (Nuckols et al., 2020a), and following injury (Willson et al., 2022). Further, muscle-level measurements coupled with models of physiological sensory organs can provide a window into the signals and motor programs

used by the nervous system to maintain stability during locomotion (Blum et al., 2017; Lin and Crago, 2002a; Lin and Crago, 2002b).

4.6   Ethics

All participants provided written informed consent and all protocols were approved by the Institutional Review Board at the Georgia Institute of Technology (Protocol H20163).

4.7   Data Accessibility

The ultrasound processing script and biomechanical data for all participants (N=7) will be available at: https://sites.gatech.edu/hpl/archival-data-from-publications/

4.8   Authors' Contributions

Pawel R. Golyski and Gregory S. Sawicki conceived of the study and designed the experimental protocol; Pawel R. Golyski carried out the experiments, analyzed the data, and drafted the manuscript; Pawel R. Golyski and Gregory S. Sawicki edited the manuscript. Both authors gave final approval for publication.

4.9   Competing Interests

We declare no competing interests.

4.10   Funding

4.11 Acknowledgements
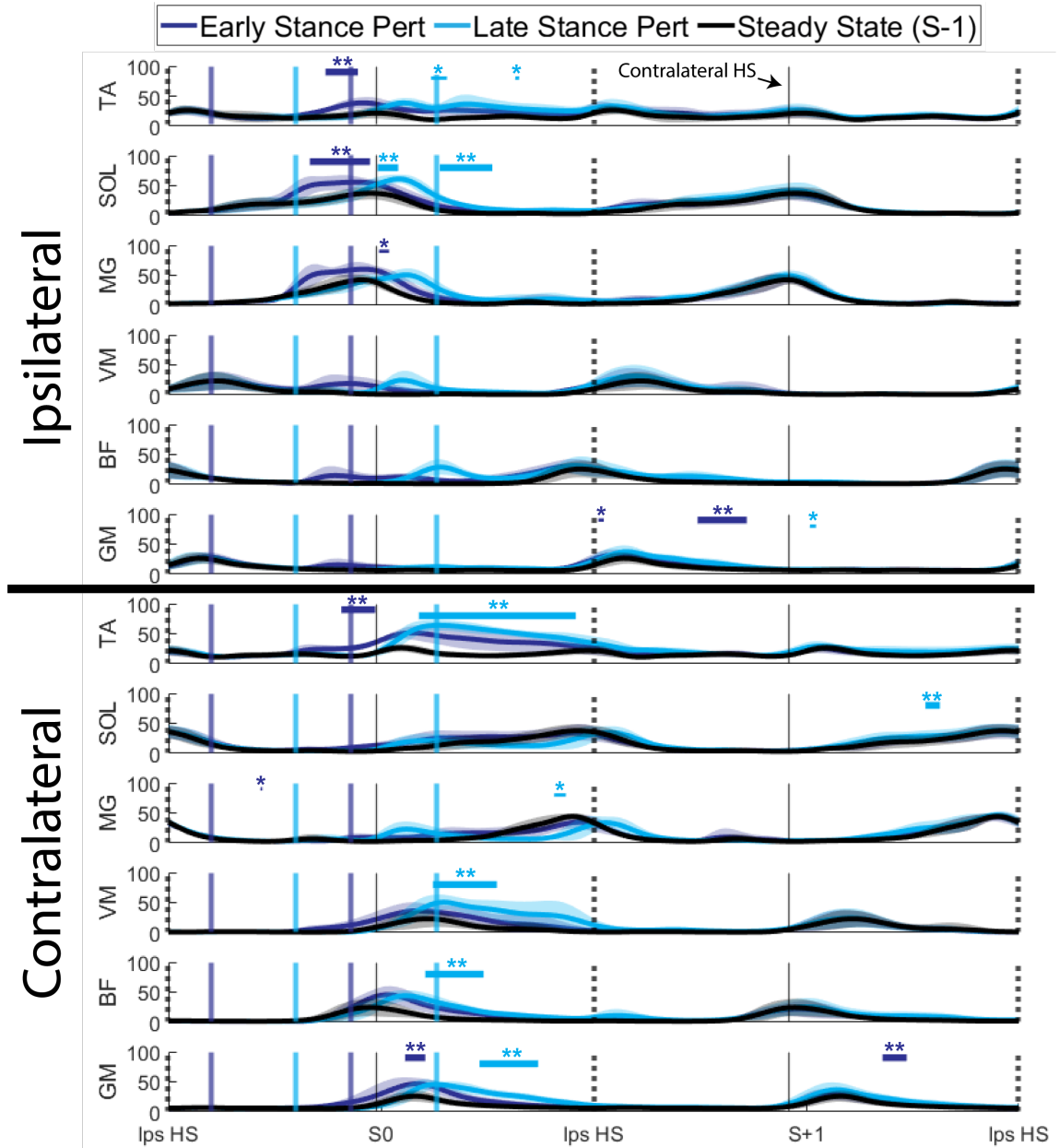
Figure 17 – Muscle activations (% max across all trials) on both sides relative to the perturbation, time-normalized to gait cycles. TA = tibialis anterior, SOL = soleus, MG = medial gastrocnemius, VM = vastus medialis, BF =biceps femoris, GM = gluteus maximus. Shaded regions represent ±1 standard deviation. Instances when curves significantly deviated from steady state (S-1) are identified with thick horizontal lines and ** for p < 0.001, and thin horizontal lines and * for p < 0.05. Solid colored vertical lines indicate average start and end times of the perturbations. Dotted/solid black vertical lines indicate instances of ipsilateral/contralateral heelstrike, respectively. "Steady State" strides were the strides preceding the perturbed stride (S-1).
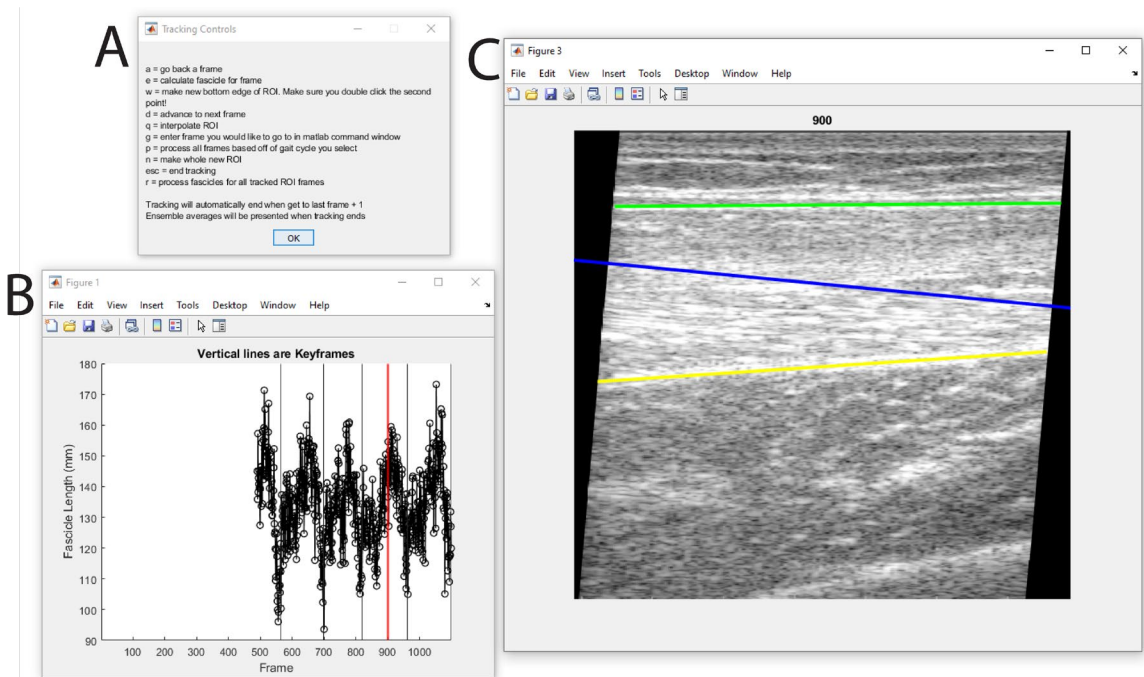
Figure 18-Custom fascicle tracking application user interface. A) Instructional information for operating the tracker. B) Representative fascicle length window. The vertical red line indicates the current image frame. Vertical thin black lines indicate keyframes (*e.g.* ipsilateral heelstrikes). C) Image window. The green line indicates the top aponeurosis, the yellow line indicates the bottom aponeurosis, and the blue line is a graphical presentation of a representative fascicle located at the middle of the images.

CHAPTER 5.   EFFECTS OF A PASSIVE HIP EXOSKELETON ON STABILITY AND PERTURBATION ENERGETICS

The fourth and final work associated with my dissertation investigates how an elastic hip exoskeleton influences stability and mechanical energetics during perturbed walking. This chapter constitutes a manuscript draft that I intend to submit to the Journal of Biomechanics as part of my American Society of Biomechanics Pre-Doctoral Achievement Award.

5.1   Abstract

Relative to powered devices, passive hip exoskeletons provide potentially cheaper and lower-profile approaches to assisting locomotion during walking. However, the effect of passive hip exoskeletons on stability during walking is not known, which is concerning since the populations that may benefit from their ability to lower metabolic cost of walking also contend with balance impairments. Here, we investigated the effects of a passive hip exoskeleton on stability as measured by whole-body angular momentum (WBAM) and mechanical energetics during perturbed walking. We hypothesized that during the perturbation, 1) a passive hip exoskeleton would improve stability as measured by a smaller range in sagittal WBAM and a lower whole-body energetic demand of the perturbation, and 2) this improvement in stability would be mediated by the exoskeleton shifting the local mechanical energetics of the joint and muscle it targets (the hip and rectus femoris, respectively) to oppose the energetic demands of the perturbation. Contrary to our hypotheses, we found that the passive hip exoskeleton had limited effects on the

mechanical energetics of whole body, legs, joints, and rectus femoris, while there was an increase in WBAM range during steady state with increasing exoskeleton stiffness. Our findings suggests 1) there is a discrepancy between stability effects of an exoskeleton as characterized by WBAM range and mechanical energetics, 2) the deleterious effects of sagittal WBAM range stem from the action of the passive hip exoskeleton on the trunk, rather than the legs, and 3) that future exoskeletons seeking to modulate transient mechanical energetic demands of perturbations should leverage active devices that can directly inject or extract energy, rather than modulating muscle-level energetics.

5.2   Introduction

Lower-limb exoskeletons have been designed for a wide variety of applications, including lowering the metabolic cost of locomotion (e.g., (Nasiri et al., 2018; Panizzolo et al., 2019; Sawicki et al., 2020; Seo et al., 2016; Shepertycky et al.; Witte et al., 2020)), reducing risk of injury (e.g., (Lamers and Zelik, 2021; Li et al., 2021)), facilitating rehabilitation (e.g., (Banala et al., 2008; Patton et al., 2008)), and improving stability (Hua et al., 2021; Monaco et al., 2017; Ringhof et al., 2019; Zhang et al., 2018). Passive devices actuated by elastic elements provide a tantalizing alternative to active, motor-driven devices since they can be cheaper, lighter, and do not require tuning of sophisticated hardware, while also being able to augment selected locomotor objectives, most often the improvement of walking and running economy (Collins et al., 2015; Nasiri et al., 2018; Panizzolo et al., 2019). However, the effect of passive exoskeletons on stability during locomotion is unknown. This is concerning since addressing fall risk is the most important feature of exoskeleton design according to stakeholders (Wolff et al., 2014), and populations that may benefit from such devices metabolically are also at a higher risk of

falls during walking, such as elderly adults (Hartholt et al., 2019; Moreland et al., 2020; Ortega and Farley, 2007).

From the perspective of mechanical energetics, passive exoskeletons may initially seem unlikely to improve stability following perturbations during walking – to achieve "energetic" stability during constant speed, level ground walking, over a stride any net mechanical energy injected into the body from the environment must be dissipated, and any net mechanical energy extracted by the environment from the body must be re-generated, such that the overall energy of the body returns to steady state levels (i.e., net zero work over a stride). Although passive exoskeletons cannot contribute net mechanical energy, they can redistribute energy and alter the mechanics of underlying musculature to modulate the biological work at the joints they target (Collins et al., 2015; Farris et al., 2013; Nuckols et al., 2020a; Nuckols et al., 2020b; van Dijk and van der Kooij, 2014). At the hip joint specifically, previous studies have shown that during walking passive exoskeletons can alter distal muscle activations (Haufe et al., 2020) and increase biological hip work (Lewis and Ferris, 2011). However, how such shifts relate to mediating the transient energetic demands of a perturbation remains unknown.

In this study, we have sought to address this gap by assessing the influence of a passive hip exoskeleton on stability and multi-scale mechanical energetics during treadmill walking with transient unilateral belt accelerations delivered in either early or late stance. To quantify stability during this task, sagittal plane whole-body angular momentum (WBAM) serves as a measure which captures the kinematic demand of the perturbation – during a belt acceleration or trip, the body is pitched forwards, which results in changes in translational and rotational velocities of the body segments relative to the center of mass

82

(COM) (Liu and Finley, 2020; Pijnappels et al., 2004). Further, WBAM is thought to assess stability since it fluctuates within a narrow range during unperturbed walking in healthy uninjured individuals (Herr and Popovic, 2008; Popovic et al., 2004), while this range is broader in populations with balance impairments such as stroke-survivors and individuals with lower-limb amputation (Honda et al., 2019; Nott et al., 2014; Silverman and Neptune, 2011; Vistamehr et al., 2016).

To quantify the multi-scale mechanical energetic changes induced by a passive hip exoskeleton, we leveraged previously established approaches to examining mechanical work demands of a unilateral belt acceleration at the leg, joint, and rectus femoris (RF) muscle-tendon unit (MTU) and fascicle levels through a combination of inverse kinematics and dynamics, *in-vivo* B-mode ultrasound and EMG measurements, and Hill-type models of muscle force ((Golyski and Sawicki, 2022), Chapter 4). Further, as part of this study the previous custom semiautomated fascicle tracker was augmented with a deep learning approach into a fully automated tracking application. To enable use of *in-vivo* measurements, a torso-mounted torsional passive hip exoskeleton (TPHE – "tee-fee") was designed to provide hip flexion assistance using a spring-loaded mechanism aligned with the hip joint in the sagittal plane, as opposed to an elastic element running parallel to the quadriceps as in previous designs (Chen et al., 2019; Haufe et al., 2020; Panizzolo et al., 2017; Panizzolo et al., 2019; Panizzolo et al., 2021). To facilitate user acceptance of the device, the torsional spring mechanism was designed to produce torque mimicking that of the biological torque-angle relationship, which resembles a "flexion spring" from mid to late stance (Shamaei et al., 2013).

To relate stability and mechanical energetics in the context of a passive hip exoskeleton, our two central hypotheses were that improved stability over the perturbed and first recovery strides, as evidenced by decreased ranges of sagittal WBAM, would be achieved when (H1) the exoskeleton shifted the net mechanical work of the whole body towards steady state levels (i.e., 0 net work over a stride), and when (H2) the exoskeleton shifted the net mechanical work of the hip joints, RF MTUs, and RF fascicles in opposition to the whole body demands of the perturbation (i.e., when the perturbation elicits net positive work at the whole-body level, a shift towards negative work at the muscle level would be stabilizing).

5.3   Methods

5.3.1   Exoskeleton Design and Characterization

The TPHE (Figure 19A) was composed of 3 sections: a torso interface, 2 thigh interfaces, and 2 torsional mechanisms (Figure 19B). The torso interface consisted of a commercially available thoracic lumbar sacral orthosis (Optec Edge SL TLSO, Optec USA Inc, GA) which was modified to allow for mounting of hardware using adjustable clamps to a spinal assembly similar to a previously published hip exoskeleton design (Chiu et al., 2021). Custom hinges to allow for ab/adduction of the hip joint were used to connect the spinal assembly to the torsional mechanisms. The mediolateral width of the pelvis assembly could accommodate standing hip widths up to 43 cm (99th percentile males and females; (Tilley and Henry Dreyfuss Associates, 2002)). Each thigh interface consisted of a custom carbon fiber strut which contacted the posterior aspect of the user's hamstring through a shear-reducing mechanism to accommodate for misalignment of the mechanism

with the biological hip joint axes. The carbon fiber strut lengths fit user statures from 171 to 196 cm, or 24th to 99th percentile males and 89th to 99th percentile females (Centers for Disease Control and Prevention (CDC) and National Center for Health Statistics (NCHS), 2016). The design objectives for the torsional mechanism were 1) to provide hip extension resistance/hip flexion assistance around midstance to mimic the torque-angle relation of the biological hip joint (Shamaei et al., 2013) and 2) to be able to safely produce a stiffness matching that of previously published hip flexion assisting exoskeletons. For the first objective, a mechanism was designed to couple a hard stop to a given hip angle, after which point further deflection would load a torsional spring. This was achieved by affixing the outer edge of the torsional spring relative to the pelvis, while the inner section of the spring was attached to a "stopper" (Figure 19B). This "stopper" would collide with a "striker" component that was coupled to the thigh at a set angle between -20 to 20 degrees of hip flexion in 10-degree increments using two steel pins. For the second objective, a survey of the literature indicated that approximate "flexion-spring" stiffnesses of other hip exoskeletons ranged from 0.17 to 1.5 Nm/degree (Chen et al., 2019; Haufe et al., 2020; Lenzi et al., 2013; Nasiri et al., 2018; Panizzolo et al., 2019; Young et al., 2017). Thus, we designed our mechanism to be able to accommodate a range of stiffnesses: 0.33, 0.66, 1 Nm/deg, in addition to a no-spring condition. The maximum stiffnesses in conjunction with the peak hip extension relative to midstance hip angle during transient belt accelerations (~30 degrees, (Golyski and Sawicki, 2022)) led us to design the mechanism to withstand 30 Nm torques. Custom torsional springs were machined from grade 5 titanium due to its high specific energy. The spiral profile of the spring was first calculated analytically with relations specified in literature (Knox and Schmiedeler, 2009) for the maximum stiffness

spring (K3) using the maximum desired spring constant (1 Nm/deg), maximum expected torque (30 Nm), and the maximum material thickness based on manufacturer availability (2.54 cm). After determining a candidate design, FEA (Solidworks, Dassault Systemes, Velizy-Villacoublay, FR) was used to iteratively determine spiral member thicknesses and fillet radii of the attachment of the springs to the outer and inner rings such that members would not contact each other or the outer ring of the torsional spring, which would lead to a non-linear stiffness profile. From this maximum stiffness design, the remaining spring designs were determined by decreasing the thickness of the spring, as torsional stiffness and spring thickness are related 1:1. Thus, the K1 spring had a modelled stiffness of 0.33 Nm/deg and was 0.84 cm thick, and the K2 spring has a modelled stiffness of 0.66 Nm/deg and was 1.68 cm thick, with all springs having an outer diameter of 10 cm. Aside from the springs, all mechanism components had safety factors during 30 Nm torques of 3 or greater. For the springs, the maximum torques were determined based on their peak kinematic deformations (i.e., 10 Nm peak torque for K1, 20 Nm peak torque for K2, and 30 Nm peak torque for K3). The safety factors for the K1, K2, and K3 springs were 1.7, 2.2, and 1.9, respectively. We anticipated users would reduce their hip extension with the device, so these factors of safety were considered conservative.

To both assess the actual stiffnesses of the manufactured springs and allow for estimation of torques during use of the device, the pelvis and thigh sections of the mechanism were fitted with 3D printed surfaces for attachment of retroreflective motion capture markers. These markers were used to define coordinate systems local to the thigh and pelvis segments and thus the relative angle between them. Each configuration of the mechanism (3 spring stiffnesses and 5 engagement angles) was placed in a custom

benchtop testing setup where the torque of the device was measured with a torsional load cell (FSH04063, Futek, Irvine, CA) while the mechanism was manually displaced until it reached its maximum torque (i.e., 10, 20, and 30 Nm for K1, K2, and K3, respectively). Each displacement was performed 3 times. For each configuration, the data was fit with a piecewise linear polynomial to estimate the stiffness and actual engagement angle (SLM, Matlab). During device use, these piecewise polynomial fits were used to estimate device torques as a function of mechanism configuration and the relative angles of the pelvis and thigh segments tracked using the same motion capture markers as for benchtop testing. Results of benchtop testing are included as a supplementary figure (Figure 27).

All machined components aside from the torsional springs were manufactured from 7075-T6 aluminum, due to its high specific strength. The TPHE had a worn mass of 5.5, 5.8, 6.1, and 6.4 kg in the K0 (no spring), K1, K2, and K3 configurations. Not including carbon fiber and manufacturing costs the TPHE cost $2,000. Bills of materials and CAD designs for the TPHE and benchtop testing setup will be made available at https://sites.gatech.edu/hpl/models/.

5.3.2 Experimental Protocol

11 healthy, uninjured individuals (10 males, 1 female, mean [SD]: 23 [3] years, 182.1 [6.6] cm stature, 77.2 [11.3] kg) participated in this study after providing informed consent to the protocol approved by the local Institutional Review Board.

Each participant first attended a training session where the TPHE in the K0 configuration was fitted, and the rotational axis of the mechanism was aligned with the sagittal hip joint axis during standing. The participants then walked for 20 minutes at 1.25

m/s with no perturbations. Mechanism angles were collected via optical motion capture (Vicon, Oxford, UK) at 100 Hz during the last 20 seconds of the trial to determine the engagement angle that would lead to torque starting in midstance, estimated as the midrange angle. For the remainder of the training session, both mechanisms were set at that engagement angle. Each participant then walked unperturbed for 20 minutes with each of the remaining conditions in order of increasing stiffness (i.e., 80 minutes total of walking), and returned 2-8 days later for the testing session. This timescale was selected based on previous work in passive ankle exoskeletons where 25 minutes per condition with 2-7 days between training and testing sessions was used to facilitate motor learning and retention in the context of metabolic effects (Nuckols et al., 2020a), since motor learning and retention timescales in the context of exoskeletons and stability is unknown.

During the testing session, each participant was instrumented with EMG sensors, retroreflective markers, and a B-mode ultrasound probe (details described in following sections) and was fitted with the TPHE in the K0 condition and walked unperturbed for 2 minutes at 1.25 m/s on an instrumented split-belt treadmill (CAREN, Motek, Netherlands). The last 20 seconds of walking were collected to re-determine the engagement angles that would lead to torque onset at midstance. Note that engagement angles for all participants for training and testing sessions were set to begin torque at 20 degrees of mechanism flexion, except for one participant where the mechanisms were set at 10 degrees flexion (participant 1). The mean (SD) engagement angle across all participants and sides was 18.3 (5.0) degrees of mechanism flexion. Following this angle check, each participant completed 4 blocks of testing, each in a different spring configuration (K0-K3), with the order of configurations being pseudo-randomized. Within each block, each participant first

walked unperturbed for 2 minutes at 1.25 m/s, then walked for approximately 15 minutes while experiencing transient, unilateral belt accelerations delivered in either early (onset at ~10% of the gait cycle) or late stance (onset at ~30% of the gait cycle). Within each block, participants experienced 20 perturbations (2 timing x left or right side x 5 repetitions). The perturbations were delivered using a custom DFlow application (Motek, Netherlands) which used real-time motion capture data to estimate gait phase. Details of the algorithm are described in (Golyski et al., 2021). 30-40 steps elapsed between perturbations to allow for a return to steady state walking (Liu et al., 2018). A conceptual overview of the experiment is shown in Figure 19C, in addition to perturbation velocity profiles.
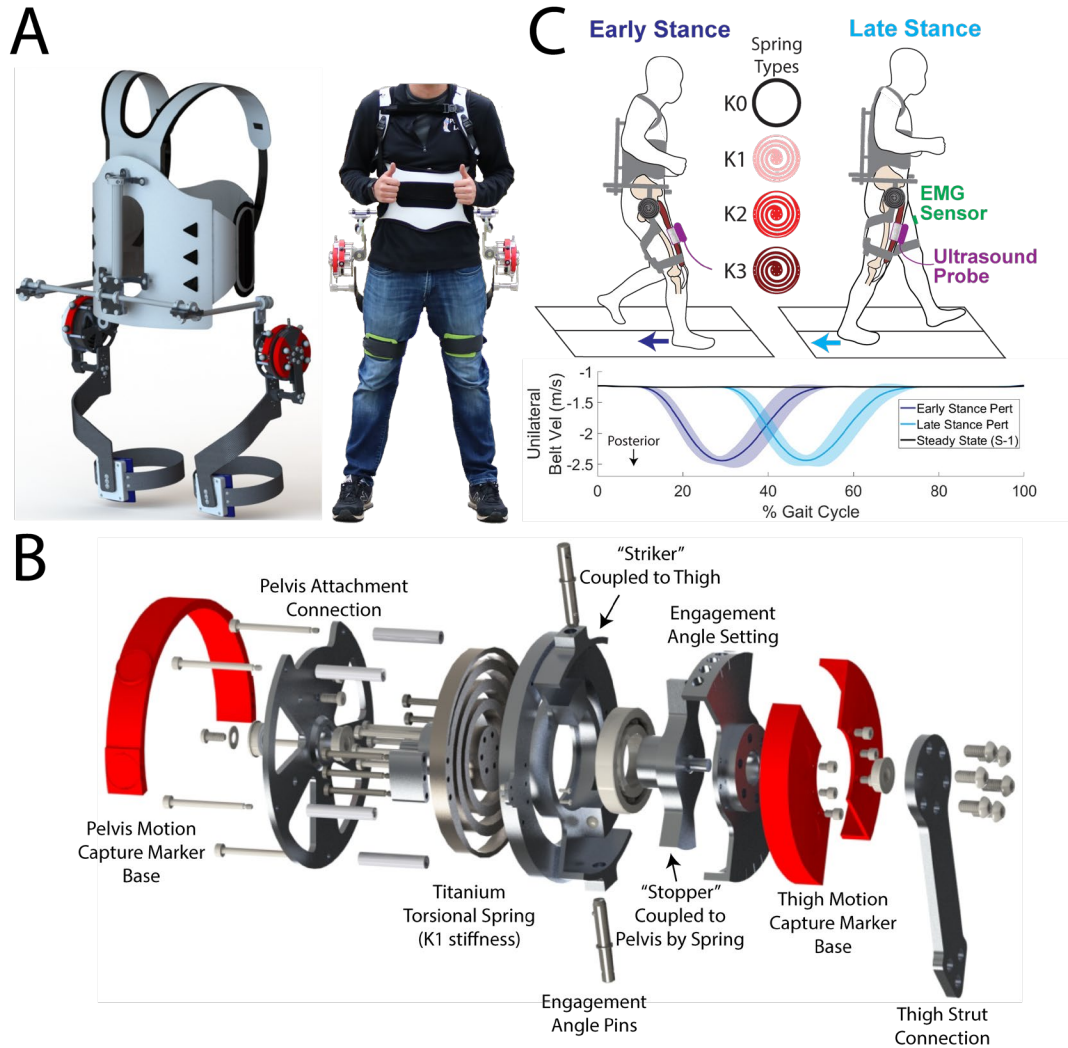
Figure 19 – (A) Torsional passive hip exoskeleton (TPHE) rendering (left) and reality (right). (B) Torsional mechanism rendering exploded view. (C) Conceptual overview of experimental protocol. Treadmill belt velocity profiles are across-participant ensemble averages, with shaded regions representing ±1 standard deviation.

5.3.3 External Kinematics and Kinetics

82 total retroreflective markers were affixed to each participant (modified human body model 2 (van den Bogert et al., 2013)) and the exoskeleton (16 markers used to track mechanisms), with 5 pelvis and trunk markers being attached to the exoskeleton and also used to track human body movement. 3D marker trajectories were collected at 100 Hz

(Vicon, Oxford, UK). A generic full-body musculoskeletal model ((Rajagopal et al., 2016), 22 rigid bodies, 37 degrees of freedom) was scaled in OpenSim (Delp et al., 2007) for each participant based on a static standing trial where the participant was in the K0 configuration. As opposed to previous work ((Golyski and Sawicki, 2022), Chapter 4), the subtalar joints were unlocked in the model, while the metatarsophalangeal joints remained locked, assuming the forefoot was a rigid body. Models for the various TPHE spring conditions were generated by attributing the added mass of the exoskeleton to the torso and scaling the inertia tensor of the torso segment accordingly. Joint angles were calculated using the OpenSim inverse kinematics tool, which calculated joint angles by solving a global least squares minimization problem between markers affixed to the scaled model and experimental marker positions. Joint moments were calculated using the OpenSim inverse dynamics tool with inputs of ground reaction force as measured by the instrumented treadmill (2000 Hz sampling) and joint angles. Joint angles and moments were low-pass filtered at 6 and 15 Hz, respectively, using fourth order zero-phase Butterworth filters. Across-participant ensemble averages of lower limb angles and moments are included as supplementary figures (Figure 28 and Figure 29, respectively). RF MTU lengths were calculated using the OpenSim Muscle Analysis tool based on the scaled models and joint angles. Positions and velocities of all body segments and the whole-body COM were calculating from kinematic data using the OpenSim Body Kinematics tool, as in (Golyski and Sawicki, 2022). Strides were segmented using a 30 Newton threshold applied to vertical ground reaction force. All trials were manually inspected for crossover steps, with 717 of the 880 perturbations being used for all subsequent analyses.

5.3.4 Whole-Body Angular Momentum

WBAM about the whole-body COM was calculated using a custom Matlab script with inputs of segment masses, inertias, positions, and linear and rotational velocities. Segment masses and inertias were obtained from scaled models while positions and velocities were calculated using the OpenSim Body Kinematics tool. These values were used to calculate WBAM according to Eq 13 (Herr and Popovic, 2008; Popovic et al., 2004):

$$\boldsymbol{WBAM} = \sum_{i=1}^{22}[(\boldsymbol{r}_{COM}^i - \boldsymbol{r}_{COM}) \times m^i(\boldsymbol{v}_{COM}^i - \boldsymbol{v}_{COM}) + \overleftrightarrow{\boldsymbol{I}}^i\boldsymbol{\omega}^i] \quad \text{Eq 13}$$

Where i indicates the segment number (22 total due to the musculoskeletal model), $\boldsymbol{r}_{COM}$ is the position of the whole-body center of mass, $\boldsymbol{r}_{COM}^i$ is the position of the segment's center of mass, m^i is the mass of the segment, $\boldsymbol{v}_{COM}^i$ is the velocity of the segment's center of mass, $\boldsymbol{v}_{COM}$ is the velocity of the whole-body center of mass, $\overleftrightarrow{\boldsymbol{I}}^i$ is the segment inertia tensor, and $\boldsymbol{\omega}^i$ is the segment angular velocity. WBAM was expressed in the fixed laboratory reference frame and was normalized using the mass of each participant not wearing the exoskeleton, the height of each participant, and the average walking speed (1.25 m/s).

5.3.5 Whole-Body, Leg, and Joint Energetics

Whole-body mechanical power was calculated as described in (Zelik et al., 2015), according to Eq 14:

$$P_{Whole\ Body} = P_{COM} + P_{per} \quad \text{Eq 14}$$

P_{COM} was the mechanical power of the COM relative to the global frame calculated according to Eq 15, and P_{per} was the mechanical power of the 22 body segments moving relative to the COM according to Eq 16:

$$P_{COM} = \frac{d}{dt}\left(\frac{1}{2} \cdot m_{COM} \cdot (v_{COM})^2 + m_{COM} \cdot g \cdot h_{COM}\right) \qquad \text{Eq 15}$$

$$P_{per} = \frac{d}{dt}\left(\sum_i^{22} \frac{1}{2}\overleftrightarrow{I}^i \cdot (\omega^i)^2 + \frac{1}{2}m^i(v_{COM}^i - v_{COM})^2\right) \qquad \text{Eq 16}$$

Where in addition to the terms defined in Eq 13, m_{COM} is the mass of the whole body, g is the acceleration due to gravity, and h_{COM} is the vertical position of the whole-body COM.

Mechanical power of each leg relative to a fixed lab frame was calculated as described in (Golyski and Sawicki, 2022) according to Eq 17, based on the individual limbs method (Donelan et al., 2002b), with the addition of mechanical power exchanged between each leg and the corresponding moving treadmill belt (Selgrade et al., 2017) and peripheral power of leg segments:

$$P_{Leg} = (F_{GRF} \cdot v_{COM}) + (F_{LEG} \cdot v_{TM}) + P_{per,leg} \qquad \text{Eq 17}$$

Where F_{GRF} is the force exerted by the leg on the whole body COM as measured by the instrumented treadmill, F_{LEG} is the force exerted by the leg on the ground (equal and opposite to F_{GRF}), v_{TM} is the velocity of the corresponding treadmill belt (logged at approximately 55 Hz), and $P_{per,leg}$ is the peripheral power (Eq 16) of only the leg segments relative to the whole boy COM. P_{Leg} should be equal to the sum of lower-limb joint powers, barring force and velocity measurement inaccuracies, contributions of lower

limb joint powers to peripheral powers of the head, arms, and trunk segments, and missing degrees of freedom of the leg (e.g., of the foot (Takahashi et al., 2012)). While $P_{Whole\ Body}$ could also be calculated using ground reaction forces and COM velocities as in (Zelik et al., 2015), kinematic measurements alone were used in this study to avoid the influence of force measurement errors leading to erroneous apparent net gains or losses of system energy during steady locomotion, at the expense of inaccuracies in modelled segment masses and inertias.

Sagittal plane lower limb joint mechanical powers were calculated as the product of joint moments and their respective joint angular velocities. Joint angular velocities were obtained by differentiating joint angles with respect to time. All kinetic and mechanical energetic measures were normalized to mass of each participant without the exoskeleton. Mechanical work values were calculated for each stride by integrating the respective mechanical powers with respect to time.

5.3.6 Electromyography

EMG analysis for use in calculation of RF fascicle and MTU mechanical energetics was similar to that of a previous study (Chapter 4). EMG sensors (Avanti, Delsys, MA) were placed on the bellies of 6 muscles of the left leg after light skin abrasion: the tibialis anterior, soleus, medial gastrocnemius, biceps femoris, gluteus maximus, and RF. Raw EMG signals were acquired at 2000 Hz. To obtain EMG envelopes, raw signals were first high-pass filtered at 10 Hz, then full-wave rectified, then low-pass filtered at 30 Hz using zero-phase Butterworth filters (Arnold et al., 2013; Buchanan et al., 2004). DC offsets were then removed by subtracting the lowest value of each envelope during a static resting trial.

Envelopes were then normalized between these lowest values and the maximum within-participant value across all trials. These normalized signals were then used as inputs to a first-order activation dynamics model (Zajac, 1989) with activation and deactivation time-constants of 35 and 58 ms, corresponding to a mixed fiber-type muscle (Dick et al., 2017; Johnson et al., 1973). As the RF was the principal muscle of interest in this work, plots of the remaining muscle activations are included as a supplementary figure (Figure 30).

5.3.7   Ultrasonography and Fascicle Tracking

Cine B-mode ultrasound images were acquired from the right rectus femoris of each participant at approximately 115 Hz in Echowave software using an ArtUS EXT-1H acquisition unit and a 60 mm long LV8-5N60-A2 probe (Telemed, Vilnius, LT). Beam angles were selected in Echowave to maximize the contrast of hyperechoic fascicles and aponeuroses (0 or -5 degrees). The probe was placed over the muscle belly at a similar level of the RF EMG sensor on the contralateral leg. Ultrasound images were synced in time with motion capture data using an external trigger signal.

Fascicle lengths were calculated from ultrasound images using a deep learning aponeurosis detector coupled with a previously described custom fascicle tracking application (Chapter 4). The addition of this approach to aponeurosis detection allows the custom fascicle tracker to be fully automated. Briefly, the original fascicle tracker used a hand-tracked region of interest on each image to identify snippets of fascicles based on physiological criteria, then used those snippets to calculate a representative pennation angle relative to the deep aponeurosis of the muscle, and finally calculated a representative fascicle length by dividing the thickness of the muscle by the sine of the representative

pennation angle. The previous custom fascicle tracking application contained a feature whereby the program would load in and automatically calculate fascicle lengths if a region of interest file containing aponeurosis borders was detected. Thus, generating these aponeurosis files using a deep learning approach (also implemented in Matlab) seamlessly integrates with the previous semiautomatic approach. The overarching design strategy of the deep learning aponeurosis detector was to re-train a previously developed U-net model architecture (Cronin, 2020) using a subset of images from the present study, thereby "overfitting" the model to perform best on the remaining images of the study. This approach allows for rapid training of models on a mid-range desktop computer and avoids having to collect a data set that generalizes across tasks, probes, participants, etc., at the cost of study-specificity and reproducibility (Leitner et al., 2021). In effect, this meant generating 1760 hand-tracked binary masks of aponeuroses from resized (to 512x512 pixels) but otherwise unfiltered images which spanned: (20 equally spaced frames across the perturbed stride) x (both timings) x (both legs) x (the most extreme (K3) and least extreme (K0) stiffness) x (all 11 participants). The previous U-net architecture (Cronin, 2020) was modified for use in Matlab with the replacement of the original sigmoid and binary cross-entropy loss layers with softmax and pixel classification layers, respectively. These data were then split into separate masks for the superficial and deep aponeuroses, for which separate models were trained. For each model, an 80%-20% training/validation split was used. The model was trained using the Matlab trainNetwork function with training parameters similar to that of a previous deep learning approach (Cronin, 2020). The specific training parameters are included in supplementary information (

96

Table 3). Note that separate models were also trained for each participant, but this did not lead to an appreciable improvement in performance. It took approximately 6 hours to train each model using a desktop computer with an Nvidia GTX 1660 Ti graphics card. Aponeurosis pixel classification performance indicated a 95% mean accuracy and 92% mean intersection over union for the deep aponeurosis, and a 97% mean accuracy and 95% mean intersection over union for the superficial aponeurosis. To convert classified pixels to aponeuroses, the largest feature of the classification output is fitted with a line through the centroid and major axis, and this line is then extended to the borders of the image.

To validate that this automated approach led to similar fascicle lengths as the previous semiautomated method when using hand-tracked aponeuroses, a subset of the data from a previous study (490 images from 28 trials spanning all participants, timings, and legs, Chapter 4) was used to generate deep and superficial aponeurosis detection models. These models were then used to automatically generate regions of interest for all frames from those 28 trials with no manual correction, from which fascicle lengths were automatically generated. Across all 28 trials (approximately 10,000 images) the RMSE between hand-tracked and fully automated methods after low-pass filtering and normalization to the gait cycle was (mean [sd]) 3.4 [1.3] mm, 2.3 [0.8] % of the maximum fascicle length, and had an R^2 of 94 [5]%. A representative trial is included as a supplementary figure (Figure 31).

For this study, the locations of the predicted aponeuroses were inspected for each frame, as facilitated by the semiautomated tracker, with a very small subset requiring manual correction (<1%). Thus, not including the time to automatically generate regions of interest (0.15 seconds/frame), the fully automated tracking speed is only limited by the

semiautomated algorithm update speed (0.2 seconds/frame). Although generating the hand-tracked binary masks for training the aponeurosis network may be time intensive, for this study those 1760 hand tracked images allowed for automated tracking of ~430,000 images.

Fascicle lengths and pennation angles calculated using the custom applications were used in subsequent analyses after being low-pass filtered at 6 Hz using a zero-phase Butterworth filter.

5.3.8 Estimation of Fascicle and Muscle-Tendon Unit Mechanical Energetics

Mechanical powers at the RF fascicle and MTU levels were calculated with a previously described method ((Dick et al., 2017) and Chapter 4) using fascicle lengths in addition to RF activations to drive a Hill-type model of RF fascicle force generation. These fascicle forces were converted to MTU forces by multiplication by the cosine of the pennation angle (relative to the deep aponeurosis). Briefly, the Hill-type model used independent contributions of activation, length, and velocity to force based on phenomenological relationships and empirical parameters to estimate fascicle forces (Azizi and Roberts, 2010; Dick et al., 2017; Hill, 1938; Otten, 1987; Zajac, 1989). The only alteration here from the approach used in Chapter 4 is that the fascicle slack lengths were based on average within-participant fascicle lengths at 50% of the pre-perturbation gait cycle in the K0 exoskeleton condition, as opposed to a no-exoskeleton condition (126 mm on average across participants). Since EMG and B-mode ultrasound lengths were collected from different legs, for muscle-level analyses perturbations were collapsed across iterations and sides within each exoskeleton configuration and participant. Fascicle powers

were calculated as the product of fascicle forces with fascicle velocities obtained by differentiating fascicle lengths with respect to time. MTU powers were calculated as the product of MTU forces and MTU velocities (the time derivative of MTU lengths). For both fascicles and the MTU, velocities were negated so lengthening resulted in negative powers. Mechanical works at the fascicle and MTU levels were calculated as the integral of the respective mechanical powers in time. All kinetic and mechanical energetic measures at the fascicle and MTU levels were normalized to mass of each participant without the exoskeleton.

5.3.9   Statistics

Because exoskeleton effects can vary widely across individuals (Zhang et al., 2017), and passive hip exoskeletons generally lead to small and variable effects (Panizzolo et al., 2019), linear mixed models were used to assess the main effect of exoskeleton stiffness on the principal outcome measures for the pre-perturbation stride ("S-1"), the perturbed stride ("S0"), and the first recovery stride ("S+1"), where strides were defined by the leg ipsilateral to the perturbation. In addition to metrics for exoskeleton characterization, the principal discrete outcome metrics were sagittal WBAM range and multi-scale mechanical works. These metrics were statistically compared on the S-1 stride to determine steady-state effects of the exoskeleton, and their differences from steady state (i.e. value at S+N – values at S-1) was used to evaluate them on the S0 and S+1 strides to remove the influence of steady-state effects of exoskeleton stiffness. For external outcome measures (i.e., not fascicle and MTU mechanics), the linear mixed models incorporated fixed factors of exoskeleton stiffness, perturbation timing, the stiffness x timing interaction, and iteration, in addition to random factors of participant and the side of the perturbation. Since data

were collapsed for fascicle and MTU mechanics, statistical models for those variables did not include perturbation side and iteration. Estimated marginal means were used to perform Bonferroni-corrected pairwise post-hoc tests and for graphical representation of metrics. Significance was concluded for $p \leq 0.05$. All statistical tests were performed in SPSS (IBM, Armonk, NY).

5.4   Results

5.4.1   Exoskeleton Mechanics

As estimated from mechanism angles and benchtop characterization, the exoskeleton produced torque from midstance to toe-off (30-66% of the gait cycle), with increasing stiffness leading to increasing torque on all strides ($p<0.001$). Peak exoskeleton torques were higher on the perturbed leg during the perturbed stride for early vs. late stance perturbations ($p<0.001$). During the first recovery stride, on the contralateral leg, exoskeleton torques across all stiffnesses were lower ($p=0.002$) due to decreased mechanism extension ($p<0.001$), particularly following late stance perturbations. Higher exoskeleton stiffnesses were also associated with lower peak mechanism extension angles ($p<0.001$), and bias towards larger mechanism flexion angles ($p<0.001$).
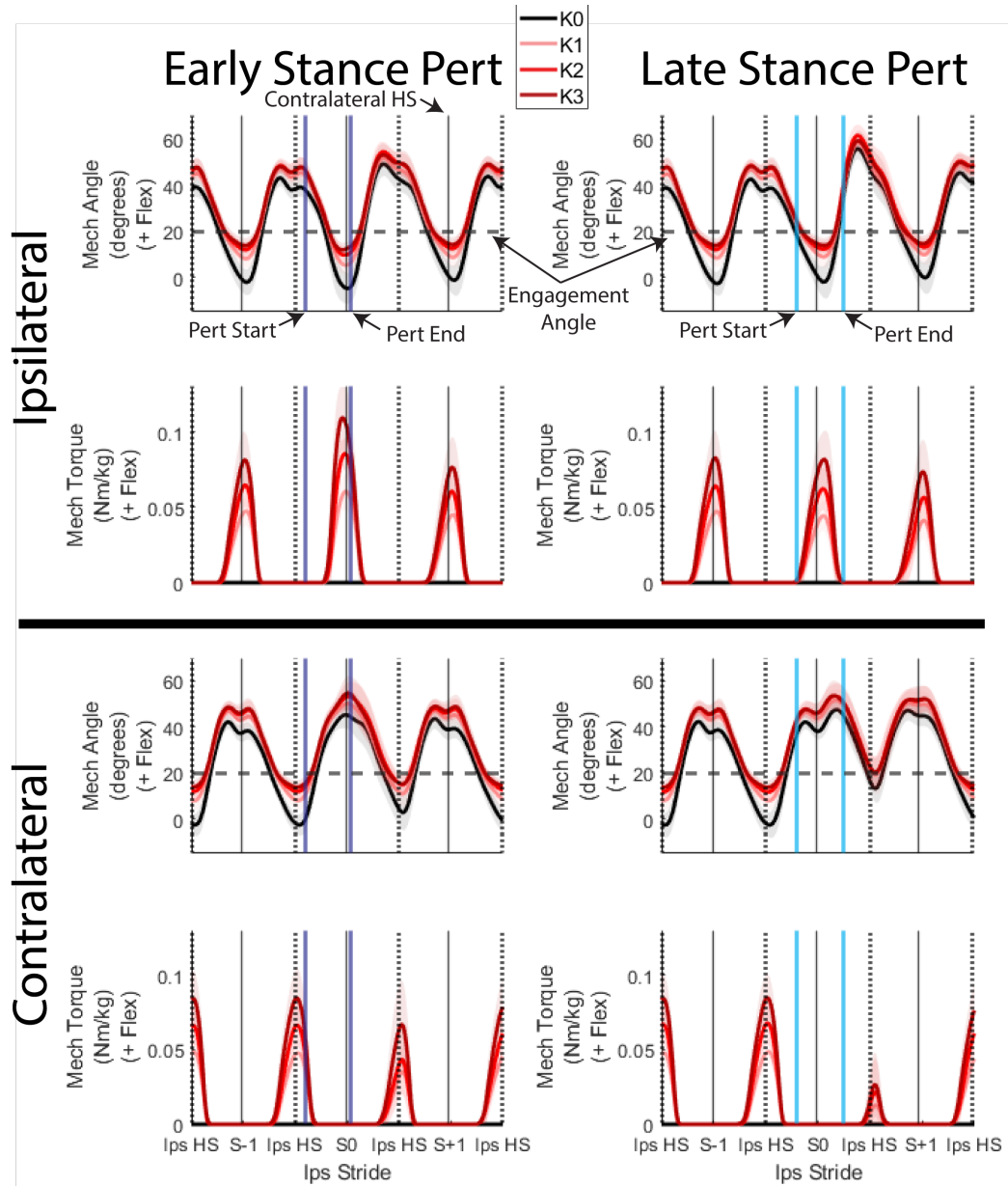
Figure 20 – Across-participant ensemble averaged exoskeleton mechanism angles and torques for the stride before (S-1), stride of (S0), and stride after (S+1) the perturbation. Exoskeleton torques are normalized to the mass of each participant not wearing the device. Shaded regions indicate ±1 standard deviation.

5.4.2 Sagittal Whole-Body Angular Momentum

WBAM results are shown in Figure 21. During steady state walking, increasing exoskeleton stiffness resulted in larger WBAM ranges (p<0.001). On the perturbed stride,

there was a significant effect of exoskeleton stiffness on the change in WBAM from steady state ($p=0.029$), though the directionality of the relationship relative to the no-spring condition was stiffness dependent. Pairwise comparisons demonstrated that for the early stance perturbations only, the K3 condition resulted in a larger increase in WBAM range than the K1 condition ($p=0.030$). On the first recovery stride, there were also significant effects of stiffness ($p=0.031$), though no significant pairwise comparisons ($p>0.494$). With respect to timing of the perturbation, early vs. late stance perturbations resulted in larger increases in WBAM range on the perturbed stride, but smaller increases on the first recovery stride ($p<0.001$ for both).
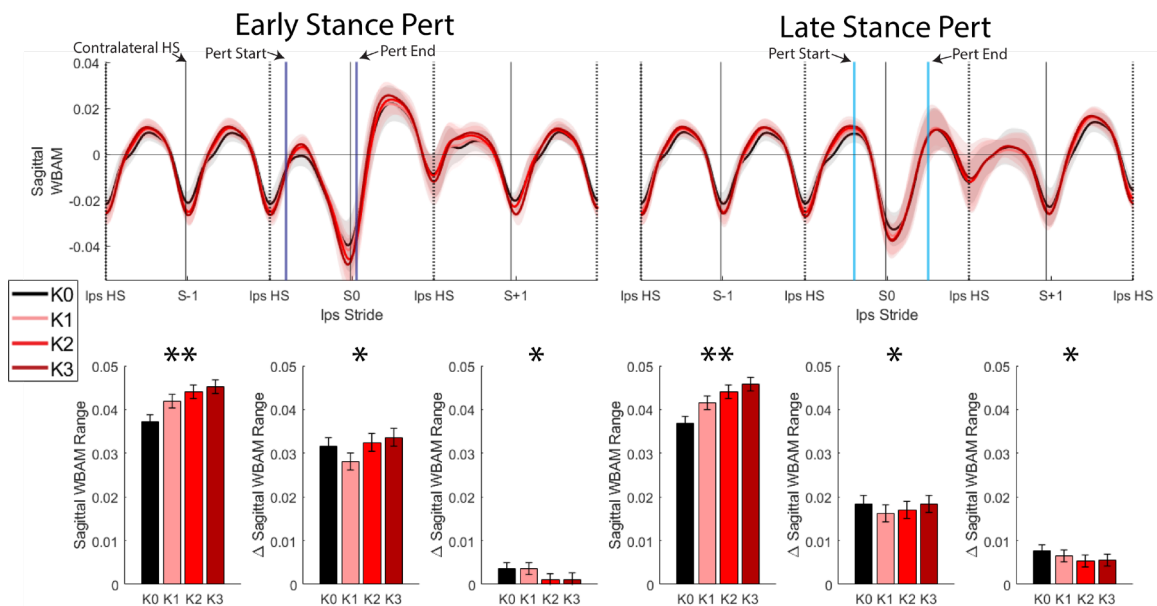
Figure 21 – Exoskeleton effects on stability as measured by sagittal plane whole-body angular momentum (WBAM). Top row: across-participant ensemble averages of sagittal WBAM for the stride before (S-1), during (S0), and after (S+1) the perturbation. Shaded regions represent ±1 standard deviation. Bottom row: sagittal WBAM range during the S-1 stride, and changes in ranges from steady state levels. For all measures, sagittal WBAM was normalized to participant body mass with no exoskeleton, height, and steady state walking speed (1.25 m/s). Error bars represent ±1 standard error. ** and * represent significant main effects of stiffness with $p<0.001$ and $p<0.050$, respectively. Positive angular momentum is defined as backward pitching.

5.4.3 Whole-Body Mechanical Energetics

Whole-body mechanical powers and works are shown in Figure 22. There were no significant effects of exoskeleton stiffness on whole-body mechanical work during either timing on any stride (p>0.226). With respect to timing, on the perturbed stride, early vs. late stance perturbations resulted in smaller positive whole-body work demands (p<0.001). On the first recovery stride, early vs. late stance perturbations resulted in smaller negative whole-body work demands (p<0.001).
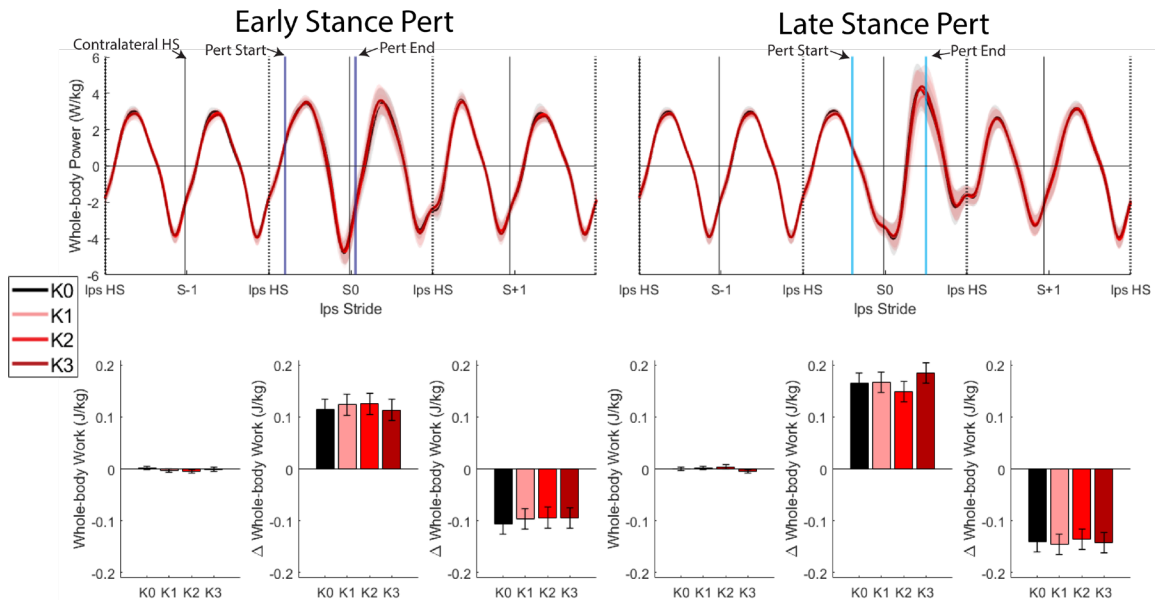
Figure 22 – Exoskeleton effects on whole-body mechanical energetics. Top row: across-participant ensemble averages of whole-body mechanical power for the stride before (S-1), during (S0), and after (S+1) the perturbation. Shaded regions represent ±1 standard deviation. Bottom row: whole-body mechanical work during the S-1 stride, and changes in mechanical works from steady state levels. Works and powers were normalized to participant body mass with no exoskeleton. Error bars represent ±1 standard error. There were no significant effects of exoskeleton stiffness on any whole-body work value.

5.4.4   Leg Mechanical Energetics

Mechanical powers and works for individual legs are shown in Figure 23. During steady state, there was a significant effect of stiffness on ipsilateral leg work ($p=0.033$), but not contralateral leg work ($p=0.101$). Since both legs should have similar trends during steady state walking over a stride, this indicates there may not have been an effect of stiffness during steady state overall. Aside from steady state, there was only a significant effect of stiffness on the perturbed side and the contralateral leg ($p=0.033$, $p>0.084$ otherwise), with a slight increase in work with higher exoskeleton stiffnesses. Timing had a significant effect during the perturbed and first recovery strides on both sides ($p<0.020$). On the ipsilateral leg, early vs. late stance perturbations were associated with increased leg work on the perturbed stride, but decreased leg work during the first recovery stride. On the contralateral leg, during the perturbed stride there was increased leg work on the perturbed stride during late stance, but not early stance perturbations.
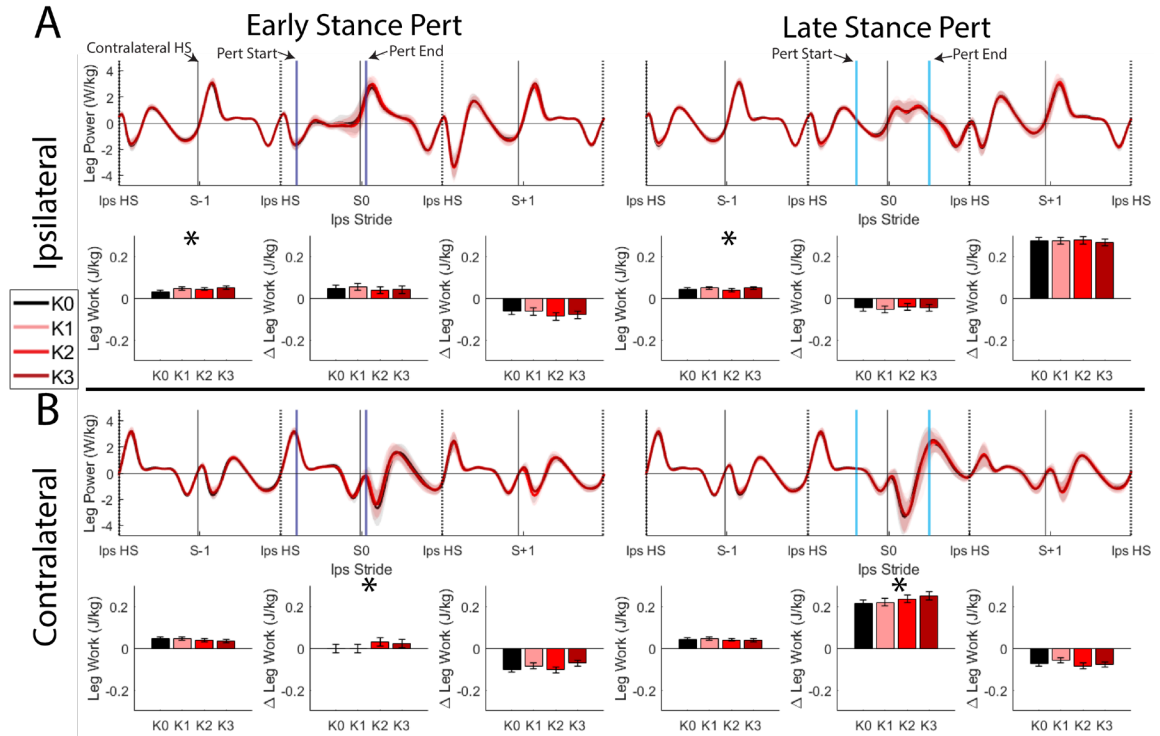
Figure 23 - Exoskeleton effects on A) the leg ipsilateral to the perturbation, and B) the leg contralateral to the perturbation. Within each leg, the top row shows across-participant ensemble averages of leg mechanical power for the stride before (S-1), during (S0), and after (S+1) the perturbation. Shaded regions represent ±1 standard deviation. Within each leg, the bottom row shows leg mechanical work during the S-1 stride, and changes in mechanical works from steady state levels. Works and powers were normalized to participant body mass with no exoskeleton. Error bars represent ±1 standard error. * represents a significant main effects of stiffness with p<0.050.

5.4.5 Lower Limb Joint Mechanical Energetics

Sagittal hip mechanical powers and works are shown in Figure 24. During steady state walking, on both sides there was a slight but significant (p<0.001) increase in hip work performed with increasing exoskeleton stiffness, driven primarily by differences from the K0 condition. On the perturbed stride, there was a significant effect of exoskeleton stiffness on ipsilateral (p=0.008), but not contralateral (p=0.059), hip work from steady state. At the ipsilateral hip, for early stance perturbations, the K2 condition was associated

with increased hip work than the K1 condition (p=0.048), while for late stance perturbations, the K2 condition was associated with increased hip work than the K3 condition (p=0.006). On the first recovery stride, there was only an effect of exoskeleton stiffness on the contralateral hip (p=0.046), with decreased hip work in the K1 than K0 conditions during the late stance perturbations approaching significance (p=0.051). The effect of timing was significant on both sides and strides (p<0.001 for all), with early vs. late stance perturbations resulting in decreased ipsilateral hip work on the perturbed stride and first recovery strides. On the contralateral side, early stance perturbations resulted in increased hip work, while late stance perturbations resulted in decreased hip work on the perturbed stride. On the first recovery stride, late stance perturbations resulted in increased hip work relative to early stance perturbations.

Figure 24 – Exoskeleton effects on A) the hip ipsilateral to the perturbation, and b) the hip contralateral to the perturbation. For each side, the top row shows across-participant ensemble averages of sagittal hip mechanical power for the stride before (S-1), during (S0), and after (S+1) the perturbation. Shaded regions represent ±1 standard deviation. Within each side, the bottom row shows sagittal hip mechanical work during the S-1 stride, and changes in mechanical works from steady state levels. Works and powers were normalized to participant body mass with no exoskeleton. Error bars represent ±1 standard error. ** and * represent significant main effects of stiffness with $p<0.001$ and $p<0.050$, respectively.

Sagittal knee mechanical powers are included as a supplementary figure (Figure 32). The only significant effect of stiffness across all strides was during steady state on the ipsilateral side ($p=0.049$). As was the case for works at the leg level, there should be no difference between ipsilateral and contralateral works during steady state, so this difference is likely not meaningful. Timing had a significant effect on the perturbed and first recovery stride, in addition to both sides ($p<0.001$ for all). On the perturbed stride at the ipsilateral knee, there was a shift towards increased knee work during early vs. late stance

perturbations. Conversely, on the perturbed stride at the contralateral knee, there was a shift towards decreased knee work during early stance perturbations, but increased knee work for late stance perturbations. On the first recovery stride, both the ipsilateral and contralateral knees exhibited a slight shift towards increased knee work during late vs. early stance perturbations.

Sagittal ankle mechanical powers and works are also included as a supplementary figure (Figure 33). During steady state, for both the ipsilateral and contralateral ankles there was a significant effect of stiffness (ipsilateral: $p<0.001$, contralateral: $p=0.002$), with increasing stiffness being associated with slight increases in ankle work. On the perturbed stride there was a significant effect of stiffness for the ipsilateral ankle ($p=0.037$), though there was no obvious directionality to this effect. There was no significant effect of stiffness for the contralateral ankle on the perturbed stride, nor either side on the first recovery stride ($p>0.121$). There were significant effects of timing on both sides and the perturbed and first recovery strides ($p<0.001$ for all). For the ipsilateral ankle, early stance perturbations predominantly resulted in an increase in work on the perturbed as opposed to first recovery stride, while late stance perturbations resulted in an increase in work predominantly on the first recovery stride and not the perturbed stride. For the contralateral ankle, late vs. early stance perturbations resulted in increased work on the perturbed stride and decreased work on the first recovery stride.

5.4.6   Rectus Femoris Mechanical Energetics

RF powers and works at the MTU and fascicle levels are shown in Figure 25 and Figure 26, respectively. RF fascicle and MTU lengths, activations, and forces are included

as a supplementary figure (Figure 34). At the MTU level, there was no effect of exoskeleton stiffness on the steady state, perturbed, or first recovery stride ($p>0.073$). However, there were significant effects of timing ($p<0.001$). On the perturbed stride for both sides, early stance perturbations resulted in less negative RF MTU work than late stance perturbations. On the first recovery stride on the contralateral side, late stance perturbations resulted in increased RF MTU work compared to early stance perturbations. At the fascicle level, there was only an effect of exoskeleton stiffness during steady state on both sides ($p<0.017$), with a trend towards increased negative fascicle work with increasing exoskeleton stiffness. There was a significant effect of timing on the contralateral leg during the perturbed ($p=0.001$) and first recovery strides ($p<0.001$). On the perturbed stride, early vs. late stance perturbations resulted in more negative work - consistent with the MTU level. On the first recovery stride, late stance perturbations resulted in more negative work compared to early stance perturbations, which was not consistent with the MTU level.
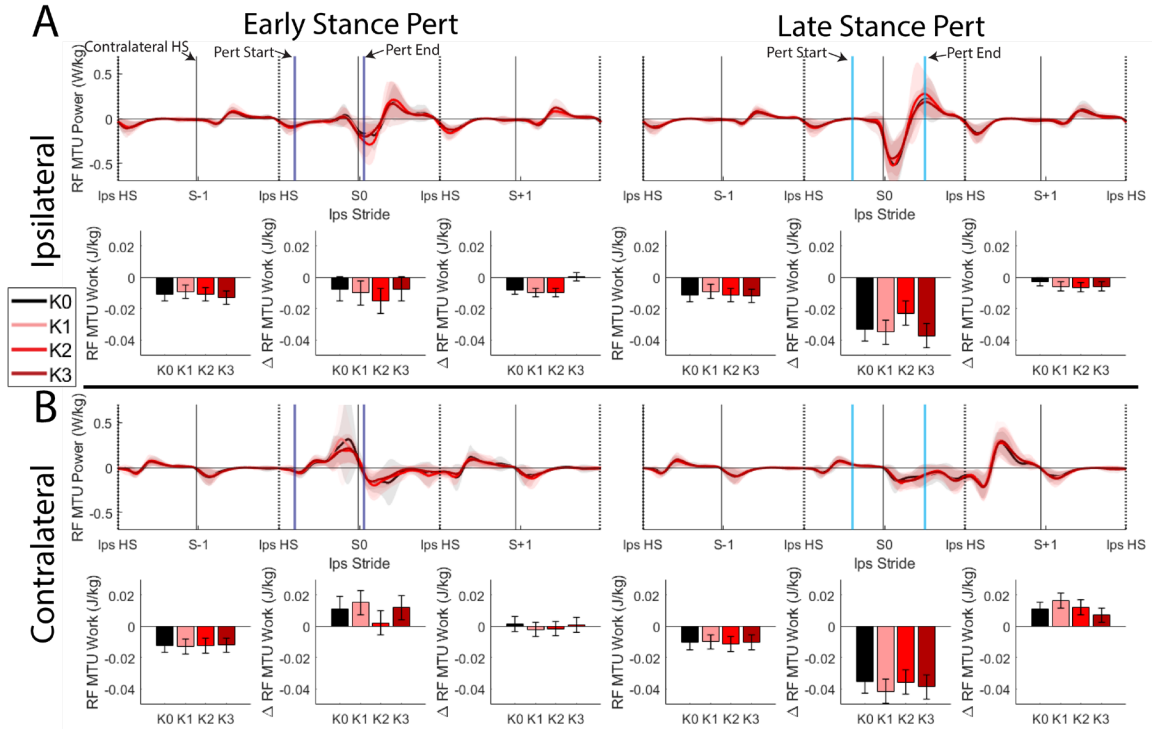
Figure 25 - Exoskeleton effects on A) the rectus femoris (RF) muscle-tendon unit (MTU) on the leg ipsilateral to the perturbation, and B) the RF MTU on the contralateral leg. For each side, the top row shows across-participant ensemble averages of RF MTU mechanical power for the stride before (S-1), during (S0), and after (S+1) the perturbation. Shaded regions represent ±1 standard deviation. Within each side, the bottom row shows RF MTU mechanical work during the S-1 stride, and changes in mechanical works from steady state levels. Works and powers were normalized to participant body mass with no exoskeleton. Error bars represent ±1 standard error. There were no significant effects of exoskeleton stiffness on any RF MTU work value.
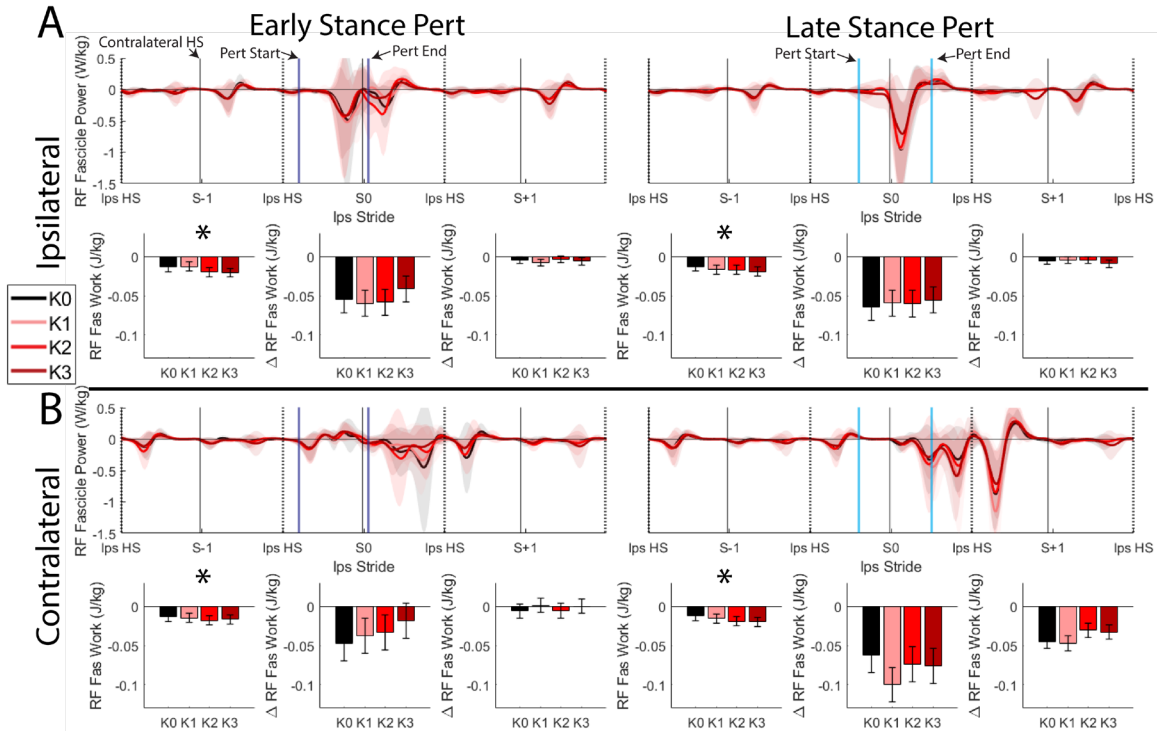
Figure 26 - Exoskeleton effects on A) the rectus femoris (RF) fascicles on the leg ipsilateral to the perturbation, and B) the RF fascicles on the contralateral leg. For each side, the top row shows across-participant ensemble averages of RF fascicle mechanical power for the stride before (S-1), during (S0), and after (S+1) the perturbation. Shaded regions represent ±1 standard deviation. Within each side, the bottom row shows RF fascicle mechanical work during the S-1 stride, and changes in mechanical works from steady state levels. Works and powers were normalized to participant body mass with no exoskeleton. Error bars represent ±1 standard error. * represents a significant main effect of exoskeleton stiffness with p<0.05.

5.5 Discussion

The main objective of this study was to relate the effects of a passive hip exoskeleton on multi-scale mechanical energetics and stability during perturbed walking. To accomplish this objective, we imposed destabilizing energetic demands using rapid unilateral belt accelerations while individuals walked with a custom passive hip exoskeleton. We quantified stability using sagittal WBAM range and mechanical energetics using mechanical work at the level of the whole-body down to the level of RF

fascicles using musculoskeletal modeling coupled with *in-vivo* measurement techniques ((Dick et al., 2017; Golyski and Sawicki, 2022), Chapter 4).

Our first hypothesis (H1) was that a shift in the whole-body energetic demand towards steady state levels would be associated with an improvement in stability, as evidenced by a decreased range in WBAM. Our data did not support this hypothesis, as there was no significant change in whole-body work due to the exoskeleton, while there were stiffness-dependent effects on WBAM range during both steady state and the perturbed periods. This finding points to a fundamental disconnect between whole-body stability from the perspectives of WBAM and mechanical energetics. From the energetics perspective, stability cannot be assessed during a "steady state" level ground stride since there is little (and on average across many strides, zero) energy flowing into or out of the body on net over a stride that must be dissipated or re-generated for the body to return to steady-state levels. However, from the perspective of WBAM, a larger WBAM range, as usually assessed during steady state walking, is indicative of decreased stability (Honda et al., 2019; Nott et al., 2014; Silverman and Neptune, 2011; Vistamehr et al., 2016), since WBAM is thought to be "tightly regulated" and fluctuate within a narrow range during walking (Herr and Popovic, 2008). Thus, from the WBAM perspective, our data indicated the passive hip exoskeleton was destabilizing during unperturbed walking. Relating our findings to literature, digitized data indicated individuals with vs. without unilateral lower limb amputation have a 45% larger normalized sagittal WBAM range during walking at 1.2 m/s (Silverman and Neptune, 2011), while we observed a 25% increase in normalized WBAM range from the no spring to the highest stiffness conditions at 1.25 m/s in this study. Incorporating the added mass of the exoskeleton into WBAM normalization results

in a 21% increase in WBAM range from the no spring to highest stiffness conditions. In the context of the perturbation, we found that both early and late stance perturbation timings generally elicited demands of net positive work on the perturbed stride and net negative work on the first recovery stride – demands that were not shifted by the exoskeleton and indicated no effect on stability from a mechanical energetics perspective. However, from the WBAM perspective, we found that the steady-state increase in WBAM range was partially offset in the K1 condition, but not the K2 and K3 conditions, which suggests that for low stiffnesses or flexion torques the deleterious consequences of a hip exoskeleton during steady state walking may not translate to perturbed contexts.

Our second hypothesis (H2) was that improved stability as measured by decreased WBAM range would be associated with shifts in mechanical work at the hip joints, RF MTUs, and RF fascicles that opposed whole-body energetic demands during the perturbation. This hypothesis was based on previous passive exoskeletons altering the net work at the joints they target (Collins et al., 2015; Lewis and Ferris, 2011), and shifts in dynamics of plantarflexor muscles to lower forces and altered lengths/velocities during use of elastic ankle exoskeletons (Farris et al., 2013; Nuckols et al., 2020a). Our data did not support a connection between local energetic changes induced by the exoskeleton and improvement of stability during the perturbed period. As previously mentioned, the only exoskeleton stiffness where WBAM range decreased on the perturbed stride relative to its steady state level was the K1 stiffness, but mechanical work at the level of legs, joints, or the RF MTU and fascicles did not exhibit a significant decrease in the K1 condition to oppose the whole-body demand of positive net work. Indeed, effects of stiffness on mechanical work during the perturbed and first recovery strides at all levels were minimal,

113

with limited clear trends with increasing stiffness aside from an increase in contralateral leg work during the late stance perturbation, which was not explained by trends at the joint levels. However, during steady state strides, increasing exoskeleton stiffness led to slight but significant increases in net work at the hip and ankle, in addition to increased negative work at the level of RF fascicles. Despite these changes being small in relation to the fluctuations in work during the perturbation, re-normalizing these data to account for the added mass in each exoskeleton condition did not alter this effect (hip: $p<0.006$, ankle: $p<0.005$, RF fascicles: $p<0.019$). This finding has three potential implications. First, these findings suggest that during steady state walking, added mass may lead to disproportionately higher net work demands at the hip and ankle, despite added mass not changing the net work over a stride performed by the leg or body. This extends previous findings which demonstrated these joints play large roles in mediating energetic demands of sprinting and sloped walking (Montgomery and Grabowski, 2018; Schache et al., 2019). Second, a previous study (Chapter 4) found that in responding to energetic demands of a belt acceleration perturbation, changes in RF fascicle work were positively associated with changes in hip work, but negatively associated with changes in knee work. While this relationship holds with our present findings during the perturbed period, this steady state result may imply such a relationship is not present during small energetic changes during unperturbed walking. Lastly, assuming these energetic changes are indeed due to the device and not the added mass alone, our findings suggest that while a passive device may not be able to change the energetics at the whole-body level, it may be capable of small changes in "local" energetics at the joint and muscle levels. This bias towards increased hip work with a passive hip exoskeleton is consistent with the rationale for this study (Lewis and

Ferris, 2011), but also suggests any steady state effects are overridden rather than harnessed during the energetic fluctuations of a perturbation.

Overall, our results indicated limited effects of the passive hip exoskeleton on leg energetics, but appreciable effects on WBAM – how might this have occurred? One theoretical reason for this is the mathematical attribution of the added mass of the exoskeleton to the trunk segment. However, separating WBAM into contributions of the trunk and the contributions of the legs reveals there was not a vertical shift in trunk angular momentum as would be caused by an increase in inertia or mass, but rather a phase shift (supplementary Figure 35). This phase shift of trunk angular momentum together with the invariant fluctuations of the leg contribution led to a "constructive interference" which precipitated higher peak to peak fluctuations in WBAM. Thus, the effects of the exoskeleton on stability from the WBAM perspective occurred not from the effects of the exoskeleton on the legs, but instead changes in trunk kinematics induced by the exoskeleton.

The present study had three important limitations. First, the torque produced by the exoskeleton was lower than anticipated, which likely contributed to the limited effects of the device at the leg level. Relative to literature, however, our highest stiffness condition produced a torque of 0.075 Nm/deg, which is 66% larger than the average torque of a low-profile passive hip flexion device which lowered the metabolic cost of walking in older adults (Panizzolo et al., 2019), and within the range of flexion torques (0.05 to 0.11 Nm/kg) considered to result in changes in joint powers (Haufe et al., 2020). However, such assistive hip torques do fall below that of peak flexion torques determined to be metabolically optimal (0.2 Nm/kg; (Bryan et al., 2020)). Further, the TPHE was designed to produce

torques up to 30 Nm based on unassisted kinematic profiles (approximately 0.4 Nm/kg), and we did not observe large changes in hip angle during device use (Figure 28). Additional analysis of lumbar and mechanism kinematics revealed that this lost device torque was not due to changes in lumbar flexion angle, but rather angular displacements of the mechanism components relative to the body. An accounting of the angular displacements of the individual components of the mechanism indicated that under load there was both a downward pitch of the pelvis section of the mechanism and an upward pitch of the thigh section of the mechanism, which together resulted in the lost kinematic displacement (supplementary Figure 36). Thus, future iterations of this device should adopt more rigid interfaces at both the torso and thigh to improve coupling between body and mechanism kinematics. The second limitation of this study is that estimates of RF mechanical energetics may be inaccurate due to use of Hill-type models for prediction of RF force. This limitation is discussed in further depth in Chapter 4, but briefly, Hill-type models provide a simplified estimate of muscle force by assuming independent relationships between muscle activation, length, and velocity determined at maximal activations. Thus, such models cannot capture changes in muscle force due to the relationships between activation, length, and velocity (Brown et al., 1999; Close, 1972; Holt and Azizi, 2014; Perreault et al., 2003), nor history dependent effects (Libby et al., 2020; Shue and Crago, 1998), which may be relevant to the forces produced during perturbations (de Groote et al., 2017). Nonetheless, we chose to use these models since they are the current standard for computational estimation of muscle force (Arnold et al., 2010; Delp et al., 2007), and by using inputs from *in-vivo* EMG and ultrasound measurements, we maintain our approach serves as an improvement over purely simulated analysis. The third limitation is related to

the context of this study. We investigated the effect of the exoskeleton in healthy, able-bodied participants and using stereotyped perturbations. Thus, the effects of the device could be different, and are anticipated to be larger, in balance impaired populations which lack tight control over sagittal WBAM fluctuations (Honda et al., 2019; Silverman and Neptune, 2011). Further, different types of perturbations could elicit different effects of the device. For example, pelvis pulls (e.g., (Vlutters et al., 2018)) may induce alterations in torso kinematics, which could in turn lead to different device torque profiles than treadmill belt accelerations.

To conclude, this study investigated the effects of a passive hip exoskeleton on mechanical energetics and stability during walking with transient unilateral treadmill belt perturbations. While we hypothesized the exoskeleton could alter whole-body perturbation energetics by changing the mechanical works at the local muscle and joint levels to improve stability, we instead found that the exoskeleton primarily led to higher WBAM fluctuations during steady state walking and had limited effects on the energetics of the legs during the perturbation. These findings demonstrate: 1) the discrepancy between stability definitions based in energetics vs. WBAM range, 2) that small steady-state trends in mechanical energetics with passive devices may not be capable of being leveraged to modulate perturbation energetics, and 3) changes in trunk dynamics caused by hip flexion assistance may have deleterious effects on stability from the perspective of WBAM. Future studies seeking to link stability and mechanical energetics should consider using devices that can directly inject or extract energy to modulate whole-body demands.

5.6 Ethics

All participants provided written informed consent and all protocols were approved by the Institutional Review Board at the Georgia Institute of Technology (Protocol H21076).

5.7 Data Accessibility

The biomechanical data for all participants (N=11) will be available at: https://sites.gatech.edu/hpl/archival-data-from-publications/

5.8 Authors' Contributions

Pawel R. Golyski and Gregory S. Sawicki conceived of the study and designed the experimental protocol; Pawel R. Golyski and Nicholas Swaich designed the exoskeleton and carried out the experiments. Pawel R. Golyski analyzed the data and drafted the manuscript; Pawel R. Golyski, Nicholas Swaich, and Gregory S. Sawicki edited the manuscript. All authors gave final approval for publication.

5.9 Competing Interests

We declare no competing interests.

5.10 Funding

5.11 Acknowledgements

5.12 Supplementary Figures for Chapter 5
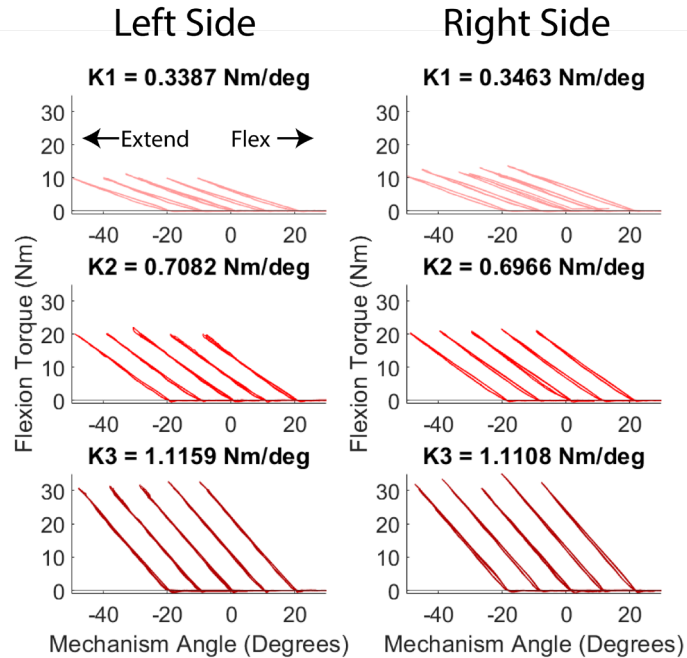
Figure 27 – Benchtop torsional mechanisms characterization results. Each plot represents 15 sweeps of the mechanism: 5 different engagement angles and 3 trials per engagement angle
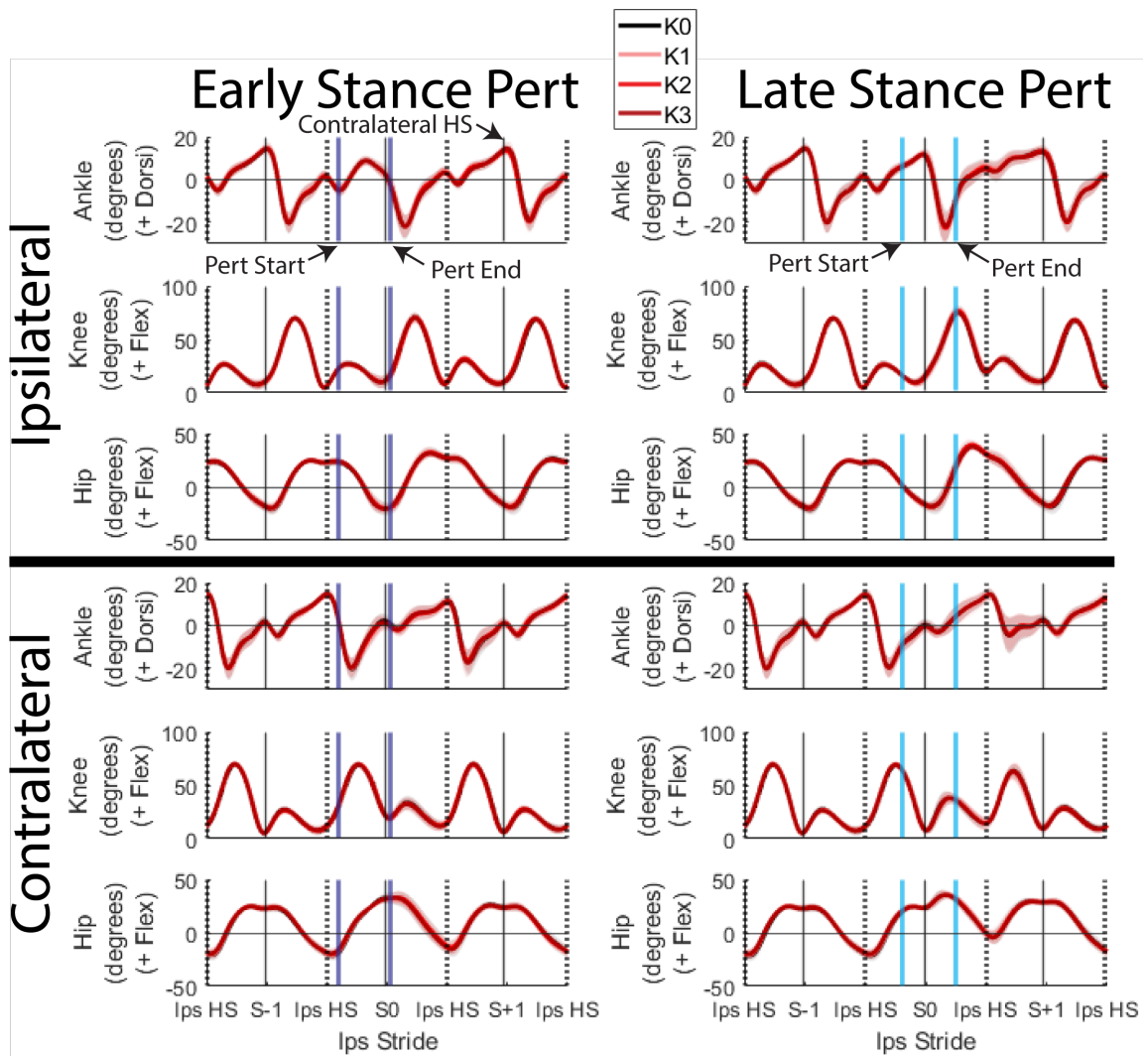
Figure 28 – Across-participant ensemble averaged sagittal plane joint angles for the stride before (S-1), stride of (S0), and stride after (S+1) the perturbation. Shaded regions represent ±1 standard deviation.
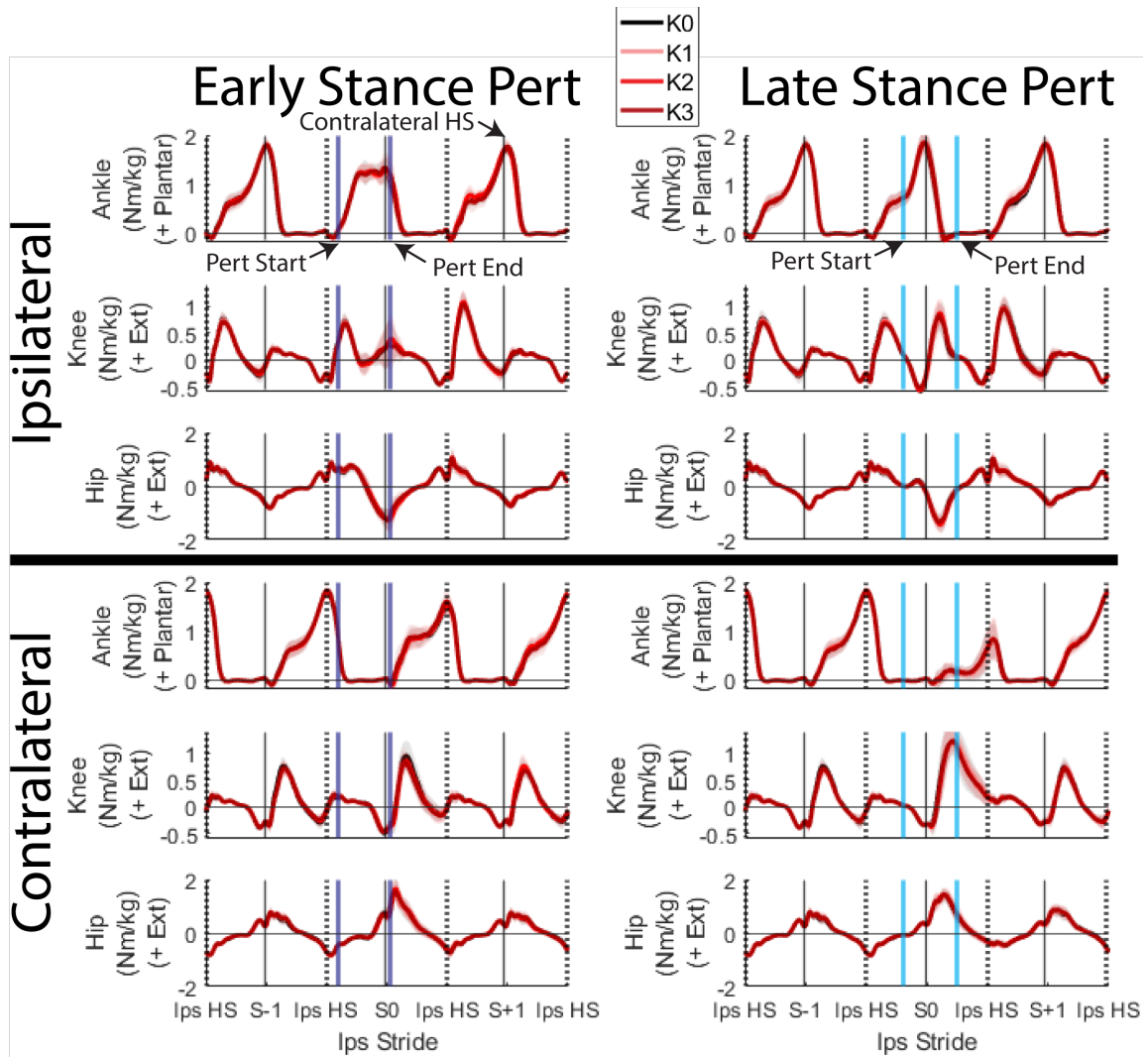
Figure 29 – Across-participant ensemble averaged sagittal plane joint moments normalized to participant mass with no exoskeleton for the stride before (S-1), stride of (S0), and stride after (S+1) the perturbation. Exoskeleton torque contribution were not subtracted from hip moments as the device crossed both the hip and lumbar joints. Shaded regions represent ±1 standard deviation.
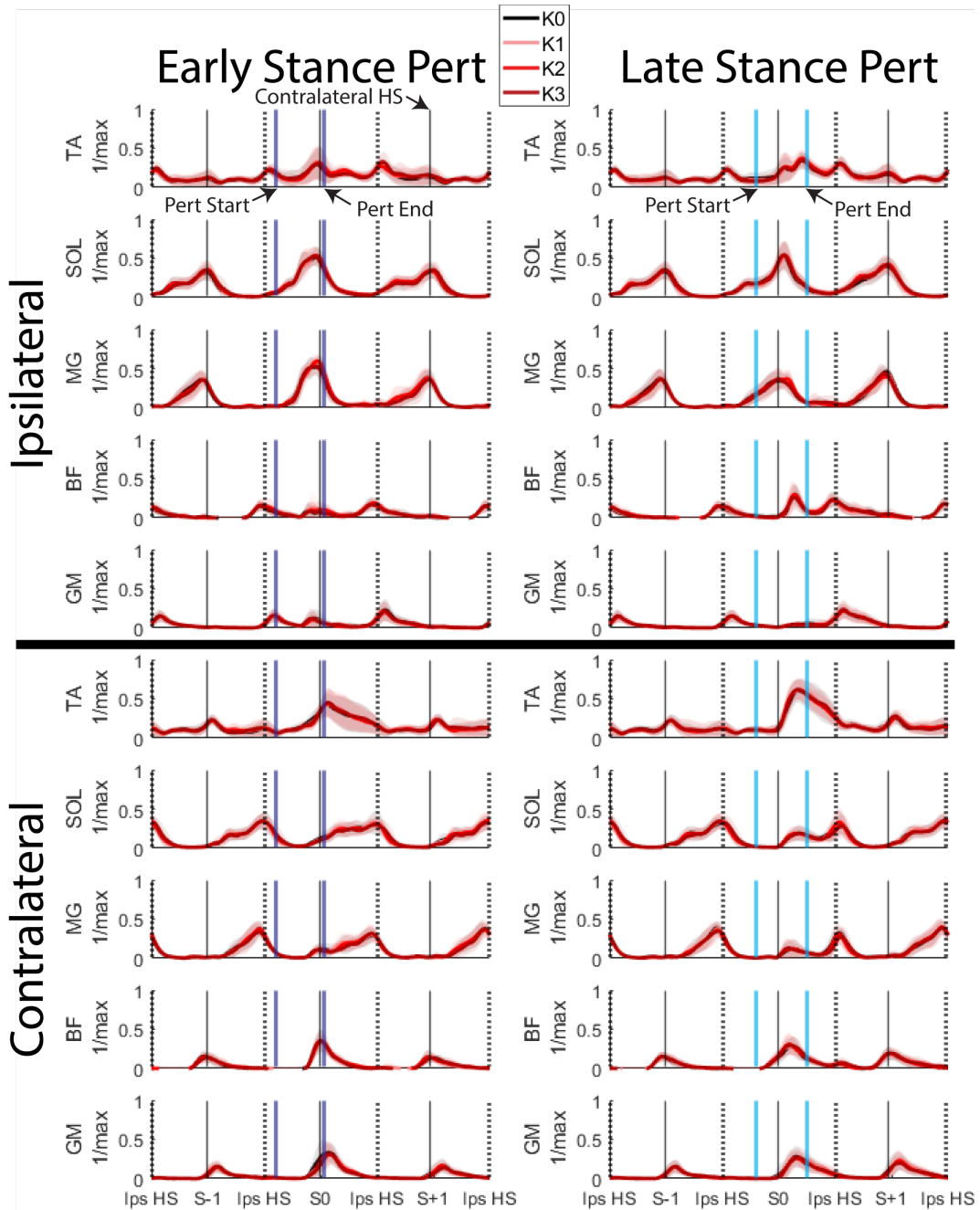
Figure 30 – Across-participant ensemble averaged muscle activations normalized to the maximum seen across all trials within each participant for the stride before (S-1), stride of (S0), and stride after (S+1) the perturbation. Shaded regions represent ±1 standard deviation.

Table 3 – Deep learning aponeurosis detector model training parameters (trainingOptions in Matlab)

Parameter	Value
Optimizer	Adam
InitialLearnRate	0.001
MaxEpochs	60
MiniBatchSize	2
ValidationPatience	8
ValidationFrequency	704 (once per epoch)
LearnRateDropFactor	0.1
LearnRateDropPeriod	10
LearnRateSchedule	piecewise
Plots	training-progress
ValidationData	test set composed of 20% of labelled images
Epsilon	1e-7
GradientDecayFactor	0.9
SquaredGradientDecayFactor	0.999
Shuffle	Every epoch
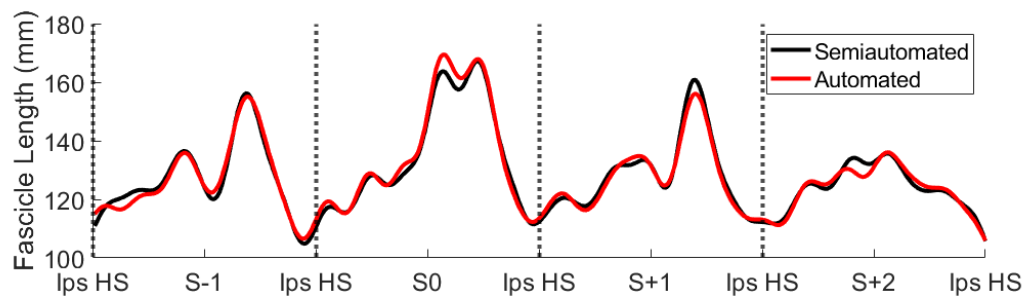
Figure 31 – Semiautomated vs. automated tracking performance on 1 of the 28 trials
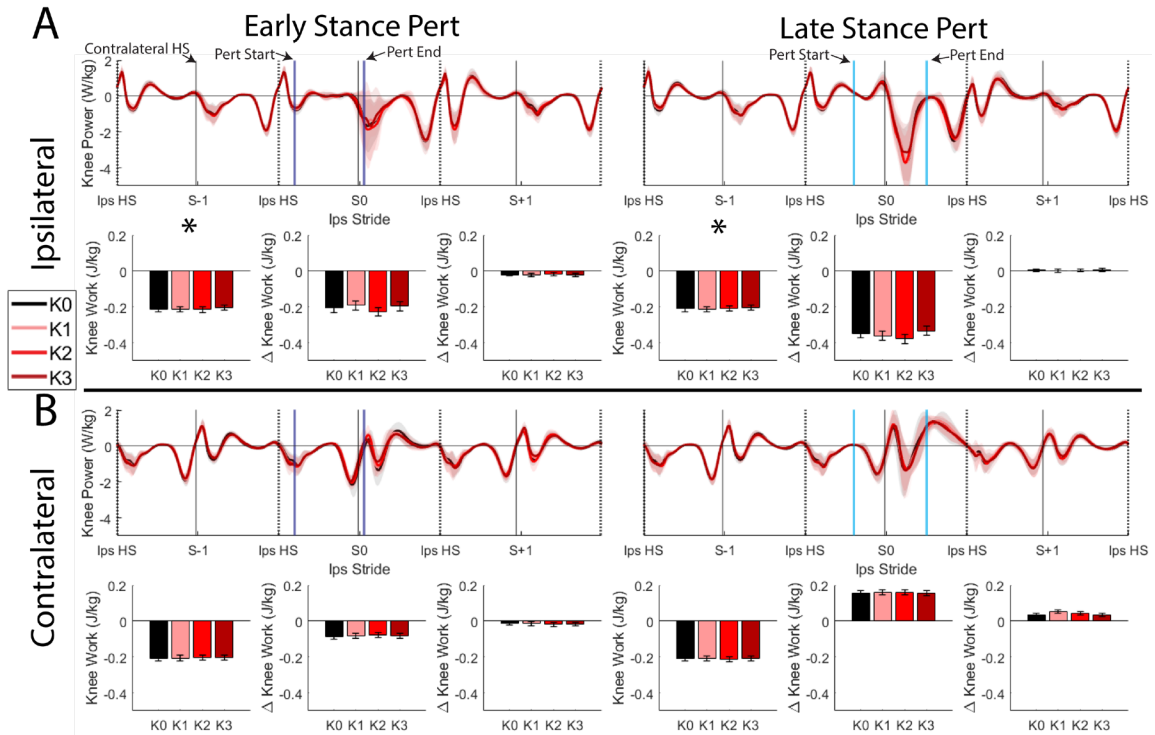
Figure 32 - Exoskeleton effects on A) the knee ipsilateral to the perturbation, and b) the knee contralateral to the perturbation. For each side, the top row shows across-participant ensemble averages of sagittal knee mechanical power for the stride before (S-1), during (S0), and after (S+1) the perturbation. Shaded regions represent ±1 standard deviation. Within each side, the bottom row shows sagittal knee mechanical work during the S-1 stride, and changes in mechanical works from steady state levels. Works and powers were normalized to participant body mass with no exoskeleton. Error bars represent ±1 standard error. * represents a significant main effect of stiffness with p<0.050.

Figure 33 - Exoskeleton effects on A) the ankle ipsilateral to the perturbation, and b) the ankle contralateral to the perturbation. For each side, the top row shows across-participant ensemble averages of sagittal ankle mechanical power for the stride before (S-1), during (S0), and after (S+1) the perturbation. Shaded regions represent ±1 standard deviation. Within each side, the bottom row shows sagittal ankle mechanical work during the S-1 stride, and changes in mechanical works from steady state levels. Works and powers were normalized to participant body mass with no exoskeleton. Error bars represent ±1 standard error. ** and * represents a significant main effect of stiffness with p<0.001 and p<0.050, respectively.

Figure 34 – Rectus femoris fascicle and MTU dynamics ensemble averaged across participants for the stride before (S-1), stride of (S0), and stride after (S+1) the perturbation. Shaded regions represent ±1 standard deviation. Standard deviations were omitted from fascicle and MTU lengths for clarity. RF fascicle forces are normalized to the mass of each participant not wearing the exoskeleton.
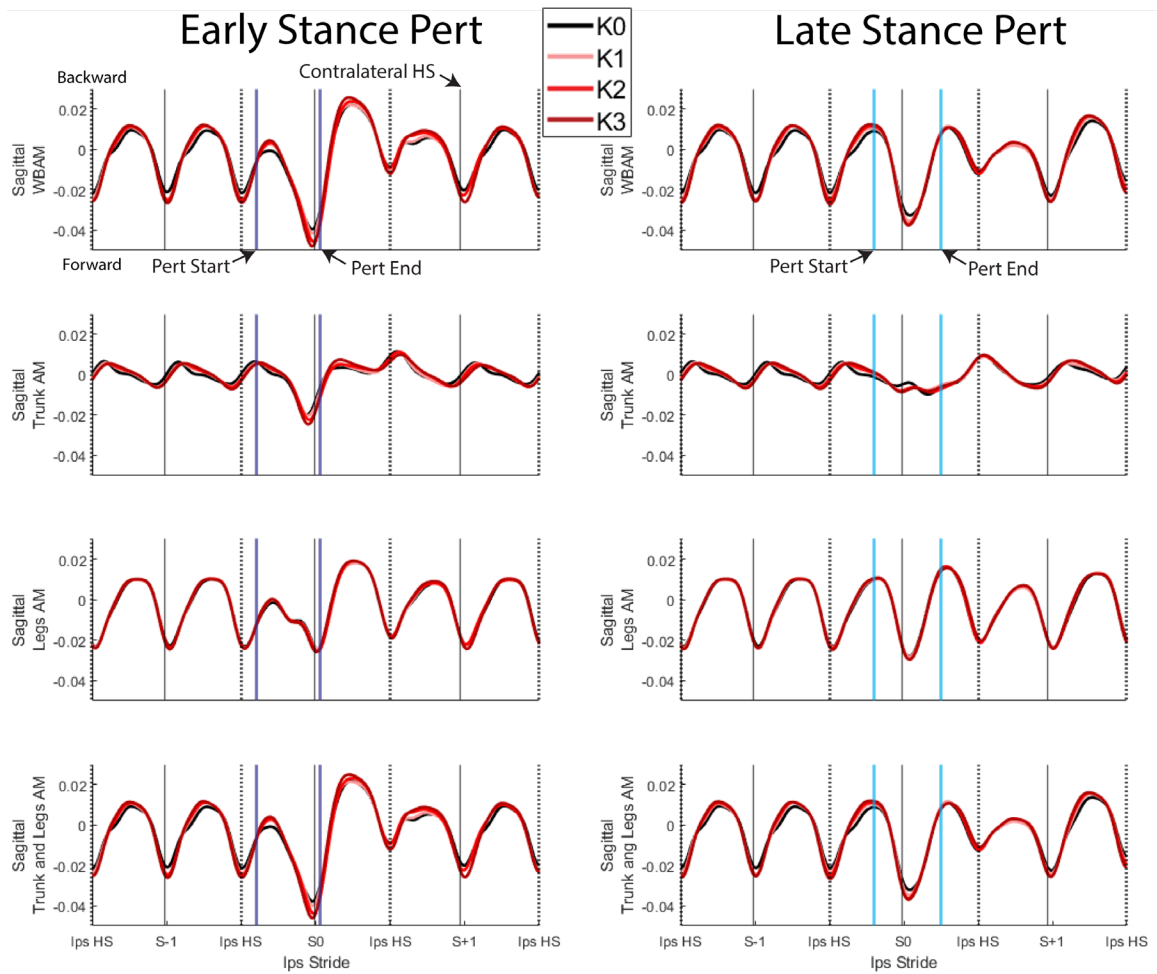
Figure 35 – Breakdown of trunk and leg angular momentum (AM) contributions in the sagittal plane. All angular momenta were normalized to mass of each participant not wearing the exoskeleton. Standard deviations are omitted for clarity. Positive angular momentum is defined as backward pitching.
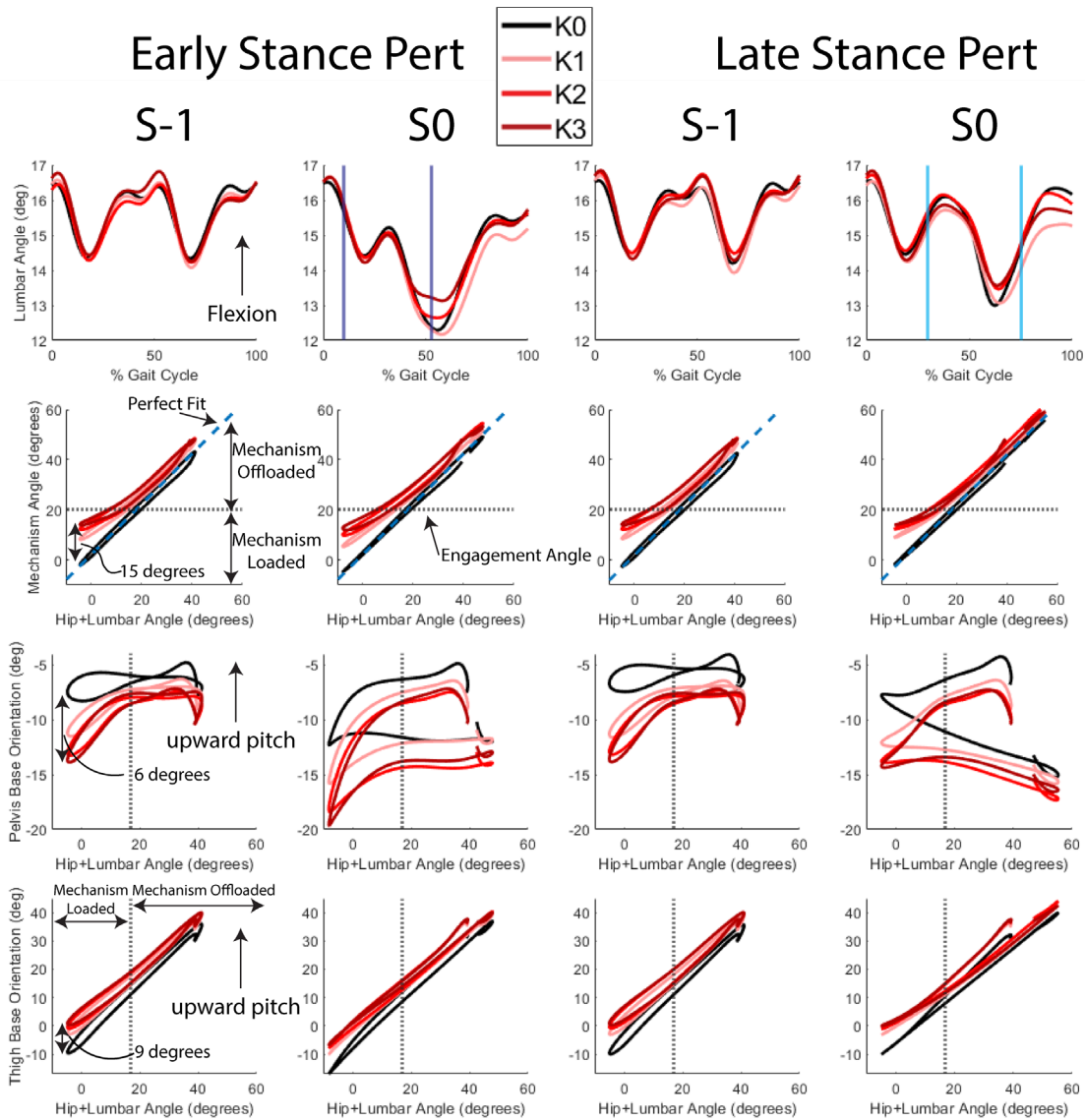
Figure 36 – Assessment of exoskeleton fit. Across-participant ensemble averages of (top row) lumbar angle, (second row) mechanism vs. combined lumbar and hip angle, (third row) sagittal orientation of the pelvis section of the mechanism, and (fourth row) sagittal orientation of the thigh section of the mechanism. Standard deviations are omitted for clarity.

CHAPTER 6.   CONCLUSION

The specific aims of this dissertation were two-fold: 1) to determine the multi-scale responses of proximal leg muscles and joints to transient mechanical energy demands and 2) to evaluate the influence of an elastic hip exoskeleton on stability during walking. To fulfill these aims, I conducted 3 separate studies in healthy, uninjured individuals, the findings of which were separated into 4 chapters.

Chapter 2, a publication in the Journal of Biomechanics (Golyski et al., 2021), describes the development and effects on spatiotemporal stability of a custom treadmill perturbation application that was developed for use on a CAREN (Motek, Netherlands) instrumented treadmill. This application allows for targeting of rapid, transient, unilateral belt accelerations at different periods within the gait cycle based on real-time kinematic data. We found that perturbations delivered close to the end of stance generally resulted in larger step widths and step lengths during the perturbed step, and shorter step lengths and wider widths on the first recovery step. These results indicate the importance of the mechanical state of the body in dictating the effect a perturbation on stability during walking. I anticipate these findings will spur future work investigating how different types of perturbation (e.g., pelvis pulls, audiovisual perturbations, platform movements) may interact with different timings to influence stability. Such investigations may clarify how the central nervous system weighs sensory inputs differently based on the mechanical state of the body to determine stabilizing responses.

Chapter 3, a publication in the Journal of the Royal Society Interface (Golyski and Sawicki, 2022), leverages the treadmill application to frame a destabilizing perturbation as

a mechanical work demand, allowing for a multi-scale energy accounting analysis to assess how perturbation energy is mediated. Specifically, by delivering a treadmill belt acceleration in either early or late stance, we hypothesized we could elicit a demand of net positive or net negative work by the perturbed leg over the perturbed gait cycle, and that the work demand at the ankle would best reflect the work demand at the leg. Contrary to our first hypothesis, we found that early/late stance perturbations elicited net positive/net zero work on average across participants, caused by an altered transfer of energy to the center of mass and a shift in force because of the perturbation. At the joint level, regression analyses revealed that changes in ankle work did best reflect changes in perturbed leg work, but also that changes in knee work best reflected changes in leg work on the contralateral leg. These findings 1) set the groundwork for the use of mechanical energetics to investigate stabilizing responses across different levels of musculoskeletal description, and 2) indicate a larger role of proximal joint and muscles, particularly at the knee, in mediating perturbation responses than previously thought.

Chapter 4, which I anticipate submitting as a publication to the Journal of Experimental Biology, extends the perturbation energetics paradigm down to the level of a single muscle, the rectus femoris. Using electromyography, B-mode ultrasound images tracked using a custom tracking application, and a Hill-type model of fascicle force, the mechanical powers and works of the rectus femoris fascicles and the muscle-tendon unit were estimated and related to the mechanical energetics at the joint and leg levels. We hypothesized 1) the perturbation would elicit negative power/work at the rectus femoris level on the perturbed leg due to active lengthening, 2) the energetic demand on the rectus femoris would reflect that of the contralateral knee and leg, and 3) the rectus femoris would facilitate the transfer

of mechanical work from the hip to the knee joint. Our first hypothesis was supported, with both perturbation timings resulting in increased negative power and work on the perturbed leg and stride. Our second hypothesis was not supported, with the mechanical works of the rectus femoris muscle-tendon unit and fascicles better reflecting the role of the contralateral hip than the knee or leg. Our third hypothesis was partially supported, with different perturbation timings altering the direction of energy transfer between the hip and the knee through the rectus femoris. Overall, this chapter: 1) contributes a novel semi-automated tracking application for measuring the dynamics of proximal leg muscles during locomotion, 2) indicates that changes in both lengths and activations contribute to altered mechanical energetics of proximal muscles during perturbed walking, and 3) demonstrates that the biarticular rectus femoris, in concert with the gastrocnemius, may facilitates the transfer of energy across the leg to fulfill leg-level demands. I anticipate this chapter will serve as the impetus for improved neuromuscular simulations informed by *in-vivo* measurements, in addition to investigations of the contributions of proximal leg muscles to proprioception and metabolic energy expenditure, particularly in concert with more sophisticated models of muscle force.

Chapter 5, which I anticipate submitting to the Journal of Biomechanics, further extends the perturbation energetics paradigm to include the influence of a passive hip exoskeleton. This chapter sought to link the multi-scale mechanical energetic and stability effects of an exoskeleton, the central idea being that a passive exoskeleton may alter whole-body energetics by altering the local energetics of biological joints and muscles. The technical developments specific to this chapter were 1) the semiautomated tracking application from Chapter 4 was supplemented with a deep learning approach to

aponeurosis detection to fully automate rectus femoris fascicle length measurements based on B-mode ultrasound images, and 2) a custom torsional passive hip exoskeleton (TPHE) was designed, manufactured, and characterized to provide passive hip flexion assistance while being able to image the rectus femoris. The hypotheses for this study were that 1) the exoskeleton would improve stability during a perturbation by lowering the range of sagittal whole-body angular momentum (WBAM) and decreasing the whole-body energetic demand of the perturbation (i.e., there would be a shift toward net zero work over the perturbed and first recovery strides), and 2) the exoskeleton would shift the net mechanical work of the hip and rectus femoris to oppose the energetic demand of the perturbation. Our hypotheses were not supported, with the TPHE leading to an increased WBAM range during steady state walking, higher TPHE stiffnesses maintaining this increased range during the perturbation, and there being little effect of the exoskeleton on mechanical energetics on any level of description. The findings from this study 1) point to a fundamental disconnect between mechanical energetic and WBAM-based definitions of stability, with a passive hip exoskeleton having potentially deleterious effects on stability from a WBAM perspective, but not a mechanical energetics perspective, 2) indicate that the small mechanical energetic alterations at the level of joints and muscles caused by low levels of hip exoskeleton assistance (<0.1 Nm/kg peak torque) may be "washed out" during perturbations but are measurable during steady state walking, and 3) hip-flexion assisting exoskeletons mounted at the torso may cause larger WBAM fluctuations during walking due to alterations in trunk kinematics caused by the assistance profile. I anticipate future studies will 1) seek to confirm these findings using devices with more rigid interfaces to facilitate higher torques being transmitted to the user from the device, and 2) will

investigate how explicitly injecting or extracting energy with an exoskeleton may alter stability from a mechanical energetics perspective.

In addition to the individual implications for each chapter, there are 3 broad questions which stem from this overall dissertation. First, how can a perturbation energetics paradigm best be extended to the level of muscle? Because *in-vivo* approaches in humans require use of inaccurate models of muscle force, a high-fidelity extension of this approach likely requires a combination of *in-situ* and *in-vivo* experiments in animals where forces and lengths can be measured with implanted instrumentation, which in turn can be used to develop improved models of muscle force generation that can capture the nuances of force produced during similar perturbations in humans. Further, advances in human *in-vivo* force measurement, such as shear-wave tensiometry (Martin et al., 2018), may provide approaches that circumvent the need for models of force generation. The second broad question is: how do our findings translate to different types of perturbations? The studies performed in this dissertation were limited to transient unilateral belt accelerations, which represent a very limited subset of the types of perturbations during locomotion in daily life. Thus, additional studies should explore how different directions, magnitudes, timings, and locations (e.g., center of mass pulls) of perturbations may alter multi-scale mechanical energetics. Fortunately, a mechanical energetic approach is not limited to unilateral treadmill perturbations – if the average net demand on the person is known during a steady state stride, the energetic demand of a perturbation can be calculated from a combination of kinematic and/or kinetic measurements informed by free-body diagrams. The third broad question is how the findings of this dissertation may change in different patient populations, since these studies were performed on healthy, uninjured young adults at a

low risk of falls. The energetic relationships between different levels of musculoskeletal description are likely altered in populations at a higher risk of falls due to differences in coordination and strength. One specific population of interest in relation to this mechanical energetics-based paradigm is individuals with lower limb amputation. During a perturbed stride, the ankle strongly reflected the demand of the perturbation on the perturbed side. However, in individuals with a transtibial amputation using a passive elastic ankle-foot prosthesis, the ankle can no longer dissipate or generate energy over a stride. Thus, future studies should investigate how the intact joints may alter their reflection of the demands of perturbations, and whether active devices with bio-inspired controllers may normalize the flows of energy during a perturbation and reduce the risk of falls.

REFERENCES

Abbott, E. M., Nezwek, T., Schmitt, D. and Sawicki, G. S. (2019). Hurry Up and Get Out of the Way! Exploring the Limits of Muscle-Based Latch Systems for Power Amplification. *Integrative and Comparative Biology* **59**, 1546–1558.

Ackland, D. C., Lin, Y. C. and Pandy, M. G. (2012). Sensitivity of model predictions of muscle function to changes in moment arms and muscle-tendon properties: A Monte-Carlo analysis. *Journal of Biomechanics* **45**, 1463–1471.

Afschrift, M., van Deursen, R., de Groote, F. and Jonkers, I. (2019). Increased use of stepping strategy in response to medio-lateral perturbations in the elderly relates to altered reactive tibialis anterior activity. *Gait and Posture* **68**, 575–582.

Alexander, N., Strutzenberger, G., Ameshofer, L. M. and Schwameder, H. (2017). Lower limb joint work and joint work contribution during downhill and uphill walking at different inclinations. *Journal of Biomechanics* **61**, 75–80.

Antonellis, P., Galle, S., de Clercq, D. and Malcolm, P. (2018). Altering gait variability with an ankle exoskeleton. *PLoS ONE* **13**, 1–17.

Arampatzis, A., de Monte, G., Karamanidis, K., Morey-Klapsing, G., Stafilidis, S. and Brüggemann, G. P. (2006). Influence of the muscle-tendon unit's mechanical and morphological properties on running economy. *Journal of Experimental Biology* **209**, 3345–3357.

Arnold, E. M. and Delp, S. L. (2011). Fibre operating lengths of human lower limb muscles during walking. *Philosophical Transactions of the Royal Society B: Biological Sciences* **366**, 1530–1539.

Arnold, E. M., Ward, S. R., Lieber, R. L. and Delp, S. L. (2010). A Model of the Lower Limb for Analysis of Human Movement. *Annals of Biomedical Engineering* **38**, 269–279.

Arnold, E. M., Hamner, S. R., Seth, A., Millard, M. and Delp, S. L. (2013). How muscle fiber lengths and velocities affect muscle force generation as humans walk and run at different speeds. *Journal of Experimental Biology* **216**, 2150–2160.

Azizi, E. and Roberts, T. J. (2010). Muscle performance during frog jumping: Influence of elasticity on muscle operating lengths. *Proceedings of the Royal Society B: Biological Sciences* **277**, 1523–1530.

Banala, S. K., Kim, S. H., Agrawal, S. K. and Scholz, J. P. (2008). Robot assisted gait training with active leg exoskeleton (ALEX). *Proceedings of the 2nd Biennial IEEE/RAS-EMBS International Conference on Biomedical Robotics and Biomechatronics, BioRob 2008* **17**, 653–658.

Bauby, C. E. and Kuo, A. D. (2000). Active control of lateral balance in human walking. *Journal of Biomechanics* **33**, 1433–1440.

Bell, J. L., Collins, J. W., Wolf, L., Gronqvist, R., Chiou, S., Chang, W. R., Sorock, G., Courtney, T., Lombardi, D. and Evanoff, B. (2008). Evaluation of a comprehensive slip, trip and fall prevention programme for hospital employees. *Ergonomics* **51**, 1906–1925.

Beltran, E. J., Dingwell, J. B. and Wilken, J. M. (2014). Margins of stability in young adults with traumatic transtibial amputation walking in destabilizing environments. *Journal of Biomechanics* **47**, 1138–1143.

Berg, W. P., Alessio, H. M., Mills, E. M. and Tong, C. (1997). Circumstances and consequences of falls in independent community-dwelling older adults. *Age and Ageing* **26**, 261–268.

Berger, W., Dietz, V. and Quintern, J. (1984). Corrective reactions to stumbling in man: neuronal co-ordination of bilateral leg muscle activity during gait. *The Journal of Physiology* **357**, 109–125.

Biewener, A. A. (2016). Locomotion as an emergent property of muscle contractile dynamics. *Journal of Experimental Biology* **219**, 285–294.

Biewener, A. A. and Roberts, T. J. (2000). Muscle and tendon contributions to force, work, and elastic energy savings: a comparative perspective. *Exerc Sport Sci Rev* **28**, 99–107.

Bjerk, M., Brovold, T., Skelton, D. A. and Bergland, A. (2018). Associations between health-related quality of life, physical function and fear of falling in older fallers receiving home care. *BMC Geriatrics* **18**, 1–8.

Blazevich, A. J., Gill, N. D. and Zhou, S. (2006). Intra- and intermuscular variation in human quadriceps femoris architecture assessed in vivo. *Journal of Anatomy* **209**, 289–310.

Blemker, S. S. and Delp, S. L. (2006). Rectus femoris and vastus intermedius fiber excursions predicted by three-dimensional muscle models. *Journal of Biomechanics* **39**, 1383–1391.

Blum, K. P., Lamotte D'Incamps, B., Zytnicki, D. and Ting, L. H. (2017). Force encoding in muscle spindles during stretch of passive muscle. *PLOS Computational Biology* **13**, e1005767.

Bobbert, M. F., Huijing, P. A. and van Ingen Schenau, G. J. (1986). A model of the human triceps surae muscle-tendon complex applied to jumping. *Journal of Biomechanics* **19**, 887–898.

Bohm, S., Marzilger, R., Mersmann, F., Santuz, A. and Arampatzis, A. (2018). Operating length and velocity of human vastus lateralis muscle during walking and running. *Scientific Reports* **8**, 1–10.

Bolsterlee, B., Veeger, H. E. J., van der Helm, F. C. T., Gandevia, S. C. and Herbert, R. D. (2015). Comparison of measurements of medial gastrocnemius architectural parameters from ultrasound and diffusion tensor images. *Journal of Biomechanics* **48**, 1133–1140.

Brennan, S. F., Cresswell, A. G., Farris, D. J. and Lichtwark, G. A. (2017). In vivo fascicle length measurements via B-mode ultrasound imaging with single vs dual transducer arrangements. *Journal of Biomechanics* **64**, 240–244.

Brown, I. E., Cheng, E. J. and Loeb, G. E. (1999). Measured and modeled properties of mammalian skeletal muscle. II. The effects of stimulus frequency on force-length and force-velocity relationships. *J Muscle Res Cell Motil* **20**, 627–43.

Bryan, G. M., Franks, P. W., Klein, S. C., Peuchen, R. J. and Collins, S. H. (2020). A hip–knee–ankle exoskeleton emulator for studying gait assistance. *International Journal of Robotics Research*.

Buchanan, T. S., Lloyd, D. G., Manal, K. and Besier, T. F. (2004). Neuromusculoskeletal modeling: estimation of muscle forces and joint moments and movements from measurements of neural command. *J Appl Biomech* **20**, 367–95.

Buczek, F. L., Kepple, T. M., Siegelt, K. L. and Stanhope, S. J. (1994). *TRANSLATIONAL AND ROTATIONAL JOINT POWER TERMS IN A SIX DEGREE-OF-FREEDOM MODEL OF THE NORMAL ANKLE COMPLEX.*

Burns, E. R., Stevens, J. A. and Lee, R. (2016). The direct costs of fatal and non-fatal falls among older adults — United States. *Journal of Safety Research* **58**, 99–103.

Cavagna, G. A. and Kaneko, M. (1977). Mechanical work and efficiency in level walking and running. *The Journal of Physiology* **268**, 467–481.

Centers for Disease Control and Prevention (CDC) and National Center for Health Statistics (NCHS) (2016). National Health and Nutrition Examination Survey Data. *National Health and Nutrition Examination Survey*.

Chen, W., Wu, S., Zhou, T. and Xiong, C. (2019). On the biological mechanics and energetics of the hip joint muscle-tendon system assisted by passive hip exoskeleton. *Bioinspiration and Biomimetics* **14**,.

Chiu, V. L., Raitor, M. and Collins, S. H. (2021). Design of a Hip Exoskeleton With Actuation in Frontal and Sagittal Planes. *IEEE Transactions on Medical Robotics and Bionics* **3**, 773–782.

Close, R. I. (1972). The relations between sarcomere length and characteristics of isometric twitch contractions of frog sartorius muscle. *The Journal of Physiology* **220**, 745–762.

Collins, S. H., Bruce Wiggin, M., Sawicki, G. S., Wiggin, M. B. and Sawicki, G. S. (2015). Reducing the energy cost of human walking using an unpowered exoskeleton. *Nature* **522**, 212–215.

Cronin, N. (2020). *Automated Analysis of Musculoskeletal Ultrasound Images Using Deep Learning*.

Daley, M. A. and Biewener, A. A. (2011). Leg muscles that mediate stability: Mechanics and control of two distal extensor muscles during obstacle negotiation in the guinea fowl. *Philosophical Transactions of the Royal Society B: Biological Sciences* **366**, 1580–1591.

Daley, M. A., Usherwood, J. R., Felix, G. and Biewener, A. A. (2006). Running over rough terrain: Guinea fowl maintain dynamic stability despite a large unexpected change in substrate height. *Journal of Experimental Biology* **209**, 171–187.

Daley, M. A., Felix, G. and Biewener, A. A. (2007). Running stability is enhanced by a proximo-distal gradient in joint neuromechanical control. *Journal of Experimental Biology* **210**, 383–394.

Daley, M. A., Voloshina, A. and Biewener, A. A. (2009). The role of intrinsic muscle mechanics in the neuromuscular control of stable running in the guinea fowl. *Journal of Physiology* **587**, 2693–2707.

de Groote, F., Allen, J. L. and Ting, L. H. (2017). Contribution of muscle short-range stiffness to initial changes in joint kinetics and kinematics during perturbations to standing balance: A simulation study. *Journal of Biomechanics* **55**, 71–77.

Debelle, H., Harkness-Armstrong, C., Hadwin, K., Maganaris, C. N. and O'Brien, T. D. (2020). Recovery From a Forward Falling Slip: Measurement of Dynamic Stability and Strength Requirements Using a Split-Belt Instrumented Treadmill. *Frontiers in Sports and Active Living* **2**, 1–13.

Delp, S. L., Anderson, F. C., Arnold, A. S., Loan, P., Habib, A., John, C. T., Guendelman, E. and Thelen, D. G. (2007). OpenSim: Open-source software to create and analyze dynamic simulations of movement. *IEEE Transactions on Biomedical Engineering* **54**, 1940–1950.

Dick, T. J. M., Biewener, A. A. and Wakeling, J. M. (2017). Comparison of human gastrocnemius forces predicted by Hill-type muscle models and estimated from ultrasound images. *Journal of Experimental Biology* **220**, 1643–1653.

Dick, T. J. M., Punith, L. K. and Sawicki, G. S. (2019). Humans falling in holes: Adaptations in lower-limb joint mechanics in response to a rapid change in substrate height during human hopping. *Journal of the Royal Society Interface* **16**,.

Dick, T. J. M., Clemente, C. J., Punith, L. K. and Sawicki, G. S. (2021). Series elasticity facilitates safe plantar flexor muscle-tendon shock absorption during perturbed human hopping. *Proceedings of the Royal Society B: Biological Sciences* **288**,.

Dietz, V., Horstmann, G. A. and Berger, W. (1989). Perturbations of Human Posture. *Journal of Motor Behavior* **21**, 357–372.

Donelan, J. M., Kram, R. and Kuo, A. D. (2002a). Mechanical work for step-to-step transitions is a major determinant of the metabolic cost of human walking. *Journal of Experimental Biology* **205**, 3717–3727.

Donelan, J. M., Kram, R. and Kuo, A. D. (2002b). Simultaneous positive and negative external mechanical work in human walking. *Journal of Biomechanics* **35**, 117–124.

Donelan, J. M., Shipman, D. W., Kram, R. and Kuo, A. D. (2004). Mechanical and metabolic requirements for active lateral stabilization in human walking. *Journal of Biomechanics* **37**, 827–835.

Donelan, J. M., Li, Q., Naing, V., Hoffer, J. A., Weber, D. J. and Kuo, A. D. (2008). Biomechanical energy harvesting: Generating electricity during walking with minimal user effort. *Science (1979)* **319**, 807–810.

Duncan, J. A., Kowalk, D. L. and Vaughan, C. L. (1997). Six degree of freedom joint power in stair climbing. *Gait & Posture* **5**, 204–210.

Emmens, A. R., van Asseldonk, E. H. F. and van der Kooij, H. (2018). Effects of a powered ankle-foot orthosis on perturbed standing balance. *Journal of NeuroEngineering and Rehabilitation* **15**,.

Eng, J. J., Winter, D. A. and Patla, A. E. (1994). Strategies for recovery from a trip in early and late swing during human walking. *Experimental Brain Research* **102**, 339–349.

Espy, D. D., Yang, F., Bhatt, T. and Pai, Y. C. (2010). Independent influence of gait speed and step length on stability and fall risk. *Gait and Posture* **32**, 378–382.

Farris, D. J. and Raiteri, B. J. (2017). Modulation of leg joint function to produce emulated acceleration during walking and running in humans. *Royal Society Open Science* **4**,.

Farris, D. J. and Sawicki, G. S. (2012). The mechanics and energetics of human walking and running: A joint level perspective. *Journal of the Royal Society Interface* **9**, 110–118.

Farris, D. J., Robertson, B. D. and Sawicki, G. S. (2013). Elastic ankle exoskeletons reduce soleus muscle force but not work in human hopping. *J Appl Physiol* **115**, 579–585.

Ferris, D. P. and Farley, C. T. (1997). Interaction of leg stiffness and surface stiffness during human hopping. *Journal of Applied Physiology* **82**, 15–22.

Ferris, D. P., Liang, K. and Farley, C. T. (1999). Runners adjust leg stiffness for their first step on a new running surface. *Journal of Biomechanics* **32**, 787–794.

Figura, F., Felici, F. and Macellari, V. (1986). Human locomotor adjustments during perturbed walking. *Human Movement Science* **5**, 313–332.

Frangi, A. F., Niessen, W. J., Vincken, K. L. and Viergever, M. A. (1998). Multiscale vessel enhancement filtering.pp. 130–137.

Gholizadeh, H., Hill, A. and Nantel, J. (2019). Effect of arm motion on postural stability when recovering from a slip perturbation. *Journal of Biomechanics* **95**,.

Gillis, G. B. and Biewener, A. A. (2002). Effects of surface grade on proximal hindlimb muscle strain and activation during rat locomotion. *Journal of Applied Physiology* **93**, 1731–1743.

Golyski, P. R. and Sawicki, G. S. (2022). Which lower limb joints compensate for destabilizing energy during walking in humans? *Journal of The Royal Society Interface* **19**,.

Golyski, P. R., Vazquez, E., Leestma, J. K. and Sawicki, G. S. (2021). Onset timing of treadmill belt perturbations influences stability during walking. *Journal of Biomechanics* 110800.

Grabiner, M. D., Koh, T. J., Lundin, T. M. and Jahnigen, D. W. (1993). *Kinematics of Recovery From a Stumble*.

Hamner, S. R., Seth, A. and Delp, S. L. (2010). Muscle contributions to propulsion and support during running. *Journal of Biomechanics* **43**, 2709–2716.

Handsfield, G. G., Meyer, C. H., Hart, J. M., Abel, M. F. and Blemker, S. S. (2014). Relationships of 35 lower limb muscles to height and body mass quantified using MRI. *Journal of Biomechanics* **47**, 631–638.

Hartholt, K. A., Lee, R., Burns, E. R. and van Beeck, E. F. (2019). Mortality From Falls Among US Adults Aged 75 Years or Older, 2000-2016. *JAMA* **321**, 2131.

Haufe, F. L., Wolf, P., Riener, R. and Grimmer, M. (2020). Biomechanical effects of passive hip springs during walking. *Journal of Biomechanics* **98**, 109432.

Heiden, T. L., Sanderson, D. J., Inglis, J. T. and Siegmund, G. P. (2006). Adaptations to normal human gait on potentially slippery surfaces: The effects of awareness and prior slip experience. *Gait and Posture* **24**, 237–246.

Herr, H. and Popovic, M. (2008). Angular momentum in human walking. *Journal of Experimental Biology* **211**, 467–481.

Hill, A. V. (1938). The heat of shortening and the dynamic constants of muscle. *Proceedings of the Royal Society of London. Series B - Biological Sciences* **126**, 136–195.

Hnat, S. K. and van den Bogert, A. J. (2014). Inertial compensation for belt acceleration in an instrumented treadmill. *Journal of Biomechanics* **47**, 3758–3761.

Hof, A. L. and Duysens, J. (2018). Responses of human ankle muscles to mediolateral balance perturbations during walking. *Human Movement Science* **57**, 69–82.

Hof, A. L., Gazendam, M. G. J. and Sinke, W. E. (2005). The condition for dynamic stability. *Journal of Biomechanics* **38**, 1–8.

Hof, A. L., Vermerris, S. M. and Gjaltema, W. A. (2010). Balance responses to lateral perturbations in human treadmill walking. *Journal of Experimental Biology* **213**, 2655–2664.

Holt, N. C. and Azizi, E. (2014). What drives activation-dependent shifts in the force-length curve? *Biology Letters* **10**, 20140651–20140651.

Honda, K., Sekiguchi, Y., Muraki, T. and Izumi, S. I. (2019). The differences in sagittal plane whole-body angular momentum during gait between patients with hemiparesis and healthy people. *Journal of Biomechanics* **86**, 204–209.

Hua, Y., Zhu, Y., Li, C., Zhao, J. and Zhu, Y. (2021). Assistance Control of Human-Exoskeleton Integrated System for Balance Recovery Augmentation in Sagittal Plane. *IEEE Transactions on Industrial Electronics* **0046**,.

Huang, T. W. P., Shorter, K. A., Adamczyk, P. G. and Kuo, A. D. (2015). Mechanical and energetic consequences of reduced ankle plantar-flexion in human walking. *Journal of Experimental Biology* **218**, 3541–3550.

Huijing, P. A. (1998). *Muscle, the motor of movement: properties in function, experiment and modelling.*

Iida, F., Rummel, J. and Seyfarth, A. (2008). Bipedal walking and running with spring-like biarticular muscles. *Journal of Biomechanics* **41**, 656–667.

Ilmane, N., Croteau, S. and Duclos, C. (2015). Quantifying dynamic and postural balance difficulty during gait perturbations using stabilizing/destabilizing forces. *Journal of Biomechanics* **48**, 441–448.

Jacobs, R., Bobbert, M. F. and van Ingen Schenau, G. J. (1996). Mechanical output from individual muscles during explosive leg extensions: The role of biarticular muscles. *Journal of Biomechanics* **29**, 513–523.

Johnson, M. A., Polgar, J., Weightman, D. and Appleton, D. (1973). Data on the distribution of fibre types in thirty-six human muscles. *Journal of the Neurological Sciences* **18**, 111–129.

Joshi, V. and Srinivasan, M. (2019). A controller for walking derived from how humans recover from perturbations. *Journal of the Royal Society Interface* **16**,.

Kagawa, T., Ohta, Y. and Uno, Y. (2011). Human Movement Science State-dependent corrective reactions for backward balance losses during human walking. **30**, 1210–1224.

Kim, M. and Collins, S. H. (2017). Once-Per-Step Control of Ankle Push-Off Work Improves Balance in a Three-Dimensional Simulation of Bipedal Walking. *IEEE Transactions on Robotics* **33**, 406–418.

King, S. T., Eveld, M. E., Martínez, A., Zelik, K. E. and Goldfarb, M. (2019). A novel system for introducing precisely-controlled, unanticipated gait perturbations for the study of stumble recovery. *Journal of NeuroEngineering and Rehabilitation* **16**, 1–17.

Knox, B. T. and Schmiedeler, J. P. (2009). A unidirectional series-elastic actuator design using a spiral torsion spring. *Journal of Mechanical Design, Transactions of the ASME* **131**, 1250011–1250015.

Konow, N. and Roberts, T. J. (2015). The series elastic shock absorber: Tendon elasticity modulates energy dissipation by muscle during burst deceleration. *Proceedings of the Royal Society B: Biological Sciences* **282**,.

Kuo, A. D. (2002). Energetics of actively powered locomotion using the simplest walking model. *Journal of Biomechanical Engineering* **124**, 113–120.

Kuo, A. D. and Donelan, J. M. (2010). Dynamic principles of gait and their clinical implications. *Phys Ther* **90**, 157–74.

Lai, A. K. M., Biewener, A. A. and Wakeling, J. M. (2019). Muscle-specific indices to characterise the functional behaviour of human lower-limb muscles during locomotion. *J Biomech* **89**, 134–138.

Lamers, E. P. and Zelik, K. E. (2021). Design, modeling, and demonstration of a new dual-mode back-assist exosuit with extension mechanism. *Wearable Technologies* **2**,.

Lavedán, A., Viladrosa, M., Jürschik, P., Botigué, T., Nuín, C., Masot, O. and Lavedán, R. (2018). Fear of falling in community-dwelling older adults: A cause of falls, a consequence, or both? *PLoS ONE* **13**, 1–14.

Lay, A. N., Hass, C. J., Richard Nichols, T. and Gregor, R. J. (2007). The effects of sloped surfaces on locomotion: An electromyographic analysis. *Journal of Biomechanics* **40**, 1276–1285.

Lee, H. D. and Herzog, W. (2003). Force depression following muscle shortening of voluntarily activated and electrically stimulated human adductor pollicis. *Journal of Physiology* **551**, 993–1003.

Lee, S. S. M., Arnold, A. S., Miara, M. de B., Biewener, A. A. and Wakeling, J. M. (2013). Accuracy of gastrocnemius muscles forces in walking and running goats predicted by one-element and two-element Hill-type models. *Journal of Biomechanics* **46**, 2288–2295.

Lee, B. C., Kim, C. S. and Seo, K. H. (2019). The Body's Compensatory Responses to Unpredictable Trip and Slip Perturbations Induced by a Programmable Split-Belt Treadmill. *IEEE Transactions on Neural Systems and Rehabilitation Engineering* **27**, 1389–1396.

Leitner, C., Jarolim, R., Englmair, B., Kruse, A., Hernandez, K. A. L., Konrad, A., Su, E., Schrottner, J., Kelly, L. A., Lichtwark, G. A., et al. (2021). A Human-Centered Machine-Learning Approach for Muscle-Tendon Junction Tracking in Ultrasound Images. *IEEE Transactions on Biomedical Engineering*.

Lenzi, T., Carrozza, M. C. and Agrawal, S. K. (2013). Powered hip exoskeletons can reduce the user's hip and ankle muscle activations during walking. *IEEE Transactions on Neural Systems and Rehabilitation Engineering* **21**, 938–948.

Lewis, C. L. and Ferris, D. P. (2011). Invariant hip moment pattern while walking with a robotic hip exoskeleton. *Journal of Biomechanics* **44**, 789–793.

Li, J. and Huang, H. J. (2021). Small Directional Treadmill Perturbations Induce Differential Gait Stability Adaptation. *Journal of Neurophysiology*.

Li, J. M., Molinaro, D. D., King, A. S., Mazumdar, A. and Young, A. J. (2021). Design and Validation of a Cable-Driven Asymmetric Back Exosuit; Design and Validation of a Cable-Driven Asymmetric Back Exosuit.

Libby, T., Chukwueke, C. and Sponberg, S. (2020). History-dependent perturbation response in limb muscle. *Journal of Experimental Biology* **223**,.

Lieber, R. L. and Friden, J. (1993). Muscle damage is not a function of muscle force but active muscle strain. *Journal of Applied Physiology* **74**, 520–526.

Lin, C. C. K. and Crago, P. E. (2002a). Neural and mechanical contributions to the stretch reflex: A model synthesis. *Annals of Biomedical Engineering* **30**, 54–67.

Lin, C. C. K. and Crago, P. E. (2002b). Structural model of the muscle spindle. *Annals of Biomedical Engineering* **30**, 68–83.

Liu, C. and Finley, J. M. (2020). Asymmetric gait patterns alter the reactive control of intersegmental coordination patterns in the sagittal plane during walking. *PLOS ONE* **15**, e0224187.

Liu, C., de Macedo, L. and Finley, J. M. (2018). Conservation of reactive stabilization strategies in the presence of step length asymmetries during walking. *Frontiers in Human Neuroscience* **12**,.

Lurie, J. D., Zagaria, A. B., Pidgeon, D. M., Forman, J. L. and Spratt, K. F. (2013). Pilot comparative effectiveness study of surface perturbation treadmill training to prevent falls in older adults. *BMC Geriatrics* **13**,.

Madehkhaksar, F., Klenk, J., Sczuka, K., Gordt, K., Melzer, I. and Schwenk, M. (2018). The effects of unexpected mechanical perturbations during treadmill walking on spatiotemporal gait parameters, and the dynamic stability measures by which to quantify postural response. *PLoS ONE* **13**, 1–15.

Martin, J. A., Brandon, S. C. E., Keuler, E. M., Hermus, J. R., Ehlers, A. C., Segalman, D. J., Allen, M. S. and Thelen, D. G. (2018). Gauging force by tapping tendons. *Nature Communications* **9**,.

Marzilger, R., Legerlotz, K., Panteli, C., Bohm, S. and Arampatzis, A. (2018). Reliability of a semi-automated algorithm for the vastus lateralis muscle architecture measurement based on ultrasound images. *European Journal of Applied Physiology* **118**, 291–301.

McAndrew Young, P. M., Wilken, J. M. and Dingwell, J. B. (2012). Dynamic margins of stability during human walking in destabilizing environments. *Journal of Biomechanics* **45**, 1053–1059.

McGowan, C. P., Baudinette, R. v. and Biewener, A. A. (2007). Modulation of proximal muscle function during level versus incline hopping in tammar wallabies (Macropus eugenii). *Journal of Experimental Biology* **210**, 1255–1265.

Millard, M., Uchida, T., Seth, A. and Delp, S. L. (2013). Flexing Computational Muscle: Modeling and Simulation of Musculotendon Dynamics. *Journal of Biomechanical Engineering* **135**,.

Monaco, V., Tropea, P., Aprigliano, F., Martelli, D., Parri, A., Cortese, M., Molino-Lova, R., Vitiello, N. and Micera, S. (2017). An ecologically-controlled exoskeleton can improve balance recovery after slippage. *Scientific Reports* **7**,.

Montgomery, J. R. and Grabowski, A. M. (2018). The contributions of ankle, knee and hip joint work to individual leg work change during uphill and downhill walking over a range of speeds. *Royal Society Open Science* **5**, 180550.

Moore, J. K., Hnat, S. K. and van den Bogert, A. J. (2015). An elaborate data set on human gait and the effect of mechanical perturbations. *PeerJ* **2015**,.

Moreland, B., Kakara, R. and Henry, A. (2020). Trends in Nonfatal Falls and Fall-Related Injuries Among Adults Aged ≥65 Years — United States, 2012–2018. *MMWR. Morbidity and Mortality Weekly Report* **69**, 875–881.

Nagano, H., Sparrow, W. A. and Begg, R. K. (2013). Biomechanical characteristics of slipping during unconstrained walking, turning, gait initiation and termination. *Ergonomics* **56**, 1038–1048.

Nakazawa, K., Kawashima, N., Akai, M. and Yano, H. (2004). On the reflex coactivation of ankle flexor and extensor muscles induced by a sudden drop of support surface during walking in humans. *J Appl Physiol* **96**, 604–611.

Nasiri, R., Ahmadi, A. and Ahmadabadi, M. N. (2018). Reducing the energy cost of human running using an unpowered exoskeleton. *IEEE Transactions on Neural Systems and Rehabilitation Engineering* **26**, 2026–2032.

Noorkoiv, M., Stavnsbo, A., Aagaard, P. and Blazevich, A. J. (2010). In vivo assessment of muscle fascicle length by extended field-of-view ultrasonography. *Journal of Applied Physiology* **109**, 1974–1979.

Nott, C. R., Neptune, R. R. and Kautz, S. A. (2014). Relationships between frontal-plane angular momentum and clinical balance measures during post-stroke hemiparetic walking. *Gait and Posture* **39**, 129–134.

Nuckols, R. W., Dick, T. J. M., Beck, O. N. and Sawicki, G. S. (2020a). Ultrasound imaging links soleus muscle neuromechanics and energetics during human walking with elastic ankle exoskeletons. *Scientific Reports* **10**, 1–15.

Nuckols, R. W., Takahashi, K. Z., Farris, D. J., Mizrachi, S., Riemer, R. and Sawicki, G. S. (2020b). Mechanics of walking and running up and downhill: A joint-level perspective to guide design of lower-limb exoskeletons. *PLoS ONE* **15**, 1–20.

Orendurff, M. S., Segal, A. D., Klute, G. K., Berge, J. S., Rohr, E. S. and Kadel, N. J. (2004). The effect of walking speed on center of mass displacement. *Journal of Rehabilitation Research and Development* **41**, 829–834.

Ortega, J. D. and Farley, C. T. (2007). Individual limb work does not explain the greater metabolic cost of walking in elderly adults. *Journal of Applied Physiology* **102**, 2266–2273.

Otten, E. (1987). A myocybernetic model of the jaw system of the rat. *Journal of Neuroscience Methods* **21**, 287–302.

Panizzolo, F. A., Lee, S., Miyatake, T., Rossi, D. M., Siviy, C., Speeckaert, J., Galiana, I. and Walsh, C. J. (2017). Lower limb biomechanical analysis during an unanticipated step on a bump reveals specific adaptations of walking on uneven terrains. *Journal of Experimental Biology* **220**, 4169–4176.

Panizzolo, F. A., Bolgiani, C., di Liddo, L., Annese, E. and Marcolin, G. (2019). Reducing the energy cost of walking in older adults using a passive hip flexion device. *Journal of NeuroEngineering and Rehabilitation* **16**, 1–9.

Panizzolo, F. A., Cimino, S., Pettenello, E., Belfiore, A., Petrone, N. and Marcolin, G. (2021). Effect of a passive hip exoskeleton on walking distance in neurological patients. *Assistive Technology* **0**,.

Pataky, T. C., Vanrenterghem, J. and Robinson, M. A. (2015). Zero- vs. one-dimensional, parametric vs. non-parametric, and confidence interval vs. hypothesis testing procedures in one-dimensional biomechanical trajectory analysis. *Journal of Biomechanics* **48**, 1277–1285.

Patton, J., Brown, D. A., Peshkin, M., Santos-Munné, J. J., Makhlin, A., Lewis, E., Colgate, E. J. and Schwandt, D. (2008). KineAssist: Design and Development of a Robotic Overground Gait and Balance Therapy Device. *Topics in Stroke Rehabilitation* **15**, 131–139.

Perreault, E. J., Heckman, C. J. and Sandercock, T. G. (2003). Hill muscle model errors during movement are greatest within the physiologically relevant range of motor unit firing rates. *Journal of Biomechanics* **36**, 211–218.

Pijnappels, M., Bobbert, M. F. and van Dieën, J. H. (2004). Contribution of the support limb in control of angular momentum after tripping. *Journal of Biomechanics* **37**, 1811–1818.

Pizzolato, C., Lloyd, D. G., Sartori, M., Ceseracciu, E., Besier, T. F., Fregly, B. J. and Reggiani, M. (2015). CEINMS: A toolbox to investigate the influence of different neural control solutions on the prediction of muscle excitation and joint moments during dynamic motor tasks. *J Biomech* **48**, 3929–36.

Popovic, M., Hofmann, A. and Herr, H. (2004). Angular momentum regulation during human walking: Biomechanics and control. *Proceedings - IEEE International Conference on Robotics and Automation* **2004**, 2405–2411.

Prilutsky, B. I. and Zatsiorsky, V. M. (1994). Tendon action of two-joint muscles: Transfer of mechanical energy between joints during jumping, landing, and running. *Journal of Biomechanics* **27**, 25–34.

Qiao, M. and Jindrich, D. L. (2016). Leg joint function during walking acceleration and deceleration. *Journal of Biomechanics* **49**, 66–72.

Rabago, C. A., Dingwell, J. B. and Wilken, J. M. (2015). Reliability and minimum detectable change of temporal-spatial, kinematic, and dynamic stability measures during perturbed gait. *PLoS ONE* **10**, 1–22.

Rajagopal, A., Dembia, C. L., DeMers, M. S., Delp, D. D., Hicks, J. L. and Delp, S. L. (2016). Full-Body Musculoskeletal Model for Muscle-Driven Simulation of Human Gait. *IEEE Transactions on Biomedical Engineering* **63**, 2068–2079.

Rankin, B. L., Buffo, S. K. and Dean, J. C. (2014). A neuromechanical strategy for mediolateral foot placement in walking humans. *Journal of Neurophysiology* **112**, 374–383.

Ringhof, S., Patzer, I., Beil, J., Asfour, T. and Stein, T. (2019). Does a Passive Unilateral Lower Limb Exoskeleton Affect Human Static and Dynamic Balance Control? *Frontiers in Sports and Active Living* **1**, 1–10.

Roberts, T. J. and Belliveau, R. A. (2005). Sources of mechanical power for uphill running in humans. *Journal of Experimental Biology* **208**, 1963–1970.

Roden-Reynolds, D. C., Walker, M. H., Wasserman, C. R. and Dean, J. C. (2015). Hip proprioceptive feedback influences the control of mediolateral stability during human walking. *Journal of Neurophysiology* **114**, 2220–2229.

Roeles, S., Rowe, P. J., Bruijn, S. M., Childs, C. R., Tarfali, G. D., Steenbrink, F. and Pijnappels, M. (2018). Gait stability in response to platform, belt, and sensory perturbations in young and older adults. *Medical and Biological Engineering and Computing* **56**, 2325–2335.

Roy, R. R., Meadows, I. D., Baldwin, K. M. and Edgerton, V. R. (1982). Functional significance of compensatory overloaded rat fast muscle. *Journal of Applied Physiology* **52**, 473–478.

Ryan, D. S., Stutzig, N., Siebert, T. and Wakeling, J. M. (2019). Passive and dynamic muscle architecture during transverse loading for gastrocnemius medialis in man. *Journal of Biomechanics* **86**, 160–166.

Sánchez, N., Simha, S. N., Donelan, J. M. and Finley, J. M. (2019). Taking advantage of external mechanical work to reduce metabolic cost: the mechanics and energetics of split-belt treadmill walking. *Journal of Physiology* **597**, 4053–4068.

Sandercock, T. G. and Heckman, C. J. (1997). Force From Cat Soleus Muscle During Imposed Locomotor-Like Movements: Experimental Data Versus Hill-Type Model Predictions. *Journal of Neurophysiology* **77**, 1538–1552.

Sawicki, G. S., Robertson, B. D., Azizi, E. and Roberts, T. J. (2015). Timing matters: Tuning the mechanics of a muscle-tendon unit by adjusting stimulation phase during cyclic contractions. *Journal of Experimental Biology* **218**, 3150–3159.

Sawicki, G. S., Beck, O. N., Kang, I. and Young, A. J. (2020). The exoskeleton expansion: improving walking and running economy. *Journal of NeuroEngineering and Rehabilitation* **17**, 25.

Schache, A. G., Lai, A. K. M., Brown, N. A. T., Crossley, K. M. and Pandy, M. G. (2019). Lower-limb joint mechanics during maximum acceleration sprinting. *Journal of Experimental Biology* **222**,.

Schiffman, J. M., Gregorczyk, K. N., Bensel, C. K., Hasselquist, L. and Obusek, J. P. (2008). The effects of a lower body exoskeleton load carriage assistive device on limits of stability and postural sway. *Ergonomics* **51**, 1515–1529.

Schillings, A. M., van Wezel, B. M. H., Mulder, T. and Duysens, J. (2000). Muscular responses and movement strategies during stumbling over obstacles. *Journal of Neurophysiology* **83**, 2093–2102.

Selgrade, B. P., Thajchayapong, M., Lee, G. E., Toney, M. E. and Chang, Y. H. (2017). Changes in mechanical work during neural adaptation to asymmetric locomotion. *Journal of Experimental Biology* **220**, 2993–3000.

Seo, K., Lee, J., Lee, Y., Ha, T. and Shim, Y. (2016). Fully autonomous hip exoskeleton saves metabolic cost of walking. In *2016 IEEE International Conference on Robotics and Automation (ICRA)*, pp. 4628–4635. IEEE.

Shamaei, K., Sawicki, G. S. and Dollar, A. M. (2013). Estimation of quasi-stiffness of the human hip in the stance phase of walking. *PLoS ONE* **8**,.

Shepertycky, M., Burton, S., Dickson, A., Liu, Y.-F. and Li, Q. *Removing energy with an exoskeleton reduces the metabolic cost of walking*.

Sherrington, C., Fairhall, N. J., Wallbank, G. K., Tiedemann, A., Michaleff, Z. A., Howard, K., Clemson, L., Hopewell, S. and Lamb, S. E. (2019). Exercise for preventing falls in older people living in the community. *Cochrane Database of Systematic Reviews* **2019**,.

Shinya, M., Fujii, S. and Oda, S. (2009). Corrective postural responses evoked by completely unexpected loss of ground support during human walking. *Gait and Posture* **29**, 483–487.

Shue, G.-H. and Crago, P. E. (1998). *Muscle-Tendon Model with Length History-Dependent Activation-Velocity Coupling*.

Silverman, A. K. and Neptune, R. R. (2011). Differences in whole-body angular momentum between below-knee amputees and non-amputees across walking speeds. *Journal of Biomechanics* **44**, 379–385.

Sloot, L. H., van den Noort, J. C., van der Krogt, M. M., Bruijn, S. M. and Harlaar, J. (2015). Can treadmill perturbations evoke stretch reflexes in the calf muscles? *PLoS ONE* **10**,.

Spector, S. A., Gardiner, P. F., Zernicke, R. F., Roy, R. R. and Edgerton, V. R. (1980). *Muscle Architecture and Force-Velocity Characteristics of Cat Soleus and Medial Gastrocnemius: Implications for Motor Control.*

Statistical Parametric Mapping (2007). Elsevier.

Sterling, D. A., O'Connor, J. A. and Bonadies, J. (2001). Geriatric Falls: Injury Severity Is High and Disproportionate to Mechanism. *The Journal of Trauma: Injury, Infection, and Critical Care* **50**, 116–119.

Süptitz, F., Karamanidis, K., Catalá, M. M. and Brüggemann, G. P. (2012). Symmetry and reproducibility of the components of dynamic stability in young adults at different walking velocities on the treadmill. *Journal of Electromyography and Kinesiology* **22**, 301–307.

Takahashi, K. Z., Kepple, T. M. and Stanhope, S. J. (2012). A unified deformable (UD) segment model for quantifying total power of anatomical and prosthetic below-knee structures during stance in gait. *Journal of Biomechanics* **45**, 2662–2667.

Talbot, L. A., Musiol, R. J., Witham, E. K. and Metter, E. J. (2005). Falls in young, middle-aged and older community dwelling adults: Perceived cause, environmental factors and injury. *BMC Public Health* **5**, 1–9.

Tang, P. F. and Woollacott, M. H. (1999). Phase-dependent modulation of proximal and distal postural responses to slips in young and older adults. *Journals of Gerontology - Series A Biological Sciences and Medical Sciences* **54**,.

Tang, P. F., Woollacott, M. H. and Chong, R. K. Y. (1998). Control of reactive balance adjustments in perturbed human walking: Roles of proximal and distal postural muscle activity. *Experimental Brain Research* **119**, 141–152.

Tant, G. R., Raitor, M. and Collins, S. H. (2020). Bump'em: An Open-Source, Bump-Emulation System for Studying Human Balance and Gait. In *Proceedings - IEEE International Conference on Robotics and Automation*, pp. 9093–9099. IEEE.

Tilley, A. and Henry Dreyfuss Associates (2002). *The Measure of Man & Woman Revised Edition: Human Factors in Design.*

Umberger, B. R., Gerritsen, K. G. M. and Martin, P. E. (2003). A model of human muscle energy expenditure. *Comput Methods Biomech Biomed Engin* **6**, 99–111.

US Bureau of Labor Statistics (2021). Injuries, Illnesses, and Fatalities Program.

van den Bogaart, M., Bruijn, S. M., van Dieën, J. H. and Meyns, P. (2020). The effect of anteroposterior perturbations on the control of the center of mass during treadmill walking. *Journal of Biomechanics* **103**, 109660.

van den Bogert, A. J., Geijtenbeek, T., Even-Zohar, O., Steenbrink, F. and Hardin, E. C. (2013). A real-time system for biomechanical analysis of human movement and muscle function. *Medical and Biological Engineering and Computing* **51**, 1069–1077.

van der Linden, M. H., Marigold, D. S., Gabreëls, F. J. M. and Duysens, J. (2007). Muscle reflexes and synergies triggered by an unexpected support surface height during walking. *Journal of Neurophysiology* **97**, 3639–3650.

van der Zee, T. J. and Kuo, A. D. (2020). Fully automated algorithm estimates muscle fascicle length from ultrasound image. *bioRxiv*.

van der Zee, T. J. and Kuo, A. D. (2022). TimTrack: A drift-free algorithm for estimating geometric muscle features from ultrasound images. *PLOS ONE* **17**, e0265752.

van Dijk, W. and van der Kooij, H. (2014). XPED2: A passive exoskeleton with artificial tendons. *IEEE Robotics and Automation Magazine* **21**, 56–61.

Vistamehr, A., Kautz, S. A., Bowden, M. G. and Neptune, R. R. (2016). Correlations between measures of dynamic balance in individuals with post-stroke hemiparesis. *Journal of Biomechanics* **49**, 396–400.

Vlutters, M., van Asseldonk, E. H. F. and van der Kooij, H. (2016). Center of mass velocity-based predictions in balance recovery following pelvis perturbations during human walking. *Journal of Experimental Biology* **219**, 1514–1523.

Vlutters, M., van Asseldonk, E. H. F. and van der Kooij, H. (2018). Foot placement modulation diminishes for perturbations near foot contact. *Frontiers in Bioengineering and Biotechnology* **6**, 1–14.

Voloshina, A. S., Kuo, A. D., Daley, M. A. and Ferris, D. P. (2013). Biomechanics and energetics of walking on uneven terrain. *Journal of Experimental Biology* **216**, 3963–3970.

Wakeling, J. M., Lee, S. S. M., Arnold, A. S., de Boef Miara, M. and Biewener, A. A. (2012). A muscle's force depends on the recruitment patterns of its fibers. *Ann Biomed Eng* **40**, 1708–20.

Wang, Y. and Srinivasan, M. (2014). Stepping in the direction of the fall: The next foot placement can be predicted from current upper body state in steady-state walking. *Biology Letters* **10**,.

Washabaugh, E. P., Kalyanaraman, T., Adamczyk, P. G., Claflin, E. S. and Krishnan, C. (2017). Validity and repeatability of inertial measurement units for measuring gait parameters. *Gait and Posture* **55**, 87–93.

Willems, P. A., Cavagna, G. A. and Heglund, N. C. (1995). External, internal and total work in human locomotion. *J Exp Biol* **198**, 379–93.

Willson, A. M., Anderson, A. J., Richburg, C. A., Muir, B. C., Czerniecki, J., Steele, K. M. and Aubin, P. M. (2022). Full body musculoskeletal model for simulations of gait in persons with transtibial amputation. *Computer Methods in Biomechanics and Biomedical Engineering* 1–12.

Witte, K. A., Fiers, P., Sheets-Singer, A. L. and Collins, S. H. (2020). *Improving the energy economy of human running with powered and unpowered ankle exoskeleton assistance*.

Wolff, J., Parker, C., Borisoff, J., Mortenson, W. ben and Mattie, J. (2014). A survey of stakeholder perspectives on exoskeleton technology. *Journal of NeuroEngineering and Rehabilitation* **11**, 1–10.

Yang, F., Bhatt, T. and Pai, Y. C. (2013). Generalization of treadmill-slip training to prevent a fall following a sudden (novel) slip in over-ground walking. *Journal of Biomechanics* **46**, 63–69.

Yeoh, H. T., Lockhart, T. E. and Wu, X. (2013). Non-fatal occupational falls on the same level. *Ergonomics* **56**, 153–165.

Yeow, C. H., Lee, P. V. S. and Goh, J. C. H. (2010). Sagittal knee joint kinematics and energetics in response to different landing heights and techniques. *Knee* **17**, 127–131.

Young, A. J., Foss, J., Gannon, H. and Ferris, D. P. (2017). Influence of power delivery timing on the energetics and biomechanics of humans wearing a hip exoskeleton. *Frontiers in Bioengineering and Biotechnology* **5**, 1–11.

Zajac, F. E. (1989). Muscle and tendon: properties, models, scaling, and application to biomechanics and motor control. *Crit Rev Biomed Eng* **17**, 359–411.

Zelik, K. E., Takahashi, K. Z. and Sawicki, G. S. (2015). Six degree-of-freedom analysis of hip, knee, ankle and foot provides updated understanding of biomechanical work during human walking. *Journal of Experimental Biology* **218**, 876–886.

Zeni, J. A. and Higginson, J. S. (2010). Gait parameters and stride-to-stride variability during familiarization to walking on a split-belt treadmill. *Clinical Biomechanics* **25**, 383–386.

Zeni, J. A., Richards, J. G. and Higginson, J. S. (2008). Two simple methods for determining gait events during treadmill and overground walking using kinematic data. *Gait and Posture* **27**, 710–714.

Zhang, J., Fiers, P., Witte, K. A., Jackson, R. W., Poggensee, K. L., Atkeson, C. G. and Collins, S. H. (2017). Human-in-the-loop optimization of exoskeleton assistance during walking. *Science (1979)* **356**, 1280–1284.

Zhang, T., Tran, M. and Huang, H. (2018). Design and experimental verification of hip exoskeleton with balance capacities for walking assistance. *IEEE/ASME Transactions on Mechatronics* **23**, 274–285.